Energy and volume flux into the deep ocean: examining diffuse hydrothermal systems

Matthew J. Pruis

A dissertation submitted in partial fulfillment of
the requirements for the degree of

Doctor of Philosophy

University of Washington

2004

Program Authorized to Offer Degree: School of Oceanography

University of Washington

Graduate School

This is to certify that I have examined this copy of a doctoral dissertation by

Matthew J. Pruis

and have found that it is complete and satisfactory in all respects,
and that any and all revisions required by the final
examining committee have been made.

Chair of Supervisory Committee:

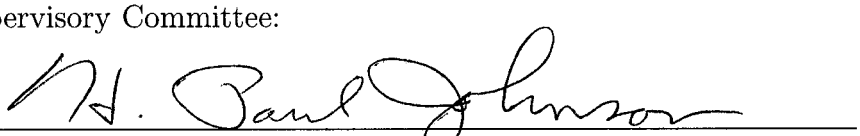

H. Paul Johnson

Reading Committee:

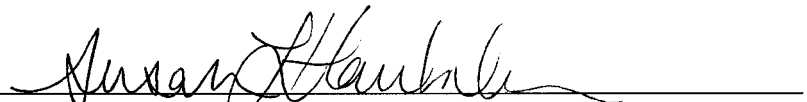

Susan L. Hautala

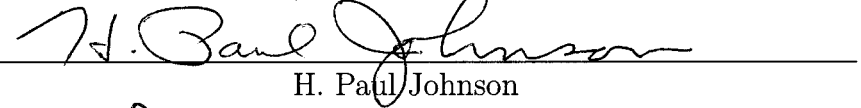

H. Paul Johnson

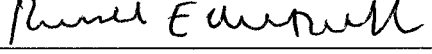

Russell E. McDuff

Date: 3/15/04

In presenting this dissertation in partial fulfillment of the requirements for the Doctoral degree at the University of Washington, I agree that the Library shall make its copies freely available for inspection. I further agree that extensive copying of this dissertation is allowable only for scholarly purposes, consistent with "fair use" as prescribed in the U.S. Copyright Law. Requests for copying or reproduction of this dissertation may be referred to Bell and Howell Information and Learning, 300 North Zeeb Road, Ann Arbor, MI 48106-1346, to whom the author has granted "the right to reproduce and sell (a) copies of the manuscript in microform and/or (b) printed copies of the manuscript made from microform."

Signature 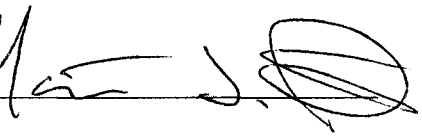

Date 15 March 04

University of Washington

Abstract

Energy and volume flux into the deep ocean: examining diffuse hydrothermal systems

by Matthew J. Pruis

Chair of Supervisory Committee:

Professor H. Paul Johnson
School of Oceanography

Hydrothermal circulation plays an important role in the chemistry of the world's oceans, the biology beneath and at the seafloor—as well as within the ocean itself—and also the geology of the uppermost igneous oceanic crust. Seawater slowly percolates through the crust, reacts with the basaltic rock, transports nutrients and heat, and eventually discharges back into the deep ocean—primarily at low-temperature vents and hydrothermal seeps. This dissertation is concerned with the flux of heat and fluid discharging from the seafloor and how field observations and numerical modeling can be utilized to describe the bulk hydrologic and mechanical properties of this fluid reservoir. Toward this end, heat and volume flux estimates were obtained using (1) a hydrologically sealed sampler which obtained direct measurement of fluid volume and heat flux from a diffuse hydrothermal vent on the seafloor, and (2) turbulence data collected above areas exhibiting low-temperature diffuse hydrothermal venting. Given that field observations near deep-sea hydrothermal vents are frequently modulated on tidal time-scales, a simple thermodynamic model is also proposed which can explain the modulation of temperature observed at some hydrothermal vents.

TABLE OF CONTENTS

List of Figures iii

List of Tables v

Chapter 1: Introduction 1

Chapter 2: Global scale heat and fluid flux 6

2.1 Temperature of rock / sediment interface 6

2.2 Global fluxes of fluid and heat 11

Chapter 3: Insights from direct measurement 14

3.1 Geologic setting 17

3.2 Instrumentation 18

3.3 Volume flux 21

3.4 Heat flux 23

3.5 Darcy flow approximation 25

3.6 Summary 28

Chapter 4: Boundary layer observations 30

4.1 Rock / water interface 34

4.2 Diffuse hydrothermal plumes 42

4.3 Instrumentation and data collection 45

4.4 Turbulent heat flux 49

4.5 Discussion 56

4.6 Summary 60

Chapter 5: Temporal Variability **62**

5.1 Model description 64

5.2 Effect of pressure perturbations on fluid temperature 75

5.3 Flow path model results 77

5.4 Model / data comparison 81

5.5 Conclusions 86

Chapter 6: Conclusions (and future work) **90**

6.1 Global-to-regional problems 90

6.2 Co-registered flow and temperature 91

6.3 Boundary layer mixing and flow 93

6.4 Temporal variability 94

6.5 Summary 94

Bibliography **96**

Appendix A: Where to find the files **116**

LIST OF FIGURES

1.1 Compilation plot of volumetric flow per unit area of seafloor 4

2.1 Ocean sediment thickness and heat flow 9
2.2 Temperature of crustal fluid reservoir 10
2.3 Volume flux of low temperature fluid versus crustal age 12

3.1 Axial Seamount location map 16
3.2 Image of diffuse flow sampler 19
3.3 Data plots from direct observation 20
3.4 Ten day record from Axial cement box 22
3.5 Power spectral plots from Axial cement box 24
3.6 Estimated permeability from Axial cement box 27

4.1 Location map of Endeavour Segment 35
4.2 Spider instrument 37
4.3 Volumetric flow vs fluid temperature 40
4.4 Near-bottom density profile 44
4.5 Turbulence instruments 46
4.6 Normalized power spectra of typical turbulence sensor 49
4.7 Example 17-min data records from turbulence instruments 50
4.8 Dissipation and λ_{peak} estimates 53
4.9 Shear production vs buoyancy conversion 55
4.10 Heat flux to rock / water interface temperature 57

4.11 Probability distribution of turbulent heat flux 59

5.1 Two phase curve and reaction zone temperatures 69
5.2 Plot of $\log_{10}(\Gamma(k/\phi))$ 73
5.3 Variation in temperature and enthalpy for an incompressible fluid . . 76
5.4 Change in enthalpy of the fluid leaving the reaction zone 77
5.5 Hydrothermal fluid ascent paths 78
5.6 Temperature effect due to different enthalpy variations 80
5.7 High-temperature data records 83
5.8 Modeled and observed effluent temperatures 87

LIST OF TABLES

2.1 Hydrothermal volume flux from crustal reservoir 8

4.1 Rock / water interface temperature 38
4.2 Turbulent heat flux results 47

5.1 Upflow times for high-temperature hydrothermal fluid 85

ACKNOWLEDGMENTS

I have frequently needed to call on many colleagues and friends to understand and put these results into context. It is appropriate that I mention a few specifically however. I would like to particularly thank my graduate advisor, H. Paul Johnson, who has not only advised, mentored and directed my sometimes mis-guided research goals—he has shown me the joy and fun of accomplishing basic science research. I believe I am hooked for life. I would also like to thank Tor Bjorklund, Jim Cowen, the Atlantis crew and the entire Alvin group for somehow managing the installation of our monitoring instrument package on the Axial Seamount. Donald Janssen provided access to both his expertise and also his laboratory for testing the cement mixtures, which proved critical to obtaining a good hydrologic-seal with the seafloor. Michael Hutnak performed all the calibration, testing and instrument preparation for the Axial Seamount monitoring instrument. Bill Fredericks designed the turbulence instrument deployment housings. A. J. Williams III, A. T. Morrison and D. Schaaf of Nobska provided substantial assistance in overcoming several last-minute engineering challenges involving the MAVS current meters. Irene García Berdeal, Susan Hautala, and Tor Bjorklund accomplished much of the turbulence instrument calibration, preparation and design. W. Wilcock and H. Mojfeld provided insightful comments and early discussions that helped formulate the thermodynamic model proposed. R. McDuff provided the impetus to pursue this portion of the dissertation research. Data for the observations / model comparison was provided by R. Embley and C. Fox. These data sets were collected as part of the NOAA NeMO program. Research was supported by NSF grants OCE9911523 and OCE0085615 and an Egtvedt scholarship.

DEDICATION

For my wife, Elaine. You did all the hard work. Thank you for your encouragement. Thank you for your determination. Thank you for filling my life with joy. I love you.

Chapter 1

INTRODUCTION

Hydrothermal circulation plays an important role in the chemistry of the world's oceans, the biology within the basaltic crust—as well as within the ocean itself—and also the geology of the uppermost igneous oceanic crust. It is estimated that a volume of sea water equivalent to that contained within the entire global ocean is circulated through the upper oceanic crust on a timescale of $\sim 10^5$ years [1]. This seawater slowly percolates through the crust (average residence time is 2700 years), reacts with the basaltic rock, transports nutrients and heat, and eventually discharges back into the deep ocean—primarily at low-temperature (<20 °C) vents and hydrothermal seeps [1]. This dissertation is primarily concerned with the flux of heat and fluid discharging from the seafloor, and how field observations and numerical modeling can be utilized to describe the bulk hydrologic and mechanical properties of this fluid reservoir. Most of the work described in this dissertation is contained in four research papers [1, 2, 3, 4]. Please see Appendix A for information on obtaining copies of the papers.

The global scale upper oceanic reservoir and the importance of low-temperature hydrothermal venting—with respect to the volume and energy fluxes—is described in chapter 2. Global databases of heat flow [5], sediment thickness [6] and crustal age [7] allow for calculation of reservoir temperatures, predicting temperatures between 10 and 20 °C at the sediment / rock interface in crust younger than 70 My. Utilizing these temperature estimates, heat flow measurements [5] and a model for the thermal

structure and evolution of the oceanic lithosphere [9], mean hydrothermal fluxes into the deep ocean were calculated as a function of plate age.

While analysis of these global data sets suggests that the impact of off-axis fluxes of heat and volume are significant, much can also be learned from the detailed analysis of single sites and locations. In chapter 3, the results obtained from sampling one square meter of diffusely venting seafloor over the course of 206 days are examined. A unique sampling strategy, which involved the cementing of a permanent fluid sampler directly to the seafloor on Axial Seamount, Juan de Fuca Ridge, allowed the first long-term direct coupling to a low-temperature hydrothermal vent on a mid-ocean ridge. Using the hydrologically sealed sampler, direct measurement of fluid volume and heat flux from a diffuse hydrothermal vent on the seafloor was obtained over an extended period of time. Enhanced variance at both tidal and lower frequencies was recorded with a high coherence between the temperature and flow data. Mean volume and heat flux for the square meter of seafloor sampled by the instrument are estimated at 48 m^3/yr and 260 W/m^2, respectively. Inferred Darcy velocities of the fluid within the crust beneath the sampled region are approximately 1.5×10^{-6} m/s and indicate fluid velocities within cracks in the substrate of 1–4 m/day, with an effective upper crustal permeability of 10^{-11} to 10^{-12} m^2. While the measured variability in fluid flow is driven primarily by changes in the thermal buoyancy of upwelling fluid, there is also a significant (above hydrostatic) pressure gradient contribution to the measured flux. This overpressure produces roughly four times the driving force compared to that attributed to thermal buoyancy alone. Small variations in the volume flux and the effluent fluid temperature ($\sim 1.5 \times 10^{-8}$ m/s and ~ 0.5 °C, respectively) also occurred on approximately tidal time scales and appear to be related to poroelastic control of the velocity of hydrothermal fluid through the seafloor boundary (i.e. tidal pumping).

Expanding on the results obtained from a single point location, estimates of turbulent heat flux at 25 different locations (36150 individual estimates) near diffuse hydrothermal vents on the Endeavour Segment of the Juan de Fuca Ridge are ex-

amined in chapter 4. This turbulence data reveals several processes important in turbulent heat transfer in this unusual oceanic environment. Temperature measurements obtained at the rock / water interface demonstrate that low-temperature diffuse effluent leaving the oceanic crust is highly variable. Our calculations show that this variability at the interface is quickly mixed in the near-bottom boundary layer. Velocity and temperature time series, at a measurement height of roughly 0.5 meters above the seafloor, indicate that heat and momentum flux occur at nearly the same scale. Typical turbulent eddies are 0.10 to 0.25 m in dimension, with the largest (energy containing) turbulent eddies occurring at scales of approximately 0.45 m. The turbulent eddies that are responsible for heat transfer depend mainly on the shear forcing, not thermal buoyancy. Probability distribution functions confirm that most of the heat flux occurs in intermittent events, and yield a mean heat flux value of order 4 kW/m^2.

Substantial variability in the observed heat fluxes and temperatures of the effluent fluid in these different studies imply large variability in the transport properties of crust through which the hydrothermal fluid is flowing. In Figure 1.1 is plotted the specific discharge of fluid through the seafloor, for different heat fluxes or crustal permeabilities, as a function of hydrothermal fluid temperature. In order to obtain heat fluxes from low temperature fluid advecting through the seafloor on the order of hundreds to tens of thousands of W/m^2, either permeabilities greater than 10^{-12} m^2 are required or the pore fluid must be overpressured with respect to the hydrostatic gradient. Figure 1.1 shows that if the off-axis sediments had average permeabilities in the range of 10^{-13} to 10^{-15} most of the off-axis advective flux of fluid from the crustal reservoir could be occurring through the sediments. However, the partitioning between the volume and heat fluxes of hydrothermal fluid through small areas of exposed basalt outcrops (with substantially higher permeabilities) and fluid which flows up through a substantial thickness of sediment is still unclear.

Many field observations near deep-sea hydrothermal vents are modulated on tidal

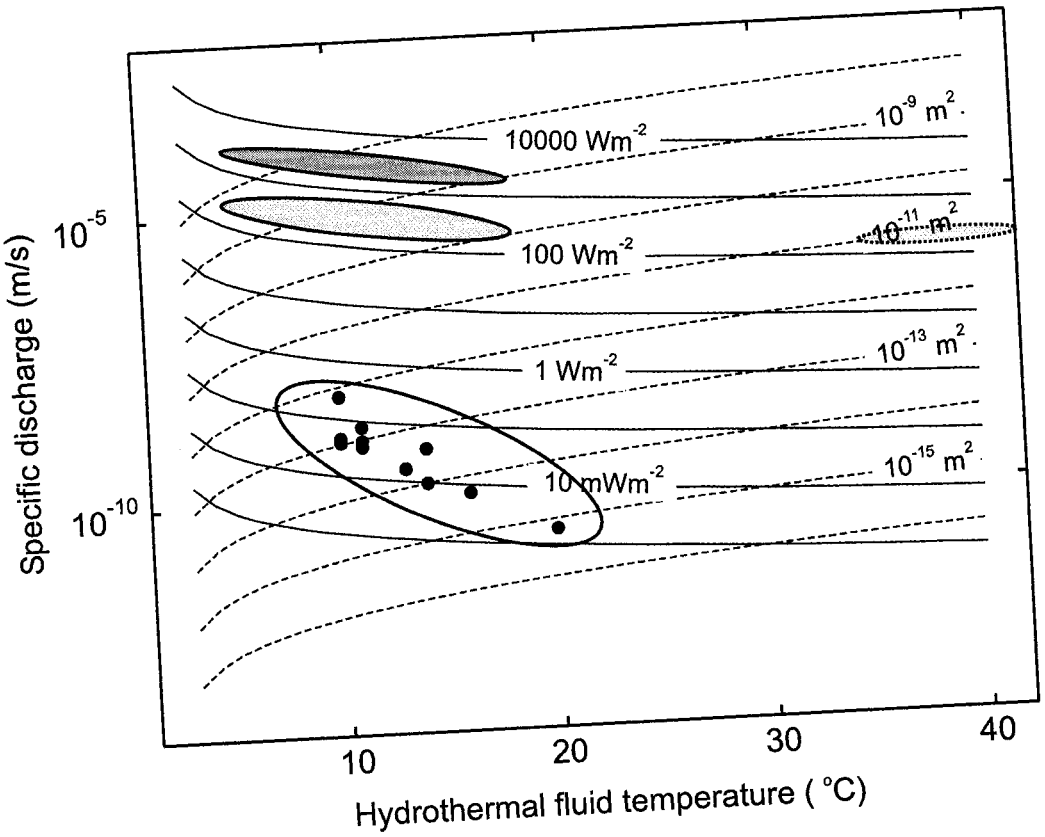

Figure 1.1: Volumetric flow per unit area of seafloor for different hydrothermal fluid temperatures. Calculation of the permeability and specific discharge in this figure assumes the pressure gradient within the crust is hydrostatic and all the buoyancy is thermally-derived. Filled circles are the hydrothermal volume flux computed in Chapter 2 divided by the area of seafloor in each crustal age bin. Lightly shaded region schematically shows the approximate range in median turbulent heat flux estimates, 50–730 W/m^2, obtained along the Endeavour segment of the Juan de Fuca Ridge. The slighter darker shaded region above it schematically shows the approximate range in mean turbulent heat flux estimates, 1800–5500 W/m^2 in the same area (see Chapter 4). The mean rock /water interface temperature observed at the base of the turbulence instruments was approximately 9 °C. Measurements at individual sites have heat fluxes as high as 150 kW/m^2. The dashed shaded region at higher temperatures shows the results obtained for the hydrologically sealed sampling box discussed in Chapter 3 before correcting for the observed overpressure.

time-scales, the observations discussed in this dissertation notwithstanding. These measurements range from physical quantities such as pressure, temperature, effluent fluid velocity and vent fluid composition, to observations of micro-seismic activity and the biological response of vent animals. Therefore in chapter 5, a simple thermodynamic model that can explain the modulation of effluent fluid temperature measured at some hydrothermal vents is examined. The model solves the governing equations for a compressible two-phase flow in one dimension, utilizing the equation of state for pure water and Darcy's law for fluid flow in porous media. In order to generate effluent fluid temperatures that are lower than the boiling point at the rock/water interface (such as those typically observed), two simple model cases are examined: (1) conductive heat loss to the host rock and (2) mixing of the upwelling hydrothermal fluid with cooler background water. If the heat loss required for fluid to depart from the boiling curve occurs near the seafloor interface, our model shows that it is plausible for a tidally-modulated thermal signal to propagate from a deep source area. However, if significant cooling occurs at depth, dissipative loss of a tidally-induced signal may be substantial. While this model simplifies the physical processes present in deep-sea hydrothermal systems, simulation results compare well with field data collected from high-temperature vents on Axial Seamount in the Northeast Pacific.

In this dissertation, many aspects of the volume and energy flux of diffuse hydrothermal fluids will be examined; from the global magnitude of low-temperature venting all the way down to observations obtained from just a single square meter of seafloor. Both temporal and spatial variability are discussed, as are the mixing processes and the hydrogeology and thermodynamics necessary to describe the interactions and interplay between point observations and integrative measurements. The observations and modeling discussed will hopefully contribute to the growing interdisciplinary foundations which are attempting to create a more complete bio-geo-chemical description of low-temperature venting of hydrothermal fluid into the deep ocean.

Chapter 2

GLOBAL SCALE HEAT AND FLUID FLUX

There is a global scale fluid reservoir residing within the uppermost igneous oceanic crust. This hydrothermal fluid reservoir forms initially within volcanic rocks newly erupted at mid-ocean ridges, but extends to the vastly larger and older ridge flanks. The upper oceanic crust is porous and permeable due to the presence of lava drain-backs, fissuring, and inter-unit voids [8], and this porosity and permeability allows active fluid circulation to advect measurable quantities of lithospheric heat from the crust to an average age of 65 My [1]. Heat flow and sediment thickness data allow calculation of reservoir temperatures. Utilizing these temperature estimates, heat flow measurements, and models for the thermal structure and evolution of the oceanic lithosphere; mean hydrothermal fluxes into the deep ocean as a function of plate age have been computed [1]. The total hydrothermal volume flux into the oceans approaches 20% of the total riverine input, and may contribute to the global seawater mass balance.

2.1 Temperature of rock / sediment interface

The average thermal characteristics of the global crustal reservoir can be estimated by merging (using crustal age as the common index) heat flow and sediment thickness data determined over wide geographical areas into a box model of the seafloor (Table 2.1). While this type of model is useful for estimating global properties when data are sparse [9, 10], it is unlikely to successfully predict crustal properties at any given geographical location. For example, it has been well documented that the uppermost

igneous crust on the Juan de Fuca Plate is anomalously warm, probably exceeding 100 °C in some locations even though the crust is younger than 10 Ma [11, 12]. Uncertainties for all crustal properties in Table 2.1 were estimated by iteratively removing samples greater than 5 standard deviations from the mean, and then computing the remaining average deviation. Twenty equal area age bins, each 5% of the total range, were chosen for all distributions other than porosity. An additional age bin of 0–1 Ma crust allowed identification of young on-axis hydrothermal flux. Each subsequent bin contains an area of 1.34×10^7 km^2. Global sediment thickness for the ocean basins has been determined geographically [6] and then merged with a separate crustal age distribution [7]. These data do not include Atlantic data north of 50° N nor the region near the Sea of Okhotsk, as this data is not currently processed (D. Divens, pers. comm., 2003). Sediment thickness for time intervals of equal area are plotted as a function of age in Figure 2.1, showing the expected systematic increase in sediment cover with increasing crustal age. Heat flow data were also compiled geographically [5], marginal basins were excluded, and then merged with crustal age over the same intervals. Although Figure 2.1 represents more heat flow data than that used by the most recent previous compilation [9, 10], the results are not dramatically different. The age of 70 My where heat flow data and the conductive flux model merge, and where the crustal reservoir can be considered convectively disconnected from the overlying ocean by thick impermeable sediments, is approximately the same as that determined by previous analyses [9]. This interpretation yields a globally-averaged crustal age—yet both venting and re-charge of fluid can occur locally in much older crust [13].

Biological and chemical processes within the oceanic crustal reservoir depend strongly on temperature. To estimate the temperature of the sediment / basement interface with crustal age, a method previously applied to heat flow data on the eastern flank of the Juan de Fuca Ridge, which was verified by the logging of several Ocean Drilling Program holes [12], was utilized. In this technique, temperature gra-

Table 2.1: Physical properties of the crustal reservoir binned into regions of equal area, each 5% of the total area of seafloor excluding margins. Uncertainties for all crustal properties were estimated by iteratively removing samples greater than 5 standard deviations from the mean, and then computing the remaining average deviation.

Age mean (Ma)	Sediment thickness [6] (m)	Heat flow measured [5] (mW/m^2)	Heat flow model [9] (mW/m^2)	Rock/sediment temperature (°C)	Hydrothermal volume flux (km^3/yr)
2.4	47 ± 32	202 ± 13	464	10 ± 7	3037 ± 2307
7.3	95 ± 55	110 ± 11	192	11 ± 6	879 ± 602
11.9	124 ± 74	109 ± 11	149	14 ± 8	337 ± 248
16.5	127 ± 75	77 ± 9	126	10 ± 6	579 ± 405
21.2	150 ± 78	67 ± 7	111	11 ± 6	505 ± 323
25.7	167 ± 86	59 ± 9	101	10 ± 5	492 ± 325
30.3	186 ± 96	55 ± 8	93	11 ± 6	430 ± 281
35.6	205 ± 109	50 ± 9	86	11 ± 6	403 ± 275
41.9	208 ± 109	62 ± 8	79	13 ± 7	155 ± 123
48.6	228 ± 128	63 ± 7	73	14 ± 8	87 ± 83
55.2	259 ± 158	58 ± 6	69	14 ± 9	85 ± 76
62.5	307 ± 203	57 ± 7	65	16 ± 11	54 ± 63
70.3	364 ± 255	60 ± 5	62	20 ± 14	11 ± 29
78.3	435 ± 307	61 ± 7	59	23 ± 17	-9 ± 37
87.0	564 ± 366	52 ± 4	57	24 ± 16	20 ± 24
97.6	673 ± 477	52 ± 5	54	28 ± 20	10 ± 21
108.7	633 ± 501	54 ± 3	53	27 ± 22	-5 ± 14
122.0	783 ± 591	51 ± 2	51	31 ± 24	0 ± 6
139.1	614 ± 394	47 ± 3	50	24 ± 16	13 ± 18
164.1	1013 ± 882	43 ± 4	49	31 ± 27	23 ± 25

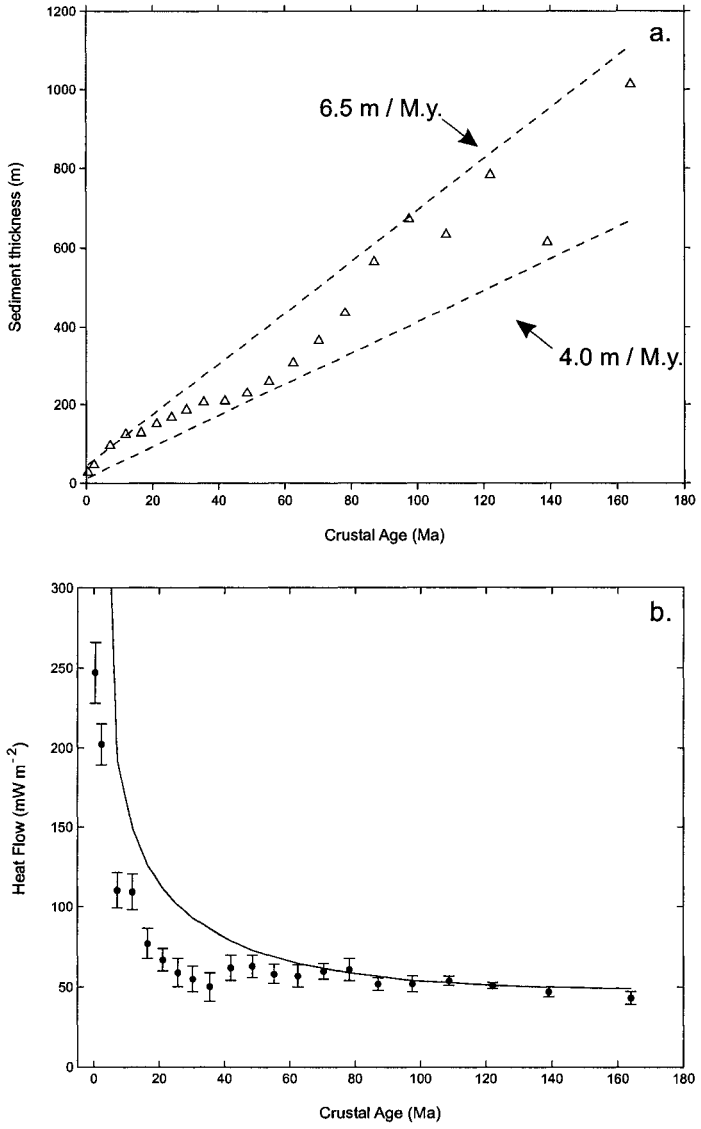

Figure 2.1: (a) Global sediment thickness as a function of crustal age. The geographically distributed data [6] are merged with crustal age [7] and then compiled in 20 equal area bins. Dashed bounding lines represent global rate of sediment accumulation including the effect of compaction. (b) Compiled global heat flow data [5] compared to flux from the purely conductive GDH-1 models [9, 10]. The difference between measured heat flow and the conductive model represents the advection of heat and fluid between the crustal reservoir and the overlying seawater.

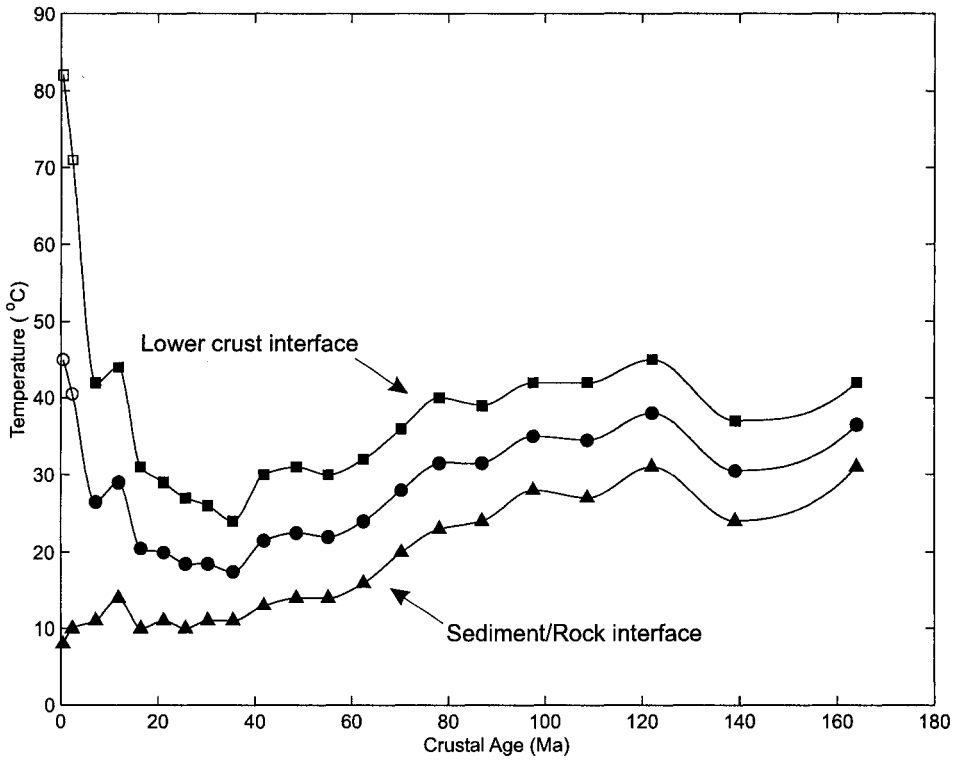

Figure 2.2: Estimated temperatures for the crustal reservoir as a function of age. Triangles are temperatures for the sediment / rock interface, squares are values for the bottom of the 600 m thick high porosity zone, and circles are the mean for the entire upper crustal reservoir. Open symbols have higher uncertainty (>20%) due to the assumption of no fluid convection within the crustal section. Temperatures represented as filled symbols should be independent of this assumption.

dients determined from surficial heat flow measurements are projected downward to the sediment / basement interface, using estimates of sediment thickness and thermal conductivity, and adjusted for a bottom water temperature of 1.5 $\pm$ 0.5 °C [17]. Sediment thermal conductivities can vary both geographically and as a function of depth, thus in this analysis a global compilation derived from the extensive Ocean Drilling Program data set was used [14]. Results from the calculation of sediment / basement interface temperatures are shown in Figure 2.2, with the youngest (sediment-covered) basement temperatures near 10 °C, rising near 30 °C for 120 My old crust.

Estimated mean basement temperatures using this simple non-convecting model are substantially elevated above bottom water temperatures, increasing to near 40 °C in crust of mid-Cretaceous age (Figure 2.2). This increase of crustal temperature with increasing age older than 20 My is a consequence of a relatively uniform heat flow for older crust that is accompanied by an increase in Cretaceous sediment thickness (Figure 2.1). Although the mid- and lower-reservoir temperatures can be over-estimated by this method by as much as 20% in young crust where convection is present [15, 16], the temperatures at the sediment/rock interface, and the associated fluxes of heat and fluid into the deep ocean, are not affected by the model assumptions.

2.2 Global fluxes of fluid and heat

For a given age interval, the difference between measured heat flow and the thermal flux expected for a conductive-only plate model provides an estimate of the missing heat flux due to the advection of fluid from basement to overlying seawater [9, 10]. These differences between measurement and model, along with sediment / basement temperatures (Figure 2.2) and a global bottom water temperature, were converted into estimates of fluid flux in to/out of the basement reservoir as a function of crustal age (Figure 2.3). Volume fluxes were determined using

$$Q_h = \rho c_p q (T - T_0)/A, \tag{2.1}$$

where Q_h is the heat flux, ρ is the water density, c_p is the specific heat of water, q is the volume flux, T is temperature at the rock / sediment interface, T_0 is the bottom water temperature and A is the area of the seafloor in the bin. Other parameter uncertainties were propagated to obtain the uncertainty in volume flux. As measured heat flow data approaches purely conductive values (Figure 2.1b), average fluid flux approaches zero for crust 70 My and older. Figure 2.3 shows that at least 50% of the total global hydrothermal fluid flux is from ridge flank crust with ages between 5 My and 70 My. This analysis does not include the small component of high temperature

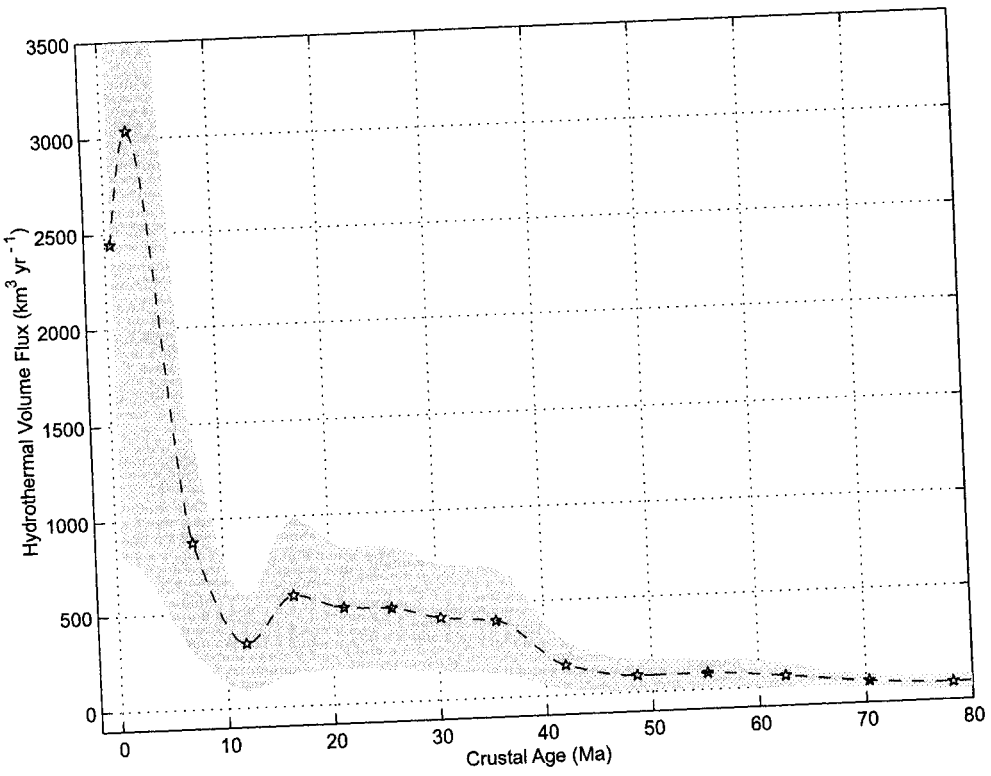

Figure 2.3: Flux of hydrothermal fluid to / from the crustal reservoir as a function of age. Shaded area shows the range of propagated uncertainties (see Table 2.1). Estimates of flux are high for young crust and approach zero at 70 Ma.

venting from the axial zone where fluid temperatures can exceed 350 °C [21], which would require the percentage of the off-axis fluid flux to be slightly larger.

Calculations based on these parameters give a total age-integrated flux of 7.1 × 10^{12} m^3/yr of low-temperature hydrothermal fluid into the deep waters of the global ocean, with 3.0 × 10^{12} m^3/yr in crust <5 My and 4.1 × 10^{12} m^3/yr occurring in older crust. These compare to previous estimates of 4.2 × 10^{12} m^3/yr (axial flux), 7.3 × 10^{12} m^3/yr (flank flux) and 11.5 × 10^{12} m^3/yr (total flux) [21] and 2.5 × 10^{12} m^3/yr (flank flux only) [18] that were based on earlier data compilations.

While this amounts to 18% of that due to riverine flow into the oceans, which is estimated to be 4 × 10^{13} m^3/yr [19], the impact of this flux on the seawater

chemical inventory is uncertain. The composition of hydrothermal fluid from varying reservoir source temperatures is substantially different than river water, and crustal fluid is injected near the seafloor while river input is added at or near the surface. There is a continuing ambiguity in the chemical composition of the low-temperature diffuse fluids in general [20], and ridge-flank hydrothermal fluid in particular—which is strongly dependent on temperature, age, rock alteration and circulation history, and only limited fluid chemical analyses are available from anomalous sites unlikely to represent global averages [18, 21, 22]. Nonetheless, the flux of mass and energy introduced into the deep ocean via low-temperature off-axis venting of fluid through the seafloor is substantial.

Chapter 3

INSIGHTS FROM DIRECT MEASUREMENT

Direct measurement of flow from diffuse hydrothermal systems has proven difficult because, unlike the visually impressive high temperature edifices, diffuse flow is spread over a large spatial area and both the temperatures and the velocities of the fluid are small. The majority of previous studies have therefore focused on the measurement of diffuse fluxes utilizing integrative water-column measurements [23, 24, 25, 26]. These measurements allow efficient integration of the highly variable low-temperature fluxes over relatively large (vent-field scale) geographic areas, but are also complicated by the decoupled nature of the measurement and the source. Thus measurements of hydrothermal fluxes constrained to either the near-bottom boundary layer, or the neutrally buoyant plume, require careful analysis to separate effects from bottom currents, tidal flow and the natural spatial and temporal variability of diffuse plumes and their sources [27, 28, 29, 30]. Even with these difficulties, these data have proven valuable in determining the partitioning between diffuse and high temperature fluxes in mass, heat and chemical constituents. Within the axial zone, the heat flux from diffuse sources has been estimated to be as much as 1 to 10 times that from focused high temperature venting [23, 24, 31]. Simple scaling of this heat flux to a mass flux, assuming a 10 °C diffuse fluid temperature and a 300 °C high temperature end-member, implies that over 95% of the volume flux is from low temperature sources within active vent fields.

Previous direct measurements of co-registered volume and heat flux at low temperature venting sites studied areas near high temperature sulfide-vent structures [31, 32] or similar locales where diffuse flow was visibly concentrated [33, 34]. The

measured effluent velocities in these experiments ranged from 0.5 to 140 mm/sec [31, 35]. These diffusely venting systems are typically believed to be composed of a mixture of high temperature fluids and seawater that is entrained directly into the venting structure, and may be hydrologically distinct from the basaltic-hosted diffuse venting sampled in this study. A recent geochemical study of directly-sampled diffuse vent fluid from the Lucky Strike hydrothermal vent field on the Mid-Atlantic Ridge showed that low-temperature venting may become hydrologically disconnected from the source high-temperature fluid [34]. In such cases the fluid may undergo a heating and cooling history that is not consistent with simple mixing of a high-temperature endmember fluid with seawater.

Co-registered measurements of effluent fluid flow and temperature have also demonstrated a strong positive correlation between the volume flux and effluent temperature at tidal or lower frequencies, with generally poor correlations at higher frequencies [31, 32]. Occasional periodic flow reversals (i.e. cold seawater flowing into the crust) were also documented, and are qualitatively similar to measurements of flow reversals that have been seen in the underpressured ODP and DSDP drill holes (i.e. 1024C, 1027C and 395A) [31, 36]. Tidal pumping of the seafloor is a known consequence of the dynamic water tide; but without a good estimate of permeability of the exposed crust on the seafloor, the magnitude of this periodic flushing of the upper crust has remained uncertain (see [36] for more discussion). For the pressure effect of the water tide to yield substantial periodic seawater flow into unsedimented oceanic crust (with seawater penetration of order 0.5 m), the permeability must be sufficiently high, of order 10^{-10} m^{-2}, a value well within the range estimated for young oceanic crust [36, 37, 38]. If the occurrence of flow reversals into the exposed young ocean crust could be generalized over large areas, it would imply a zone of intense mixing within the upper 0.5 meter of unsedimented oceanic crust, with major implications to geologic, hydrologic and biologic processes in the uppermost crust.

In this chapter, co-registered fluid flow and temperature data collected from a

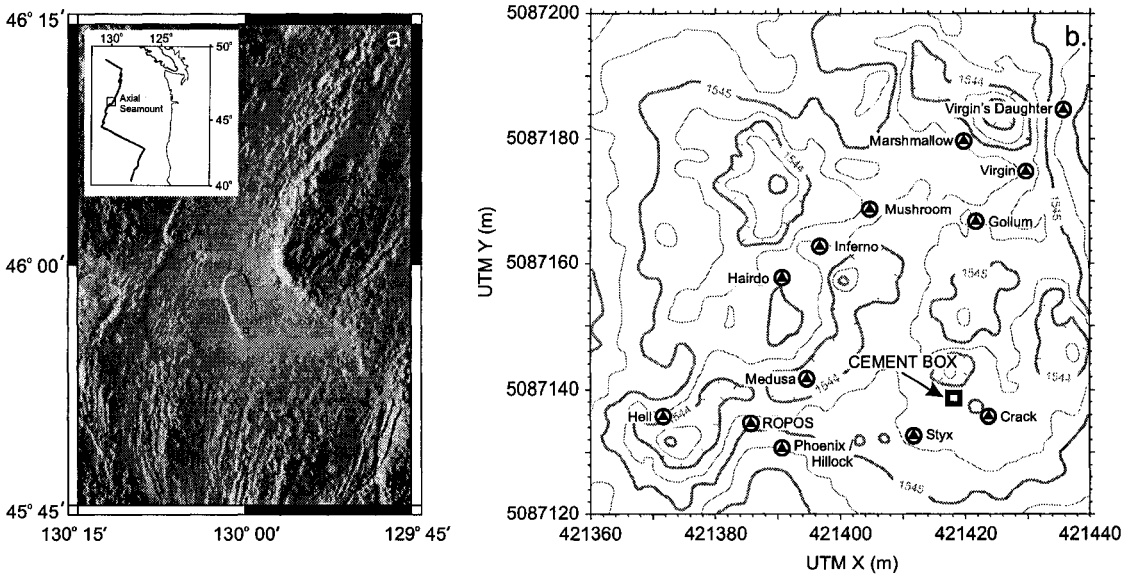

Figure 3.1: Axial Seamount. (a) The instrument package was deployed in the ASHES vent field in the southwestern caldera. Lighting in the image is from the east and the depth in the image range from 1411 to 2863 meters. The SeaBeam bathymetric data used in this figure was obtained from the Ridge Multibeam Synthesis Project [http://ocean-ridge.ldeo.edu]. (b) ASHES vent field is characterized by pervasive low-temperature venting encompasses an area of roughly 200 m $\times$ 1200 m. The most intense hydrothermal venting is however constrained to a 180 m $\times$ 180 m region covered by smooth sheet and lobate flows. Known high temperature vents are labeled (locations provided by R. Embley, pers. comm.). There is little bathymetric relief ($<$ 4 m) over this entire region of intense venting [39].

low-temperature diffuse vent on Axial Seamount on the Juan de Fuca Ridge in the Northeast Pacific is examined. After describing the geologic context and background of related studies done in this area in Section 3.1, the instrument package and sampling system is described in Section 3.2. In Sections 3.3 and 3.4, the volume and thermal fluxes through the sampling device is shown and some detail on their variations over the deployment interval is given. Simple modeling used in Section 3.5 shows that the measured diffusely venting flow through the seafloor interface in this location is overpressured with respect to what would be expected for thermal buoyancy-driven flow alone.

3.1 Geologic setting

Axial Seamount, the youngest member of the Cobb-Eickelberg seamount chain, is a well-studied ridge axis volcano on the central Juan de Fuca Ridge, and represents a good natural laboratory for a hydrologic study of hydrothermal systems. The caldera floor (approximately 8 km $\times$ 4 km) is the locus of substantial hydrothermal venting, with several widely-distributed vent fields found around the caldera rim [40]. Our monitoring package was deployed in the ASHES vent field; which is composed of approximately a dozen high temperature (>200 °C) vents and includes a large area of diffuse venting spread over approximately 0.24 km^2 (see Figure 3.1). The site is appropriate for a long-term monitoring of fluid and temperature fluxes since the surrounding area has been well mapped and there is a long history of related fluid chemistry and geophysical measurements [40, 41]. Ocean bottom gravity studies have shown that the seamount is has an absolute porosity of approximately 38% for the upper volcanic crust, while magnetic studies indicate that the seamount has either a highly altered or a very warm (>100 °C) central core [43, 44]. Recent seismic tomographic mapping has confirmed the presence of a zone of partial melt approximately 1–2.5 km beneath the surface of the caldera [45].

Interestingly, prior to 1998, the area surrounding the seamount was the most tectonically active region in the NE Pacific detectable utilizing the US Navy's SOSUS arrays. A volcanic eruption in January, 1998, on the southeastern caldera wall has however dramatically altered the tectonic regime, with a general paucity of earthquakes in this region following the eruption, including the Cleft segment to the south and the Co-Axial segment to the north [46]. The measurement interval for our vent monitor began in late 1998, approximately one year after the nearby eruption. The low level of local tectonic activity may have allowed the detection of a far field response to the June 8th, 1999, earthquake on the Endeavour segment, approximately 220 km to the north [47]. This earthquake, which may have been part of a larger

aseimic spreading event, had significant impact on diffuse venting at the nearby Endeavour vent fields and was recorded at several drillholes on the ridge flank as well as the sedimented Middle Valley ridge-axis drillhole [48, 49].

Our sampling instrument was placed in the Crack Vents region in the southwest corner of the ASHES vent field. The area is dominated by fractured ropy sheet flows. Many of the fractures (generally < 5 cm in width) in this region are marked by bordering accumulations of anhydrite and have exit fluid temperatures in excess of 200 °C, although there are no large anhydrite mounds or spires in this area [39]. Effluent fluid chemistries are similar to the high-temperature phase-separated (gas-enriched, low-chlorinity) fluids exiting at the anhydrite-dominated Virgin Mound vent located 40 meters to the north [41]. Generally, brine phase fluids are discharging from the high-temperature sulfide chimneys active in western part of the ASHES vent field near the caldera wall; while vapor phase components appear to be venting as diffuse flow from the seafloor surrounding these chimneys and in anhydrite chimneys to the east. It has been proposed that the observed pattern of spatial segregation of fluid phases is due to the relative permeability variability of two-phase flow within a substrate; with brine phase fluids confined to large flow conduits by a surrounding relative permeability barrier, and vapor phase fluids flowing diffusely through the surrounding host rock [42].

3.2 Instrumentation

The seafloor boundary represents a complex and difficult site for sampling fluids, where pillow flows and fissured basalt make it difficult to obtain a reliable hydrologic seal with the seafloor. Our instrument package was designed to overcome this difficulty in order to obtain un-contaminated diffuse hydrothermal fluid samples as evidence for a microbial biosphere living within the oceanic crust [50]. Our sampling design consists of a rectangular 1 m $\times$ 1 m Teflon-lined polyethylene base surrounded by a

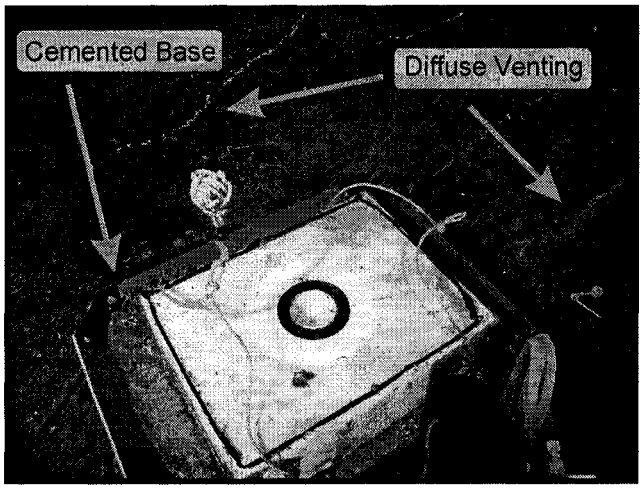

Figure 3.2: The deployment is in an area of an extensive sheet flow that is fractured by a series of N-NE trending fissures (1–3 cm in width). White staining present on some fractures are bordering accumulations of anhydrite. The instrument package was installed into the circular sampling port seen on the upper surface of the cemented base. This high-resolution digital photograph was taken by R. Embley with ROPOS during a cruise in 2002 funded by the NOAA Vents Program. Camera development was by the Canadian Scientific Support Facility and Deep Sea Power and Light.

flared-out cofferdam (Figure 3.2). The cofferdam was grouted with a concrete mixture that hydrologically sealed the box to seafloor [51]. A one-meter tall instrumented column was mounted on the top of the permanently-deployed base consisting of the datalogger, internal and external thermistors, a filter pack designed to collect dissolved and particulate organic carbon, and the flow sensor. The upwelling fluid was focused from the one square meter of seafloor sampled by the box, through the Teflon-lined base and into a 1.27 cm diameter sampling tube where the fluid volume flux was measured. The pressure drop due to focusing the flow through the small pipe diameter is less than 1% the vertical buoyancy of the fluid. The flowmeter was a Kobold Instruments magnetic paddle wheel flow sensor (DPL-1120) modified to perform at full-ocean depths. Temperatures were recorded both at the input of the instrument port and also externally to the sampling package. All sensors initially sampled every

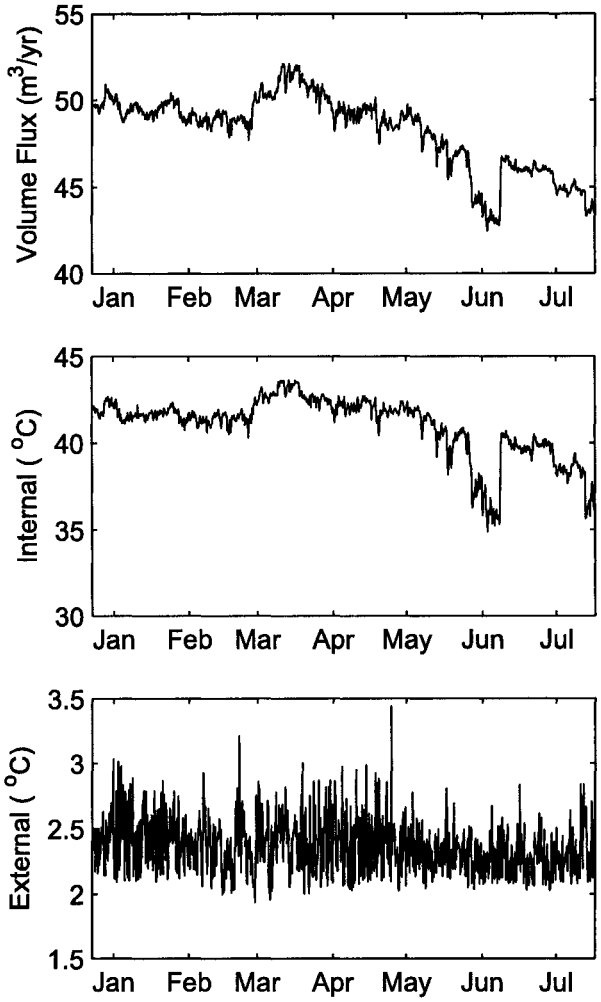

Figure 3.3: Data plots showing the (a) volume flux, (b) temperature of the effluent fluid, and (c) the temperature of the bottom water near the cement box recorded on an externally mounted thermistor. Note the rapid response that occurs within 8 hours of the June 8th earthquake which occurred approximately 220 km to the north, and the possible precursor decrease in fluid flow that occurs approximately two weeks preceding the earthquake [47, 49].

20.5 minutes during the first 21 days of the record, at which point the sample rate was subsequently slowed to one sample every four hours for the remainder of the record.

3.3 Volume flux

Given that the instrument base is in contact with an area much larger than the crack widths (1-3 cm) in the area covered by the instrument base, measurements of volumetric flux through the seafloor interface (see Figure 3.3) and the conservation of mass equation can be used directly, (i.e. $A_1 v_1 = A_2 v_2$), to calculate the Darcy velocity of the upwelling fluid within the subsurface. The specific discharge is simply the measured fluid flux rate divided by the area of the seafloor sampled,

$$\overline{u} = \frac{q}{A}. \tag{3.1}$$

The velocities measured in the instrument sampling pipe, with a diameter 1.27 cm, ranged from 1.0–1.3 cm/s, inferring a specific discharge of $1.3 - 1.6 \times 10^{-6}$ m/s during the experiment interval. The total fluid flux through the one square meter of seafloor sampled is 48 m^3/yr. Utilizing an idealized geometrical model for the porosity structure of oceanic crust in which circular tubes form a regular cubical matrix throughout an otherwise impermeable rock matrix,

$$\overline{u} = \frac{\phi u_c}{3}, \tag{3.2}$$

the vertical velocity of the fluid within volcanic rock matrix, u_c, can be estimated if the porosity, ϕ, is known [36, 52, 53]. Assuming that the effective porosity (available for fluid flow) ranges somewhere between 10% and the bulk porosity estimate of 38% obtained from seafloor gravity studies [43] and that the horizontal (non-vertical) flow within the substrate is negligible, equation (3.2) gives vertical velocities for the fluid within cracks in the substrate which are between 8 to 30 times the specific discharge.

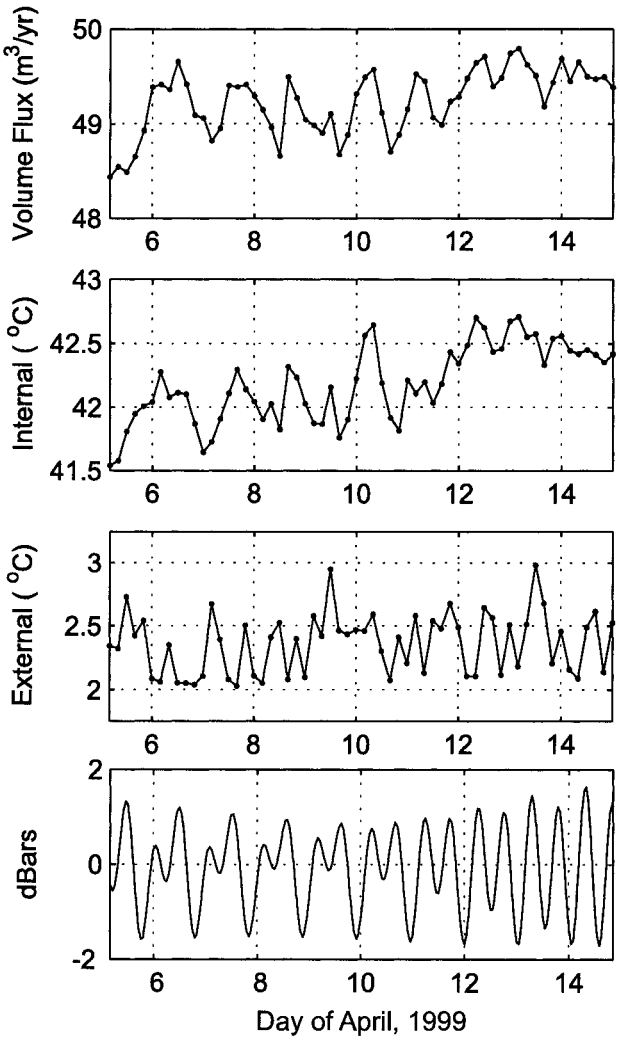

Figure 3.4: Data plots showing a ten day record of (a) volume flux, (b) temperature of the effluent fluid, (c) external thermistor recording background water temperature and (d) the modeled tidal variations utilizing a near pressure recorder [54].

Although these measured flow rates are low, and the tidal range in this area can be substantial (e.g., Figure 3.4c), it is important to note that the flow out of the seafloor in this location remained positive at all times (i.e. there were no flow reversals when seawater flowed into the seafloor). Examination of shorter time intervals (see Figure 3.4 for an example) indicates some consistent variance in both the internal temperature and flow measurements at roughly daily time scales. This variability may be related to poroelastic effects on the velocity of fluid through the seafloor interface, where the pore fluid pressure in the upper crustal rocks is responding to transient loading arising from the passing water tide [55]. Inferring the specific discharge associated with a tidal volumetric flux of roughly 0.5 m^3/yr daily variability over one square meter of seafloor equates to approximately 1.6×10^{-8} m/s. Using this as the Darcy velocity, a 2 meter water tide amplitude and a fluid viscosity of 6.4×10^{-4} Pa s, a formation scale effective permeability of order 10^{-12} m^2 is obtained. Caution should be used in interpreting this result however, since it has been assumed (but not demonstrated) that the daily variations observed in the effluent velocity and temperature are a direct result of the instantaneous loading of the passing ocean tide. Although the signals at periods of 24 hour and greater are strongly correlated, they are not well correlated at higher frequencies. In fact, examination of the spectra at tidal frequencies indicate that the neither the effluent temperature nor the velocity have significant enhancement of energy over the 206-day deployment interval at tidal frequencies (Figure 3.5). An alternative method to computing effective permeabilities is given in Section 3.5.

3.4 Heat flux

Since both the volumetric flux and the temperature of the effluent fluid have been measured, direct measurement of the heat flux from one square meter of a diffuse vent has been obtained in a manner analogous to previous direct measurements of heat

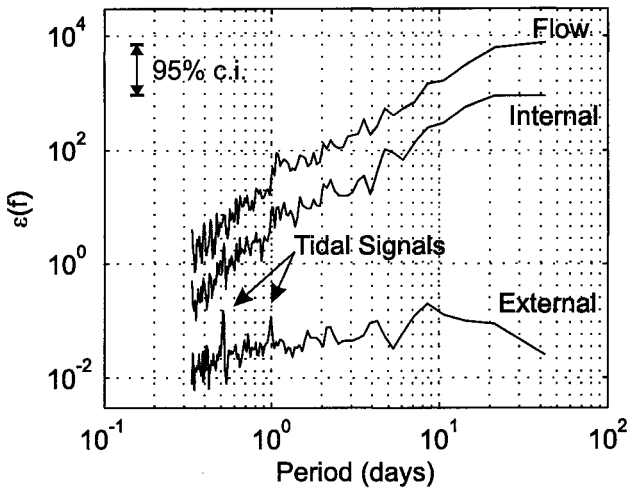

Figure 3.5: Normalized power spectral plots showing enhanced energy at tidal frequencies for the external temperature sensor and very little tidal energy in the internal flow and temperature measurements. The spectra were offset for image clarity.

flux from the high temperature point sources,

$$Q_H = \frac{\rho c_p q(T - T_0)}{A}, \tag{3.3}$$

where Q_H is the heat flux, ρ is the density of fluid, c_p is the specific heat of the fluid, q/A is the specific discharge and $(T - T_0)$ is the temperature difference between the bottom water and the hydrothermal fluid. Both the fluid density and the specific heat are functions of temperature, salinity and pressure and therefore vary throughout the instrument deployment. In this experiment the hydrothermal fluid density ranged from 1021.7 to 1025.3 kg m^{-3}, and the specific heat ranged from 3986.1 to 3992.1 J kg^{-1} $°C^{-1}$.

Our measured heat flux varied from 200 to 300 W/m^2 over the deployment interval, with a mean heat flux of 260 W/m^2. In 1987, *Rona and Trivett* [23, 56] measured diffuse heat flux in this area utilizing plume measurements within the bottom boundary layer. They obtained estimates of diffuse heat flux that ranged between 22 to 57 kW/m^2 over nearby diffusely venting areas, and estimated that the total component

of diffuse heat flux for the ASHES vent field was 15–75 $\times$ 10^6 W. This prior study did not however record a water column plume above the *crack vents* where the cement box is located, nor were they able to estimate magnitude of the diffuse heat flux for this specific site. This indicates that the area sampled by the cement box may not be characteristic of the magnitude of diffuse flow within the ASHES vent field in general, and may have broader implications. In order to obtain two orders of magnitude higher heat flux (and therefore volume flux assuming roughly equivalent effluent temperatures), significantly higher effective permeabilities would be required over relatively short spatial distances ($\sim$50 meters). The disparity between these two estimates also highlights the well-known spatial and temporal variability of diffuse venting, where it is common for the temperature of the fluid exiting the crust to vary by 10s of degrees over a spatial scale of decimeters and temporal scales as short as weeks.

3.5 Darcy flow approximation

Since previously (in Section 3.3) the daily variation in the specific discharge to estimate formation scale permeabilities of order 10^{-12} m^2, it would be useful to examine whether the measured flow indeed meets the required assumptions for Darcy's law for fluid flow in a porous media. The critical assumption in Darcy's law is that the flow within the substrate must be laminar. In order to examine this assumption, the Reynolds number of the flow within the substrate can be estimated using the formulation for flow within a pipe [57]. It has been shown experimentally for pipes and open channels that if $Re \ll 2300$, the flow can be considered laminar. Within an aquifer however, where the roughness of the flow path is large and the flow path very tortuous, a $Re < 10$ is usually required to ensure laminar flow. The Reynolds number is defined as

$$Re \equiv \frac{\rho \overline{u} D}{\mu}, \tag{3.4}$$

where Re = Reynolds number, ρ = density of the hydrothermal fluid, $\overline{u}$ = mean velocity per unit area, D = pipe diameter and μ = fluid viscosity. Examining the Reynolds number for flow within the subsurface reservoir, utilizing the specific discharge of 1.5×10^{-6} m/s and the same fluid density and viscosity used above, and crack widths less than 1 meter in dimension yields a $Re < 10$. These calculations support the expectation that sub-surface flow in the crust below the cemented box should be laminar.

This laminar flow in the substrate is however focused from the one square meter sampling area at the seafloor interface to a 1.27 centimeter sampling pipe. Computing the Re for the flow within the measurement pipe (using an equivalent volume flux as above, or $\overline{u}$ = 1.2 cm/s, a mean hydrothermal fluid density of 1023 kg/m^3 and $\mu = 6.4 \times 10^{-4}$ Pa s), a $Re \gg 2300$ is obtained, indicating flow within our measurement pipe should be fully turbulent. This result is supported by the spectra showed in Figure 3.5, where obtaining an approximate wavenumber spectra by scaling with the mean velocity of 1.2 cm/s yields the expected slope for turbulent flow of approximately -5/3. So while the subsurface flow was likely laminar (the region of interest for all the following calculations), the flow actually measured in the sampling pipe was turbulent.

Measurements of the Darcy velocity can be used to directly compute the effective permeability of the substrate using Darcy's equation of fluid flow,

$$\overline{u} = -\frac{k}{\mu}\left(\frac{dP}{dz} - \Delta\rho g\right), \tag{3.5}$$

where k is the permeability, μ is the viscosity of the hydrothermal fluid, P is the reduced or non-hydrostatic pressure, $\Delta\rho$ is the density contrast between seawater and hydrothermal fluid, g is the gravitational acceleration and $\overline{u}$ is the Darcy velocity. If fluid within the crust is hydrostatic and the background vertical pressure gradient is zero, then the permeability estimated from equation (3.5) ranges from 1.0×10^{-11} to 7.8×10^{-12} m^2. This permeability is however highly correlated with the effluent fluid temperature (see Figures 3.3 and 3.6). Relaxing the constraint of zero background

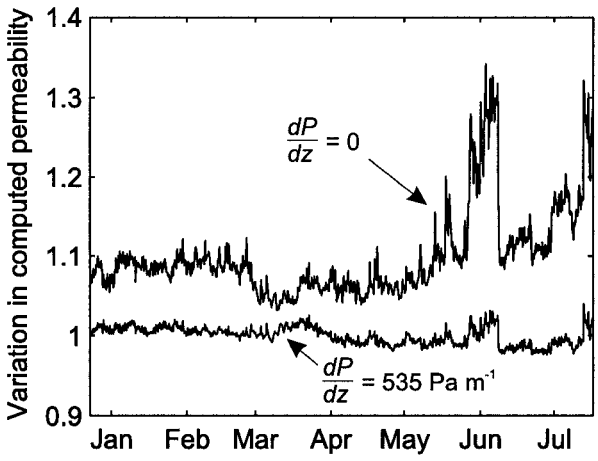

Figure 3.6: Normalized variation in computed permeability found by repeatedly solving equation (3.5) and dividing result by the median computed permeability over the deployment interval. The $\frac{dP}{dz}$ =0 case has been offset by 0.05 for clarity.

vertical pressure gradient, and instead iteratively solving equation (3.5) with the best fit determined by minimizing $\| k_i - \overline{k} \|$, a mean overpressure equivalent to 535 Pa m^{-1} reduces the variance of the estimated permeability to less than 4%. This strategy produces a significant improvement during the last 90 days of deployment when there is a substantial variation in effluent temperature. The calculated overpressure would contribute approximately 4 times the driving force, with respect to fluid buoyancy alone, to the measured effluent velocity and would reduce the average required permeability to 1.5×10^{-12} m^2. Driving fluid flow with the overpressure alone would yield Darcy velocities of 1.25×10^{-6} m/s (or 1 to 3 m/day within the subsurface cracks).

It is not obvious what process would cause the calculated, non-thermal, overpressure in this system. The geopressuring of fluid in sedimentary basins has however been well studied and some of the most common processes associated with these systems may be analogous to the process(es) that are present in this hard-rock system; (1) aquifer head, (2) tectonic compression, (3) loading / compaction with the absence of adequate drainage systems, and/or (4) intrusion of gas or fluid phase-changes. A

general requirement for the anomalous subsurface pore fluid pressure is the presence a subsurface permeability barrier that is effectively preventing, or greatly restricting, free fluid flow. It may be that the large sheet-like lava flow, upon which the sampling box is deployed, acts as an effective permeability barrier (cap rock). Other subsurface permeability barriers, including biological films or gas bubbles, cannot be excluded however.

Although the flow from the cemented box is only mildly overpressured (535 Pa m^{-1} is equivalent to transferring an additional load of 5 cm of water or 2 cm of rock to the fluid), the constant geopressure dominates the measured effluent fluxes in this low-flow hydrothermal system. It is also significant that over the course of the 206-day deployment there is no requirement for time-dependent changes in the measured effective permeability. If the upper crustal permeability is constant over this interval, it implies that the observed temporal variability in diffuse flux (mass, volume and heat) from the cemented box is a consequence of changes in (1) the subsurface mixing, (2) the geometry of the flow paths, or (3) the addition of 'new' heat to the hydrothermal system.

3.6 Summary

The volumetric and heat fluxes of a diffuse vent have been measured using the direct coupling provided by an interface cemented onto the seafloor of an active volcano on a mid-ocean ridge. Volume flux of the low-temperature hydrothermal fluid is approximately 48 m^3/yr and indicates upwelling flow velocity within the subsurface at 1–4 m/day. An effective permeability of $1.5\times\ 10^{-12}$ m^2 for the uppermost crustal rocks of the seamount is estimated and a significant, time-invariant contribution to the pressure gradient from a non-thermal process has been documented. The measured permeability is surprisingly consistent over the 206-day deployment, without any indication of significant changes in the subsurface plumbing during this time. Our flux

measurements are consistent with an oscillatory poroelastic-driven flow ($\sim 1.5 \times 10^{-8}$ m/s) through the rock/water interface. This oscillatory (tidal) flow, however, constitutes less than 1% of the total flow volume from the box, and would only represent approximately 5% of the volume flux if the overpressuring of the effluent fluid was relieved. It is likely however, that other diffusely venting areas (with higher effective permeabilities) may be experiencing significant tidal modulation of their mass and energy fluxes on tidal timescales. Although the cemented-box has allowed us to tightly characterize a small diffuse hydrothermal zone and shown the potential importance of non-thermal buoyancy terms in low-flux deep-sea hydrothermal systems, the obvious diversity of diffusely-venting areas and our limited spatial sampling severely limit the broad generalization of these results.

Chapter 4

BOUNDARY LAYER OBSERVATIONS

Measurements obtained over the past few years aimed at determining the heat flux of diffuse hydrothermal vents have provided several insights into the way in which this heat is transferred into the deep ocean boundary layer. These results are not only significant for predicting the magnitude of heat transfer from this type of hydrothermal venting, but also in understanding how other biological and chemical properties are distributed in the ridge-axis environment. There are three ways in which hydrothermal fluid typically exits the seafloor; (1) focused high-temperature vents, (2) diffuse seepage of hydrothermal fluid through, or closely associated with vent structures, or (3) low-temperature, diffuse flow that occurs distant from focused vent structures. Initially, high-temperature focused vents drew the most attention, since this type of venting is easier to detect with water column surveys, and also because the focused nature of flow from the structures made it (somewhat) easier to estimate mass and energy fluxes. Even so, the scale of measurement is difficult to obtain using deep-diving submersibles and/or remotely-operated vehicles at the seafloor. Sulfide structures have been documented up to 50-m tall, and each structure may consist of several, to dozens, of individual high-temperature vent orifices [58].

A high-temperature vent site is defined to consist of at least one *smoker* vent, $> 215°C$, however the actual number may be much larger [77]. For example, the Main Endeavour vent field (which is included in this study) consists of over one hundred individual vent orifices, and covers an area greater than 0.2 km^2 [59, 60]. Temperature and velocity measurements obtained within a few centimeters of focused vent orifices yield power outputs which range from less than 1 to nearly 100 MW, and effluent

fluid velocities between 0.1 and 2 m/s [23, 61, 62]. Complicating the estimation of vent-field scale fluxes from point-source measurements is not just the difficulty in locating and documenting all the different vent sources, but also the variability in the dimensions and geometry of the vent orifices themselves. While typical orifices are only a few centimeters across, some have been documented to be as large as 30 centimeters in diameter [62].

Thus many investigators have instead focused on measurements of buoyant or neutrally-buoyant plumes above the vent fields, and thereby obtain a more naturally integrated estimate. Buoyant plumes from individual orifices may (or may not) merge as they rise vertically through the water column. Either way, the plumes entrain background fluid from near the vent structures and throughout their ascent [63, 64]. Typically, plumes from high-temperature, focused hydrothermal sources rise several of hundred meters above the seafloor before reaching a height of neutral buoyancy, although the actual rise heights are determined by the buoyancy flux, background stratification, configuration of the source(s) and strength of the bottom water currents [65, 66, 67]. After the plumes reach a height of neutral buoyancy, the fluid is advected away from the source area with the prevailing ocean currents at that depth [26, 68, 69, 70]. We know that this fluid is broadly distributed throughout the ocean basins, as chemical *signatures* of the high-temperature source fluid within these plumes are found 1000s of km from ridge axes [71].

However, it is currently unclear to what degree the diffuse, lower-temperature flow near the sulfide edifices is entrained into these plumes. Preliminary field observations, which measured both the point sources and the buoyant plumes above hydrothermal structures, seemed to indicate that diffuse effluent near hydrothermal structures may not necessarily be entrained into the focused-vent source plume [62, 72]. This is significant since diffuse flow near vent structures can be substantial, and if it is entrained into the high-temperature plumes, then it is included in heat estimates obtained from water column surveys of neutrally-buoyant plumes. Diffuse percolation of hydrother-

mal fluids through or closely associated with hydrothermal structures may represent anywhere from one to five times the heat flux dissipated by the focused vent sources themselves [23, 24, 26, 29, 31]. The effluent fluid velocities for this type of hydrothermal venting can also be substantial, with direct observations ranging from 0.005–0.15 m/s [23, 31, 32, 33, 34, 35].

The determining factors in the entrainment of background fluid near a vent structure may be the configuration of distributed high-temperature sources, and the mean speed of the bottom currents. Acoustic imaging of deep-sea hydrothermal plumes, as well as numerical simulations, show inward flow consolidation—a point of minimum radius—above distributed sources [67, 64, 73, 74]. Thus they predict enhanced entrainment of fluid from the bottom boundary layer as the source area is expanded. There will also be a point of maximum vertical velocity associated with the 'neck' of the plume, below which the fluid is accelerating and above which it is decelerating [75]. However, given the substantial volume and heat flux predicted for diffuse percolation through sulfide structures, it is likely the buoyancy flux from this type of venting is significant enough to obtain a substantial rise height, even when not entrained into focused vent plumes. Estimating the partitioning of diffuse and focused flow fluid within neutrally buoyant plumes therefore requires detailed modeling and mapping of source configurations and flux rates, and would likely require additional constraints provided by chemical or biological tracers [29]. Unfortunately, this leads us to conclude that an *a priori* estimate of the relative partitioning of distributed and focused vent fluids in the neutrally-buoyant plume is not feasible.

Lower-temperature, diffuse flow that is tens to hundreds of meters away from focused vent structures is well outside the defined source region of high-temperature vent sources, and thus this fluid is unlikely to be (initially) drawn into the high-temperature plumes [76]. Basalt-hosted, diffuse flow of this type generally has effluent temperatures which are less than 35 °C [77] and a single measurement from one of these vents showed exit velocities which were less than 5×10^{-5} m/s [2]. Much larger

flow rates of 2–10 l/s were measured in concentrated flow regions of similar vents on the Galápagos Rift by *Corliss et al.* with vent fluid temperatures of up to 17 °C, but they were unable to determine the area of the vents [33]. Buoyancy flux from low-temperature diffuse vents of this type is thus likely to be sufficiently small that their plumes will be blown over by bottom currents (which are of order 2–20 cm/s) and transported along the rock / water interface [23, 30, 78]. A simple numerical model developed to examine low-temperature diffuse venting predicts for a wide range of conditions (a) the rise height of these plumes will be less than their source dimension and (b) the plume may be transported a substantial distance while still maintaining contact with the rock / water interface [56]. The eventual fate of this hydrothermal fluid remains uncertain, although studies have shown signatures of this fluid are still contained in the bottom mixed-layer several kilometers from their source regions [78].

The present work describes a synthesis of heat flux data collected over three years along the Endeavour Segment of the Juan de Fuca ridge. The focus of this study is low-temperature, basalt-hosted diffuse vents away from high-temperature focused vents. Diffusely venting patches of the seafloor are examined in four separate vent fields along a 2.5 km length of ridge axis (see Figure 4.1). Vertical heat flux measurements were obtained at ~0.5 m height above the seafloor, both within and outside areas of active hydrothermal venting. In the next section, we describe the percolation of hydrothermal fluid through the upper basaltic crust as well as the fundamental aspects of heat transfer into the near-bottom oceanic boundary layer. Section 4.2 describes how the low-temperature fluid is mixed into the bottom boundary layer and sets the context for our observations near the rock / water interface. In section 4.3, a description of our turbulence instruments is given, including velocity calibration. The turbulence observations are then described in section 4.4. The time and space scales and the form and distribution of turbulent eddy heat flux are shown for a range of heat flux magnitudes. These results show similar form for the different vent fields, most likely indicating the influence of similar geologic constraints on the advection of

fluid (and thus heat) within the upper oceanic crust. Lastly, we compare statistical extrapolations of the turbulent eddy heat flux estimates with previous studies of hydrothermal heat flux in the ridge-axis environment.

4.1 Rock / water interface

The thermal energy that drives the circulation of low-temperature fluids through the upper oceanic crust has the same source (i.e. the formation of the new seafloor) as the high-temperature systems, yet much less is known about its spatial, temporal and physical variability. The sub-surface flow-path, mixing history and geochemistry of diffuse effluent fluid has remained ambiguous. Low-temperature fluids near focused vent structures may be (1) conductively-heated seawater, without large geochemical modification, (2) a mixture of high-temperature effluent with seawater or other reservoir fluid or (3) some combination of these two processes [34, 79, 80, 20]. Secondary processes such as mineral precipitation and / or dissolution [79, 81], re-equilibration of the vent fluids with the host rock at low temperature [82], or sub-seafloor biological processes [83, 84] may also affect the temperature–chemistry relationship of the hydrothermal fluid prior to discharging into the ocean. Given these ambiguities, substantial uncertainty remains in estimating the magnitude of mass and energy transport from low-temperature, diffusely venting regions of the seafloor. While one recent study [80] showed that more than 90% of the heat flux along one segment of the Mid-Atlantic Ridge is dissipated by conductively heated seawater or simple thermal conduction—with little or no geochemical modification—all studies which have examined geochemical data from ridge-axis diffuse fluids as they discharge from the seafloor, support the involvement of a high-temperature source fluid [20].

Systematic, quantitative data on the prevalence and distribution of basalt-hosted, diffuse venting along spreading axes is currently lacking. However it is clear that considerable variability in the surface expression of venting of this type occurs between,

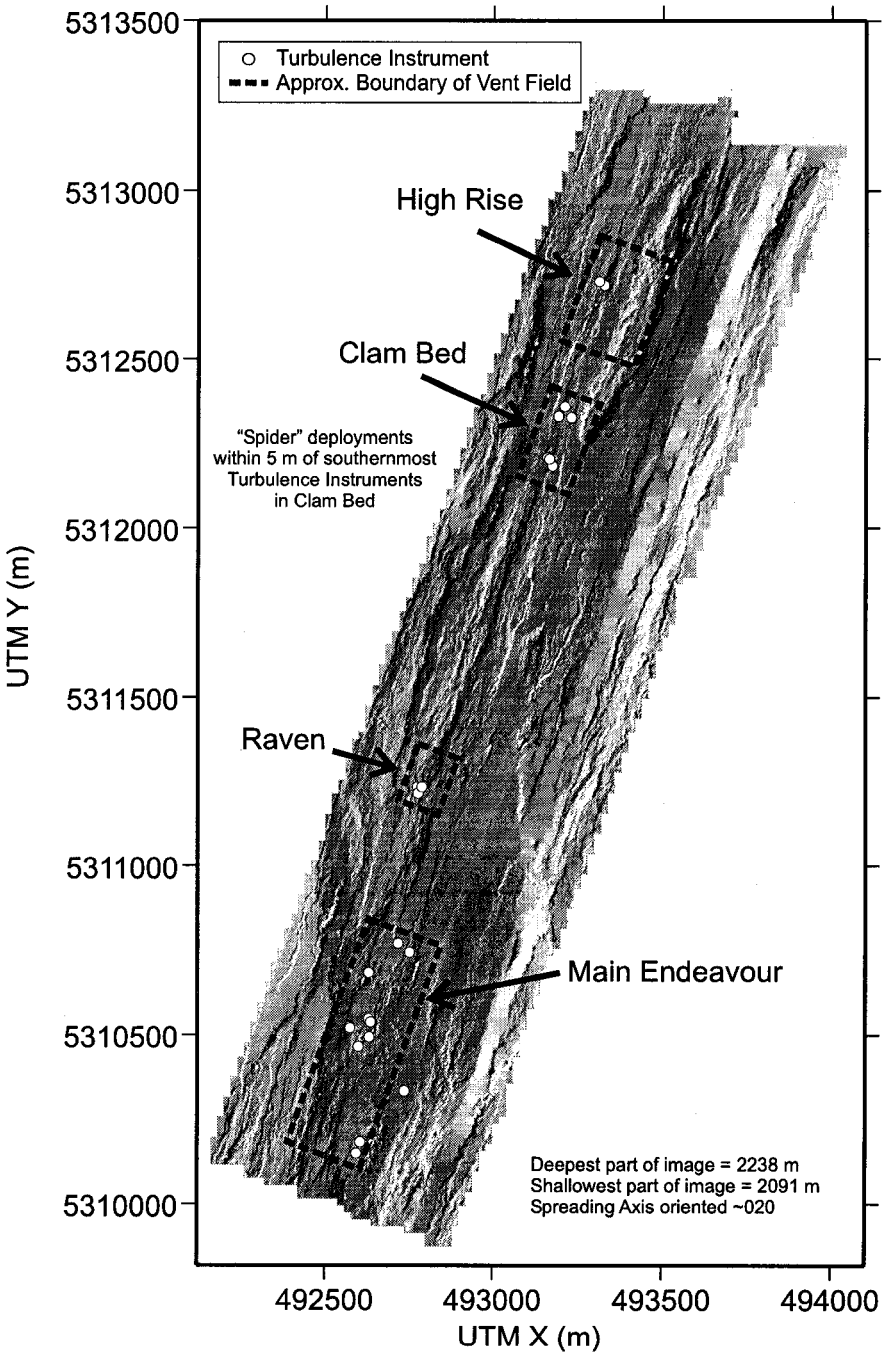

Figure 4.1: Location map of the Endeavour Segment on the Juan de Fuca Ridge. High Rise and Main Endeavour fields are the most active of the four vent sites shown. Each has over 10 large sulfide structures displaying vigorous venting. In contrast, the Raven and Clam Bed fields exhibit relatively large areas of low-temperature, basalt-hosted diffuse flow, yet each contains three or less structures exhibiting focused venting. The above bathymetry is from a high-resolution survey collected in 2000 and 2001 [113].

and within, active vent sites. Most low-temperature, basalt-hosted venting occurs as small patches (a few meters in diameter) of flow that appears to be associated with local variability in the permeability of the rock structure—with the majority of flow occurring either along surface cracks or near regions of active faulting. However, much larger regions of venting do occur. The Clam Bed vent field (see Figure 4.1) is host to a large, 30 m $\times$ 50 m, area of diffuse venting. The region of active venting can clearly be delineated by the presence of an extensive tubeworm community. A small high-temperature, greater than 215 °C, vent is located near the center of this diffuse patch, but measurements of the temperature of the basalt-hosted flow are all still less than 30 °C.

Substantial variability in rock surface temperature does exist within the patch of diffuse venting however. In fact, measurements showed high variability even at decimeter scales. A collection of temperature measurements obtained using a 1-m triangular array of thermistors, which were kept in direct contact with the seafloor using spring-loaded pistons, showed variability of more than 10 °C over less than twenty centimeters (Figure 4.2 and Table 4.1), although there was no visual evidence in variability of the health of the tubeworms within the sampled areas (J. Voight, pers. comm., 2001). These observations demonstrate that at the rock / water interface, diffuse vents are more analogous to a collection of small micro-plumes emanating from discrete cracks than a large distributed heat source. To better understand how these microplumes mix into the bottom boundary layer requires more information on the buoyancy of the hydrothermal fluid as it leaves the crust and the rate at which the fluid is supplied to the interface. This is typically expressed as the surface buoyancy flux,

$$B_0 = b_0 w_0, \tag{4.1}$$

where b_0 is the vertical buoyancy, $b = (g/\rho)\rho'$, and g is the acceleration of gravity. Fluid density, ρ, is determined by the salinity, temperature and depth of venting. Generally, diffuse fluids have salinities near background seawater values (D. Butter-

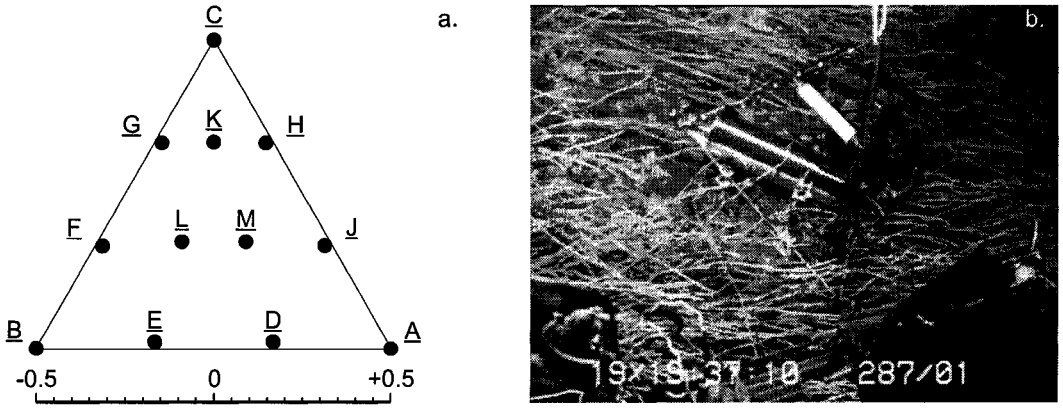

Figure 4.2: (a) The "spider" instrument was designed to examine the spatial variability of surface temperature at the rock / water interface on the scale of decimeters. Twelve high-resolution thermistors were deployed over less than 1 m^2 of seafloor with spring-loaded contact plungers (see Table 4.1 for data). (b) The five deployments were all within a large tubeworm field in the Clam Bed vent field.

field, pers. comm., 2003), so for our calculations we have assumed the density contrast is due only to thermal effects. Thus we can write $b = g\alpha\Delta T$, where α is the coefficient of thermal expansion and ΔT is the temperature differential between the warm hydrothermal fluid and the cool background seawater. In point-source plume models, the total source buoyancy flux, $\hat{B}_0$, is the important factor, therefore the source volume flux is used instead of the mean velocity of the venting fluid, $\hat{B}_0 = b_0 w_0 A$, where A is the cross-sectional area of the source.

The geology of the upper oceanic crust places important constraints on the volumetric fluid flow rate out of the basaltic crust, and thus has a large impact on the measured surface buoyancy flux. Similar to flow in the ocean, the vertical velocity of fluid within the porous media is controlled by the vertical buoyancy and the resistance to flow, in this case primarily the capacity of porous rock to transmit the fluid. Unfortunately, there is a large range in the measurements and estimates of the transport efficiency of the upper oceanic crust [37]. However, it is possible to broadly constrain the velocity of the hydrothermal fluid as it flows through the crust. From

Table 4.1: Mean temperatures over deployment interval for twelve contact thermistors deployed within a tubeworm vent field. Thermistor accuracy was 0.002 °C, although only 0.1 °C is shown for clarity. Deployment times are given with day in the month of June, 2001, followed by the time in UTM.

Thermistor†	Dep. 1	Dep. 2	Dep. 3	Dep. 4	Dep. 5
A	2.2	—	—	—	—
B	>18	2.2	5.8	7.0	—
C	2.2	2.2	2.9	2.0	—
D	—	—	—	—	—
E	>18	2.8	2.0	7.9	6.7
F	7.5	5.8	2.3	2.0	3.4
G	4.9	3.8	2.9	2.0	7.1
H	3.0	2.7	2.3	2.5	6.7
J	4.3	2.2	2.3	2.0	5.7
K	2.1	1.9	1.9	2.0	2.2
L	7.8	>18	2.0	2.5	2.4
M	6.6	5.9	2.0	2.1	6.2
$t_{deployed}$	19 14:00	19 16:50	19 19:50	22 04:30	24 23:40
$t_{recovered}$	19 16:40	19 19:38	22 04:23	24 23:10	25 04:12

†See Fig. 4.2 for thermistor locations.

Darcy's Law for fluid flow in a porous media, the one-dimensional volumetric flow rate per unit area, $\overline{w}$, which is driven by the vertical pressure gradient, dp/dz, due to the buoyancy of the hot hydrothermal water, can be expressed as

$$\overline{w} = -\frac{K}{\mu}\frac{dp}{dz} \approx \frac{K\rho_0 b}{\mu}, \tag{4.2}$$

where K is the permeability of the host rock, μ is the dynamic viscosity of the fluid and ρ_0 is the density of the background seawater.

The vertical flow rate and temperature of the effluent fluid also directly determine the flux of heat through the seafloor interface, i.e.

$$Q = \rho c_p \overline{w} \Delta T, \tag{4.3}$$

where c_p is the specific heat capacity of the fluid. Comparing equations (4.2) and (4.3) demonstrates the interplay between geologic properties and the heat flux measured at the surface. In Figure 4.3, the specific discharge of fluid through the seafloor is plotted as a function of hydrothermal fluid temperature. It shows that for the range of heat flux estimates for diffuse hydrothermal flow, hundreds to tens of thousands of W/m^2 [2, 23], the specific discharge of fluid over the diffusely-venting region is between 10^{-3} and 10^{-6} m/s, and that the effective permeability of the uppermost rock matrix must be between 10^{-8} and 10^{-11} m^2.

If we are interested in estimating the effect of the individual micro-plumes emanating from the cracked surface of the basaltic basement rocks, then it is important to realize that the specific discharge calculated above is not the actual velocity of the fluid as it departs from the seafloor, w_0. The fluid in the rock matrix is constrained to flow only within the open space of the porous media, so a geometric scaling is required to translate the specific discharge into the actual fluid velocity within the cracks in the substrate. Allowing for laminar flow, the scaling factor depends on the porosity of the media, ϕ, and also the geometry of the fluid flow paths accessible for vertical flow. Simple permeability models yield scaling factors between $1/\phi$ and $3/\phi$,

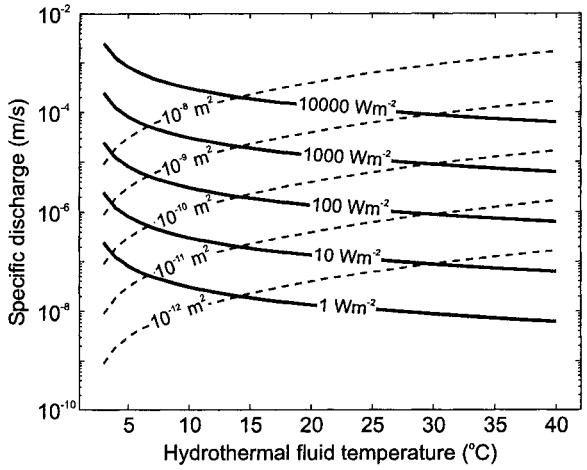

Figure 4.3: Volumetric flow per unit area of seafloor, $\overline{w}$, for different hydrothermal fluid temperatures at different crustal permeabilities (dashed-lines) or heat fluxes (solid-lines). Pressure gradient within the crust is assumed hydrostatic and all the buoyancy is thermally-derived, i.e. the salinity of the hydrothermal fluid is assumed equal to seawater.

although larger scaling factors are possible if the majority of the open pore space is unavailable for fluid flow [85]. Ocean bottom gravity surveys have shown that the porosity of young uppermost oceanic crust ranges from 9–38% [8] and a recent gravity survey estimated that a mean porosity for the upper 130 meters of basaltic crust for the Endeavour Segment at the upper end of that range [86]. Thus while Figure 4.3 shows that if the advective heat fluxes from diffusely venting regions are of order 1000s W/m^2, the volumetric flow per unit area is of order 10^{-4} to 10^{-5} m/s; using the above correction factors, this translates into interstitial pore fluid velocities which are as much as ten times larger, but are still $\ll$ 1 cm/s. These calculations demonstrate that the vertical velocity of the effluent hydrothermal fluid from this type of venting is likely to be small in comparison to the typical horizontal velocities of bottom water, which are of order 2–20 cm/s.

Before we cross the rock-water interface and examine the near-bottom turbulent boundary layer, it should be noted that the gradients in surface temperature shown

in Figure 4.2 and Table 4.1 are unlikely to extend to substantial depth within the rock matrix. This is an important point since the heterogeneity seen at the surface is not likely to represent heterogeneity in the upwelling source fluid below the surface. The thermal capacity of the rock matrix would quickly dissipate any excess thermal energy carried by the hydrothermal fluid. To demonstrate this point, we can estimate the surface heat flux between cracks within an otherwise uniform, un-broken block of basalt, using Fourier's law of heat conduction. The heat flux through the basalt matrix can be written as

$$Q = -\Lambda \left(\frac{\partial T}{\partial y} \right)_{y=0}, \tag{4.4}$$

where Λ is the thermal conductivity of basalt, $\sim$2.4 $\mathrm{Wm^{-1}K^{-1}}$, and T is the temperature of the rock matrix. Thus two cracks separated by 20 cm—one with its rock surface maintained by upwelling hydrothermal fluid at $\leq$ 30 °C, and the other maintained at 2 °C—would dissipate enough thermal energy to cool the volume of seawater in a 2-cm wide crack by an amount equivalent to the entire difference in fluid temperature in less than two hours. The actual rate of thermal dissipation in oceanic crust would likely be substantially greater. Even though the rock is likely to be fractured, and therefore have a lower effective thermal conductivity [1], the fluid flow paths within the rock are unlikely to be constrained to cracks as large as 2-cm. Thus the rock-water surface area, and consequently the interfacial heat transfer rate, is likely to be much larger than for the uniform block calculation above [3, 87, 88]. Therefore the observed gradients in rock surface temperature are likely due to variability in the surface permeability structure and near-surface mixing of the upwelling hydrothermal fluid with seawater, and not different reservoirs of upwelling hydrothermal fluid. These results imply that the uppermost basaltic rock likely represents the most heterogeneous region of temperature and fluid chemistry—since below the surface, large temperature gradients within the upper basaltic crust cannot be maintained; and above the surface, mixing processes quickly homogenize any variability in

fluid properties.

4.2 *Diffuse hydrothermal plumes*

Utilizing these results, we can examine the importance of the geometry and initial momentum of the individual micro-plumes in a cross-flow current. At distances $x \gg L_M = (w_0 u)/b_0$, the effect of the initial momentum of the plumes is negligible, and at $L \gg r_0$, where r_0 is the radius of the source, initial geometry effects are negligible [89]. Assuming a minimal salinity contribution and hydrothermal fluid temperatures between 3 and 40 °C, b_0 would range between 10^{-3} and 10^{-1} m/s^2. Using conservative over-estimates for the bottom water velocity, $u \sim 10^{-1}$ m/s, and the effluent fluid velocity, $w_0 \sim 10^{-3}$ m/s, gives $L_M < 10$ cm. Given that the individual sources are also constrained to small areas (see Figure 4.2 and Table 4.1), initial geometry effects of the micro-plumes are also fairly localized. Thus the geometry and initial momentum of the individual micro-plumes from low-temperature diffuse sources does not greatly impact the plume dynamics at measurement heights greater than several tens of centimeters.

While it is therefore more appropriate to discuss diffuse plume dynamics as originating from a distributed source area [90], we will first look at the more well-studied point-source plumes, since the impact of a cross-flow current has been examined in more detail for point-sources, and also to facilitate comparisons with the high-temperature focused source plumes. Observational and laboratory studies for point-source plumes rising in a non-rotating, stratified environment with no cross-flow have shown that the maximum rise height [63, 91, 92] is

$$z_{max} \approx 3.75 \left(\frac{\hat{B}_0}{N^3} \right)^{1/4}, \tag{4.5}$$

where N is the buoyancy frequency,

$$N = \left(\frac{g}{\rho} \frac{d\rho}{dz} \right)^{1/2}. \tag{4.6}$$

Typical values of N are 7.35×10^{-4} s^{-1} and 1.68×10^{-3} s^{-1} for the depth range of 2100–2300 m in the Atlantic and Pacific oceans, respectively [65]. Similarly, recently obtained vertical CTD casts near our study area along the Endeavour Segment of the Juan de Fuca Ridge [69] yielded average values for N of 2×10^{-3} s^{-1} and 1.5×10^{-3} s^{-1} for observations above and within the near-bottom geothermal boundary layer, respectively. Our surveys in 2001 and 2002, utilizing a CTD mounted on the remotely-operated vehicle *Jason*, found N less than 1×10^{-3} s^{-1} near the floor of the axial valley, generally between 1 and 1.5×10^{-3} s^{-1} for the next 300 meters and approximately 2×10^{-3} s^{-1} for observations above 400 meters above the seafloor (see Figure 4.4 for an example profile taken above the central valley instrument deployment site). A near-bottom low stability layer, which we define as the region below which the squared buoyancy frequency is less than a prescribed limit, in our case $N^2 < 1 \times 10^{-6}$ s^{-2}, was found to be generally < 35 m in vertical dimension.

Salinity variation is an important contributor to the source buoyancy flux of high-temperature systems, where high-temperature hydrothermal fluid salinities range from 0.1 to 2 times that of seawater [20]. Given this complication and constrained by point source measurements at the seafloor, the range of source buoyancy fluxes used in numerical simulations is between 0.1 m^4/s^3 for individual vent sources to 2.1×10^{-3} m^4/s^3 for distributed (100 m^2) sources [65, 91]. Using this entire range, one would expect rise heights anywhere between 80 and 375 m. However, the rise height of hydrothermal plumes is also sensitive to the cross-flow current [91, 92, 93] and from atmospheric observations it has been shown that

$$z_{max} \approx 2.6 \left(\frac{\hat{B}_0}{uN^2} \right)^{1/3}. \tag{4.7}$$

For a cross-flow velocity, u, of 0.2 m/s, and using the other values from above, the minimum of the estimated rise heights would decrease to approximately 60 meters above the seafloor.

Mixing depths for the distributed sources have primarily been studied from the

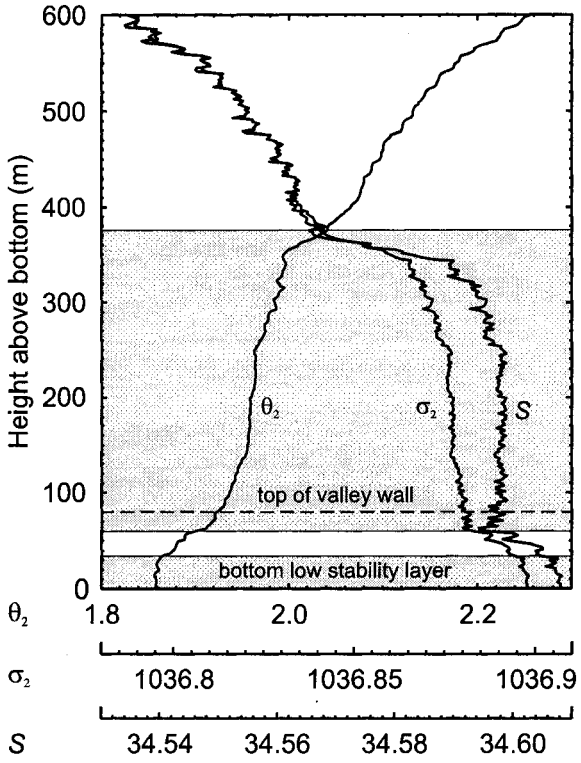

Figure 4.4: Potential temperature (θ_2), potential density (σ_2), and salinity (S) profile above the central valley deployment (see Figure 4.1) obtained using a CTD mounted on the ROV Jason. A bottom low stability layer and range of rise heights predicted for high-temperature focused vent sources are shaded. The depth of the top of the axial valley wall is shown with a dashed line.

perspective of generating deep and intermediate water sources at high latitudes. Numerical simulations and laboratory studies [90, 94, 95, 96] have shown that in a stratified ocean, the maximum depth (or in our case, height) of penetration is related to the radius, r_0, of the source region,

$$z_{max} \approx 3.9 \frac{(B_0 r_0)^{1/3}}{N}. \tag{4.8}$$

Given the large range possible for surface buoyancy fluxes and radii of diffusely venting patches of seafloor, rise heights anywhere up to ~ 75 meters are reasonable. But for a typical diffuse patch of a few meters in diameter, a surface heat flux of a couple thousand W/m^2, and a buoyancy frequency of 1×10^{-3} s^{-1}, the generated plume would

reach a maximum height of 40 meters. However, cross-flow effects and an increase in the buoyancy frequency above the near-bottom low stability layer would likely decrease the maximum plume height somewhat. Thus, one may expect some vertical separation between the high-temperature and lower-temperature diffuse plumes as they advect away from their respective source regions, although overlapping between the plumes is still feasible. It should therefore be possible for water column surveys to differentiate between the two different source regimes, if surveys are extended to very near (perhaps, impractically near) the seafloor.

4.3 Instrumentation and data collection

Vertical heat flux estimates were obtained at approximately 0.51 m height above the instrument base, although there is substantially roughness in the seafloor which may cause an effective zero plane displacement. The on-bottom deployment intervals ranged from 5 hrs to 322 days (see Table 4.2). Shorter term deployments recorded continuously at 2 or 5 Hz, while year-long deployments were configured to record bursts of 180–320 samples at 2 Hz every hour. Each turbulence sensor package consisted of a central data logger which recorded synchronous measurements of temperature (3 point measurements within 0.8 m hob) and three-axis velocity (nominally at 0.51 m hob). The instruments were deployed with a novel single-point mooring design, which enabled stable instrument deployments in areas of rough volcanic-pillow basalt terrain (Figure 4.5). This deployment system eliminated the effects of current meter motion by having rigid contact of the mounting system with the seafloor, and also allowed for placement of the instrument package in the very rough surface morphology associated with most diffuse venting areas. The instrument packages were generally not placed closer than 10–15 meters from actively venting sulfide structures. The thermistors are encased in individual titanium pressure housings and have a measurement range of -5 to $+45$ °C. Thermistor precision is 0.1 °C and the resolution is 0.03 °C. The

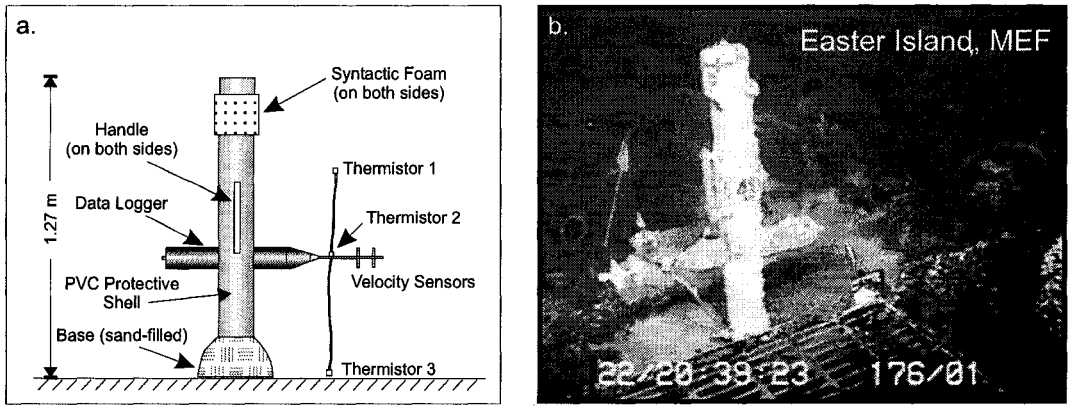

Figure 4.5: (a) Schematic of the single-point mounting system which was utilized for deployment of the turbulence sensors on the seafloor. The instrument retracted into the PVC housing when carried along the seafloor by the remotely operated vehicle. (b) Image of instrumentation during recovery after a one-year long deployment. Biological coating of the instruments was common during long-term deployments.

thermistors were calibrated prior to and following deployments utilizing a well-stirred ice bath which was slowly heated to 40 °C. The calibrations were verified by examining self-consistency within the thermistor chains during descent and ascent from the seafloor.

Acoustic velocity measurements were made using Nobska MAVS-3 [97]. MAVS have previously been used in the deep sea deployments [30, 98] because of their ability to measure small velocities with reasonably high accuracy (~0.3 cm/s). MAVS are differential time-of-flight velocity sensors and have a linear response function similar to the BASS instrument [99, 100]. This enables equal sensitivity at low velocities, but requires careful calibration to determine the zero-point. Each MAVS obtained zero-point measurements both prior and subsequent to the instrument's deployment [101]. During the initial deployment of our instruments, large (up to 4.5 cm/s) offsets were noticed between the pre- and post-deployment calibrations. We have found that all of our MAVS-3 instruments exhibited offsets during their first full-ocean depth immersion in salt water. In all subsequent deployments, the zero-velocity calibrations varied

Table 4.2: Deployment interval averages and ninety-five percent confidence intervals determined using the bootstrap method. Dissipation rate was estimated from the spectra by means of equation (4.16), other quantities were calculated directly from observations of velocity and temperature. Time intervals where frozen turbulence test failed were excluded from all averages shown.

Year	Δt (days)	Location	$\overline{u}$ (m/s)	$\overline{\rho c_p \langle w'T' \rangle}$ (W/m^2)	$\overline{u_*}$ (m/s)	$\overline{\varepsilon} \times 10^{-6}$ (W/kg)
2002	2.0	MEF†	0.038	4700 ± 660	0.014	6.81 ± 1.63
2002	3.0	Mid. Valley††	0.029	10 ± 2	0.005	0.22 ± 0.04
2002	1.5	MEF††	0.033	12000 ± 1400	0.014	5.17 ± 1.16
2001	4.0	Clam Bed	0.032	100 ± 590	0.012	6.18 ± 0.69
2001	2.5	High Rise	0.096	110 ± 75	0.011	4.89 ± 1.16
2001	1.7	MEF	0.065	38000 ± 6000	0.030	80.7 ± 11.6
2001	6.2	MEF	0.045	150000 ± 6600	0.038	232. ± 30.6
2001	5.8	Clam Bed	0.037	35000 ± 1800	0.020	17.8 ± 1.54
2001	2.5	High Rise	0.059	4 ± 6	0.008	3.08 ± 0.60
2001	5.3	MEF	0.020	9800 ± 1100	0.017	11.0 ± 2.58
2001	5.8	Raven	0.048	35000 ± 2200	0.020	21.6 ± 1.69
2001	5.8	Raven	0.027	3700 ± 270	0.014	10.8 ± 0.82
2000	3.0	MEF	0.028	620 ± 170	0.009	2.74 ± 0.52
2000	0.2	Clam Bed	0.033	750 ± 230	0.011	3.97 ± 1.57
2000	3.2	MEF	0.042	26 ± 23	0.009	3.40 ± 0.74
2000	3.2	MEF	0.033	3000 ± 580	0.015	9.34 ± 1.34
2000	2.9	MEF	0.032	710 ± 120	0.010	3.56 ± 0.50
2000	0.5	Clam Bed	0.041	13 ± 14	0.007	0.74 ± 0.40
2000	6.0	MEF	0.041	19000 ± 1400	0.022	46.5 ± 7.13
2000/1	251.2	MEF‡	0.025	2100 ± 160	0.013	19.7 ± 1.37
2000/1	253.6	Clam Bed‡	0.029	460 ± 54	0.007	5.09 ± 0.41
2000/1	256.6	Clam Bed‡	0.026	970 ± 40	0.010	7.06 ± 0.46
2001/2	242.7	MEF	0.032	1100 ± 72	0.011	6.41 ± 0.51
2001/2	291.0	Raven	0.039	2200 ± 180	0.011	8.32 ± 0.37
2001/2	321.7	MEF	0.046	2600 ± 120	0.011	8.33 ± 0.46

†See Figures 4.6, 4.7, and 4.8. ††See Figures 4.7 and 4.8. ‡See Figure 4.10.

by less than 0.3 cm/s from the initial post-deployment calibration values. We therefore believe that zero-offset drift for these instruments is small, and simply subtracted the post-deployment zero-point calibrations from all determinations of velocity.

The time-of-flight methodology for computing fluid velocities utilized by the MAVS current meters involves acoustic receivers which are spaced at distances of approximately 10 cm. But due to the use of four separate acoustic paths, the instrument has an effective sample radius of only a couple of centimeters. Small corrections to the computed velocities are required for variation in the sampled fluid temperature, and thus the velocity measurements are not entirely independent of the temperature measurements. A thermistor was located along the instrument shaft just outside the acoustic velocity sensor array. Examination of the spectra from a typical MAVS deployment (e.g., Figure 4.6) shows that the maximum scale of turbulent motion occurs at length scales of roughly 0.45 meters, where the angular wavenumber, $k = 2\pi f/\overline{u}$, is a function of frequency, f, and the mean current speed, $\overline{u}$. The velocity sensor typically falls off almost three orders of magnitude before reaching its resolution limit of a few centimeters. The temperature sensor falls off much more quickly due to its slow thermal time constant ($\sim$5 seconds), and thus has a lower resolution limit that is only capturing mixing lengths on the order of $\leq$ 5 cm. Still there is almost two orders of magnitude falloff from the dominant length scale, and we are therefore able to capture most of the variance that is responsible for the majority of the energy dissipation. The dominant turbulent motions can clearly be seen in the data records, which show periodic large variations on timescales of 30–60 seconds, corresponding to mixing lengths scales of 0.25–0.5 meters for a mean horizontal current of order 0.05 m/s (see Fig. 4.7 for some examples).

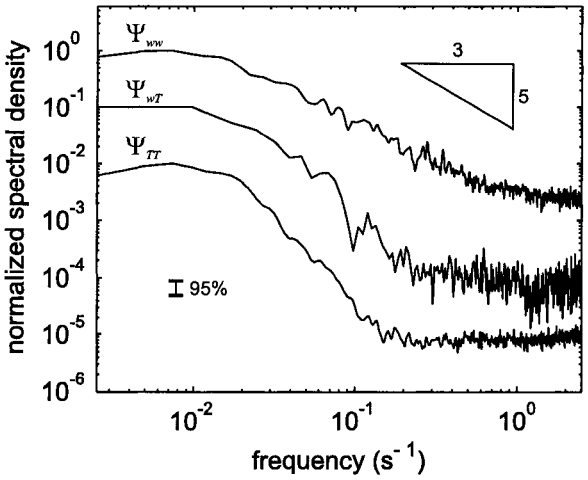

Figure 4.6: Normalized power spectra for one-hour time series of w', $w'T'$ and T', covering the time period shown in Figure 4.7a. The $w'T'$ and $T'T'$ spectra were offset one decade downward for clarity. The approximate 5-second thermal time constant for the thermistors is evident, but most energy is at larger wavelengths. Total variances are $\langle w'w' \rangle = 1.70 \times 10^{-4}$ m^2 s^{-2}, $\langle w'T' \rangle = 1.94 \times 10^{-4}$ m s^{-1} K and $\langle T'T' \rangle = 6.20 \times 10^{-3}$ K^2. The mean current speed, $\overline{u}$, is 0.038 m/s.

4.4 Turbulent heat flux

There are two limiting thermal convection regimes that our turbulence instruments could be experiencing; (1) forced convection or (2) free convection. In free, or natural, convection, the movement of the fluid is due entirely to density gradients within the fluid, e.g. hot air rises over cold air. There is no external device or phenomenon which causes fluid motion. In forced convection, the fluid is forced to flow by an external factor—wind in the atmosphere, geostrophic or tidal currents in the ocean. Our measurements, which were generally obtained directly above areas venting warm hydrothermal fluid, but were quite close to the bottom boundary in a known cross-flow, will be experiencing some mixture of these two modes of convection. In a homogenous, neutrally stratified boundary layer, the Monin-Obukhov length is the ratio of production of turbulent kinetic energy due to the mechanical shear and the magnitude of buoyancy conversion, and defines the height above the surface where buoyant factors

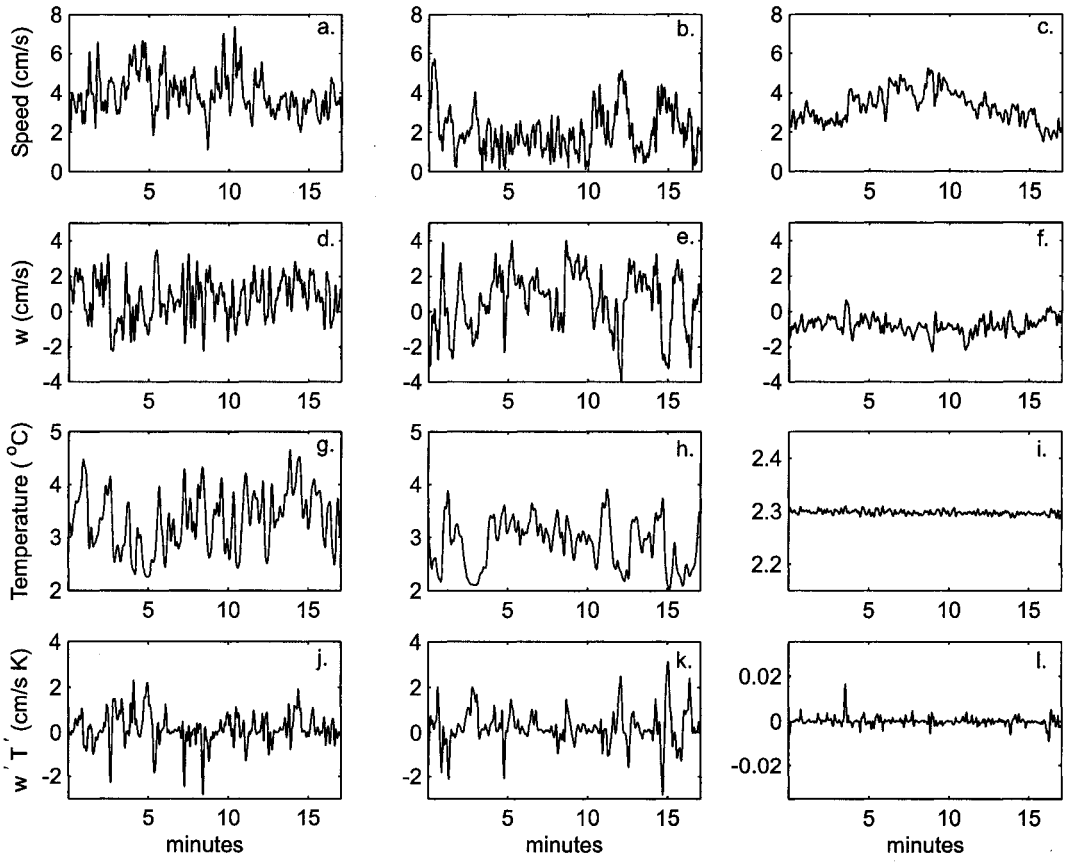

Figure 4.7: Samples of typical 17-min records. Columns 1 and 2 contain data from two MAVS placed approximately 4 meters apart during the 2002 field program in the Easter Island area within the Main Endeavour Field. Column 3 is from a MAVS placed in the central valley, approximately 250 meters east of this site during the same time interval. Most of the energy is at temporal scales of less than one minute [see (a)-(f)]. Mean turbulent heat fluxes over this interval are 5900, 8900 and 2 W/m^2 for (j), (k) and (l), respectively. Note the change of one and two orders of magnitude in the scales of panels (i) and (l) respectively.

begin to dominate over shear production of turbulence from the horizontal flow. The generation of turbulent kinetic energy due to shear production can be expressed as

$$S = \tau \frac{\partial \overline{u}}{\partial z}, \tag{4.9}$$

where $\tau = u_*^2$ is the kinematic Reynolds stress and $u_* = (\langle u'w' \rangle^2 + \langle v'w' \rangle^2)^{1/4}$ is the local friction velocity. For our calculations, we used 17-minute averaging periods in determination of local shear velocity. Numerous observations of the time-averaged velocity gradient and the Reynolds stress have established that

$$\frac{\partial \overline{u}}{\partial z} = \frac{u_*}{\lambda}, \tag{4.10}$$

where λ is the length scale of the dominant turbulent motion [102]. In a constant-stress, unstratified turbulent surface layer, $\lambda = \kappa|z|$, where κ is von Kármán's constant (taken to be 0.4) and z is the height above the surface. Using $\lambda = \kappa|z|$, the generation of turbulent kinetic energy due to shear production can be expressed as $u_*^3/\kappa|z|$.

The local rate of buoyancy conversion in the turbulent kinetic energy equation is

$$B = \langle w'b' \rangle = g\alpha \langle w'T' \rangle, \tag{4.11}$$

given that the buoyancy flux depends almost exclusively on the heat flux, i.e. the salinity flux is assumed negligible, for low-temperature diffuse vents. Thus we can estimate the Monin-Obukhov length from direct observations of u_* and $\langle w'T' \rangle$, or

$$L = -\frac{u_*^3}{\kappa g \alpha \langle w'T' \rangle} = -\frac{u_*^3 \rho_0 c_p}{\kappa g \alpha Q}. \tag{4.12}$$

Using the deployment average values given in Table 4.2, it can be shown the Monin-Obukhov length scale would be at all the deployment sites with heat flux greater than 1000 W/m^2, between -1.5 and -8.4 m (L is defined as negative for unstable conditions), although substantial variability exists on shorter timescales. At the 17-minute averaging timescale used for our calculations, it was not uncommon for both stable and unstable conditions to be sampled over the course of a multiday deployment, even near regions which exhibit rigorous venting.

The actual shape of the surface-layer velocity profile is influenced by the local state of stratification. Unstable conditions yield larger mixing length scales, while stable stratification yields dominant mixing scales which are smaller. Most of our observations above diffuse vents are within a statistically unstable boundary layer, where the fluid density is generally lower near the seafloor interface than it is above. The Monin-Obukhov similarity theory has been extended though the use of stability functions which depend solely on z/L or

$$\frac{\partial \overline{u}}{\partial z} = \frac{u_*}{\kappa |z|} \Phi_m, \tag{4.13}$$

where the Φ_m function were empirically determined from atmospheric data to be

$$\Phi_m = (1 - 16\frac{z}{L})^{-1/4}, \tag{4.14}$$

and

$$\Phi_m = (1 + 5\frac{z}{L}), \tag{4.15}$$

under unstable and stable conditions, respectively [103, 104]. Thus a Monin-Obukhov length scale of -1.5 meters would effectively increase the dominant mixing length from 0.2 to 0.33 m, although dominant mixing lengths of up to 0.45 m are not uncommon for shorter averaging timescales. Alternatively, it has been postulated that the mixing length may be proportional to the wavelength at the peak in the weighted vertical velocity spectrum, or $\lambda_{peak} = c_\lambda / k_{max}$, where $c_\lambda = 0.85$ [105]. Examples of the 1-hour average spectra are shown in Figure 4.8 and give reasonably good correspondence between the two methods, with λ_{peak} ranging from 0.1 to 0.5 m, but typically a value close to 0.2 to 0.35 m would be estimated.

The dissipation rate can also be calculated directly from the measured wave number velocity autospectra within the inertial subrange,

$$\varepsilon^{2/3} = \frac{3}{4\varphi} \Psi_{ww}(k) k^{5/3}, \tag{4.16}$$

where Ψ_{ww} is the vertical velocity energy density spectra at wavenumber $k = 2\pi f / \overline{u}$ in the inertial subrange of the spectrum and φ is Kolmogorov's constant, taken to

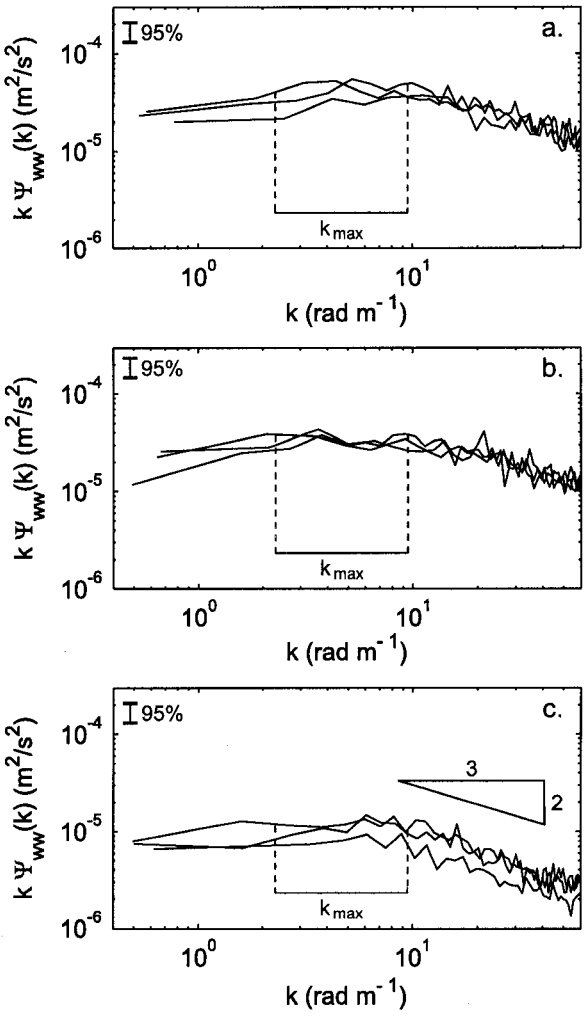

Figure 4.8: Examples of smoothed 1-hour spectra, corresponding to the instruments shown in Figure 4.7a, b, and c, plotted versus the wave number, $k = 2\pi f/\overline{u}$, where $\overline{u}$ ranges from 2.8 to 4.4 cm/s for the deployment intervals shown above. Dashed lines mark the spectral peak, $k_{max} = c_\lambda/\lambda_{peak}$. Dissipation rate may be estimated at any point within the -2/3 slope region.

be 0.51 [106, 107]. In Figure 4.9, the deployment averaged mechanical shear production and the calculated buoyancy conversion are compared to the dissipation rate, where time intervals which fail a frozen turbulence criteria are excluded. The deployment averaged buoyancy conversion is everywhere less than half the estimated shear production, and the shear production is equal to or greater than the dissipation rate. From this comparison, it seems plausible that the overall importance of diffusely venting patches to the structure of turbulence in the near-bottom boundary layer lies in its enhancement of mechanical stirring, rather than in direct plume entrainment.

Turbulent heat fluxes were directly calculated from our measured vertical velocities and temperatures,

$$Q = \rho c_p \langle w'T' \rangle, \tag{4.17}$$

where $\langle w'T' \rangle$ needs to be computed over timescales sufficiently long for statistical robustness, but sufficiently short to ensure the assumption of stationary. This time interval, chosen to be around 17 minutes, was easily obtained in our short-term deployments (which recorded continuously at either 2 or 5 Hz). But due to logistical constraints, the yearlong deployments only recorded bursts of measurements over a time interval of 90–160 seconds. These timescales are of similar order to the scale of the dominant turbulent motions. To test whether we could obtain statistically reliable heat flux estimates utilizing only short, 1.5 to 2.5 minute, bursts of recordings, we compared the short-term, continuously recording deployments to results obtained from decimating these records to simulate the long-term sampling. The measured turbulent heat fluxes seem to indicate that the shorter sampling periods can substantially underestimate the turbulent heat flux, when short time averages are considered. But generally when averaged over multi-day deployments, the results were more comparable. We thus expect the turbulent heat fluxes estimated from the long-term deployments to be lower-bound estimates, but correct to order of magnitude.

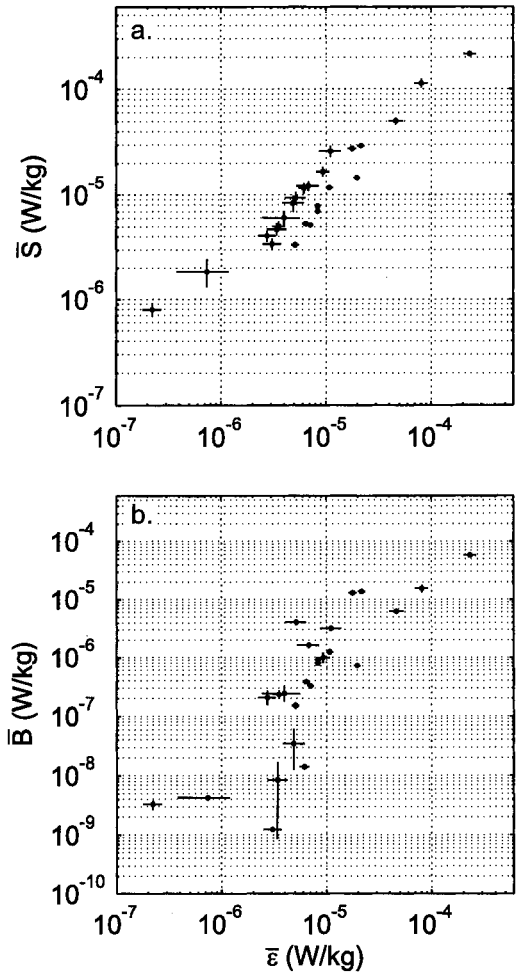

Figure 4.9: (a) Comparison of estimated shear production, $S = \frac{u_*^3}{\kappa|z|}\Phi_m$, to the dissipation rate, ε, for the deployment averages. (b) The dissipation rate generally increases with the local buoyancy conversion, $B = g\alpha\langle w'T'\rangle$. Turbulent heat flux relates to the buoyancy conversion by a factor of $(\rho c_p)/(g\alpha)$, which is a function of fluid temperature, but is approximately 3×10^9 kg/m^2. Ninety-five percent bootstrap confidence limits are shown for each estimate as a representation of the uncertainty.

4.5 *Discussion*

Comparison of the measured temperatures at the rock/water interface with the measured turbulent heat flux has shown that point measurements of surface interface temperature are a poor predictor of turbulent heat flux measured above the diffuse vent. This result is perhaps not completely surprising given the large spatial gradients in surface rock temperature shown in Figure 4.2 and Table 4.1. Nevertheless this result could also be a consequence of spatially variable permeability modifying the velocity of the effluent fluid, and thereby affecting the transport and discharge rate of hydrothermal fluid out of the seafloor, or surface roughness variability which may locally enhance or reduce the measured heat flux over the vent site. However, since our six year-long records did not show a strong correlation between the bottom thermistor and observed turbulent heat flux (examples are shown in Figure 4.10), it is most plausible that the bottom thermistor measures only the temperature of very localized effluent fluid, and that this temperature may vary over small spatial distances. Even so, both the turbulent heat and the bottom thermistor temperatures did display variability on monthly to annual timescales. This variability may be indicative of slow variations in the permeability of the uppermost rock matrix due to mineral precipitation or dissolution or sub-seafloor biological productivity. However, without synchronous volume flux and fluid density measurements, it is impossible to distinguish between changes in the geologic properties of the sub-surface flow paths and the rate of heat supplied to the system [2].

Several qualitative observations can be made from the turbulent heat flux observations we have obtained over basalt-hosted, diffusely venting patches of the seafloor. The probability and cumulative distribution functions for each of the vent fields studied are shown in Figure 4.11. The large skewness of the probability distribution indicates the efficiency with which heat is dispersed as the bigger eddies overturn. Similarly, the large kurtosis reinforces the view that most of the actual heat trans-

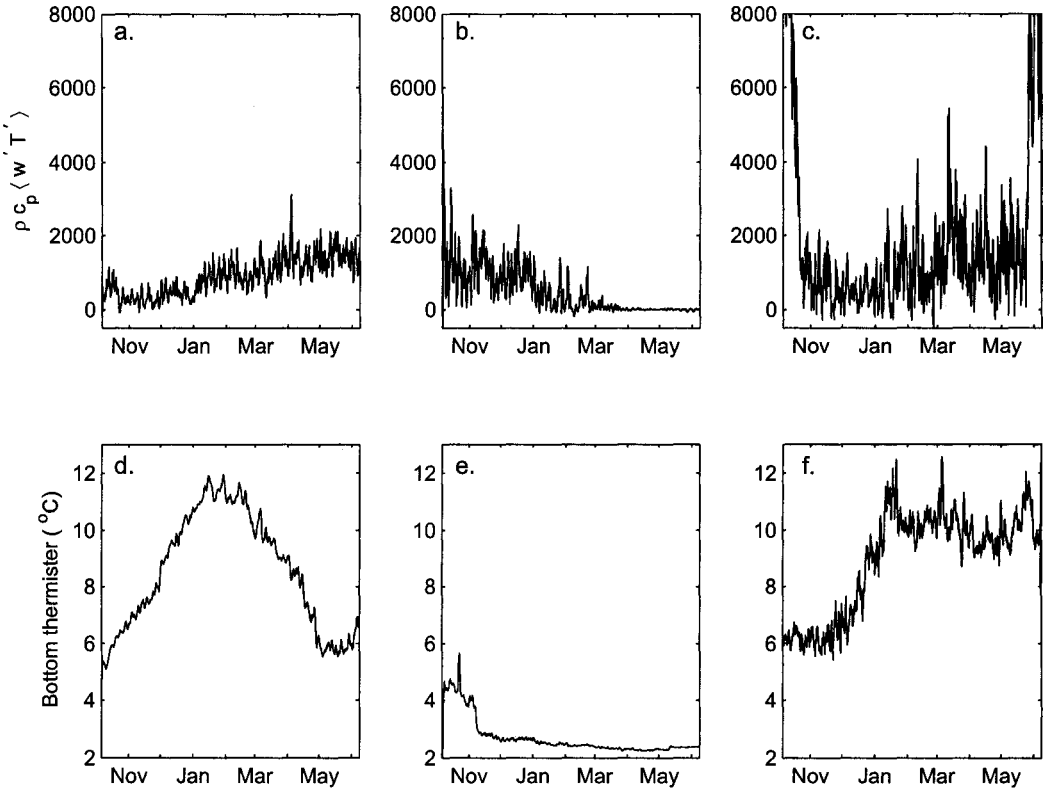

Figure 4.10: Examples of turbulent heat fluxes (in W/m^2) calculated for two instruments (a), (b) in the Clam Bed vent field and one (c) in the Easter Island vent area in Main Endeavour Field. The temperature recorded at each instrument base is shown in (d), (e) and (f), respectively. Instruments were deployed in 2000 and recovered in 2001. Data shown after a low-pass 36-h filter was applied for clarity. Large changes in temperature at the water / rock interface do not necessarily correspond to changes in the measured heat flux at 0.51 meters above the vent source.

fer takes place during intermittent events, and emphasizes the fact that there will be substantial variability in short-term averages of heat flux. The accuracy of such statistics depends strongly on the characteristics of the distributions, and if the tails of the distribution are poorly sampled, the mean values will likewise be poorly estimated. While the most common observed value of heat flux ranged from 50–730 W/m^2, the mean values were an order of magnitude larger. Functionally, the Clam Bed vent field results are very similar to the observations of diffuse heat flux at the Main Endeavour vent field, although the mean heat flux was roughly half of that observed within the Main Endeavour Field. These two sites represent the most comprehensively studied regions in our study. Clam Bed is mostly dominated by large areas of diffuse flow and has only three active sulfide structures. In contrast, Main Endeavour Field is dominated by large, focused-flow structures and has only small patches of basalt-hosted diffuse flow at any distance from the sulfide edifices. Yet for each vent field, only about 20% of the observations were above the calculated mean, and removal of the largest 5% of measured heat flux values reduces the mean by a factor of approximately one third. The consistency of the results most likely indicates some geologic control on the hydrothermal discharge, but human preferences for instrument placement on the seafloor cannot be totally excluded. Nonetheless, the range of turbulent heat fluxes observed and the measured temperatures of effluent hydrothermal fluid at the rock/water interface, indicate that diffuse flow may be preferentially located in regions of enhanced permeability, greater than 10^{-10} m^2 from Figure 4.3 and Table 4.2.

A recent water column study of the Main Endeavour Field [98] has attempted to quantify the lateral transport of warm hydrothermal fluid within the axial valley, while also quantifying the flux of heat in the buoyant plumes above the vent field. Estimates of 50–150 MW were obtained for the lateral near-bottom transport and 650 $\pm$150 MW for the high-temperature buoyant sources [70, 98]. Extrapolation of our turbulence measurements, assuming the heat flux measured at 0.5 m is representative

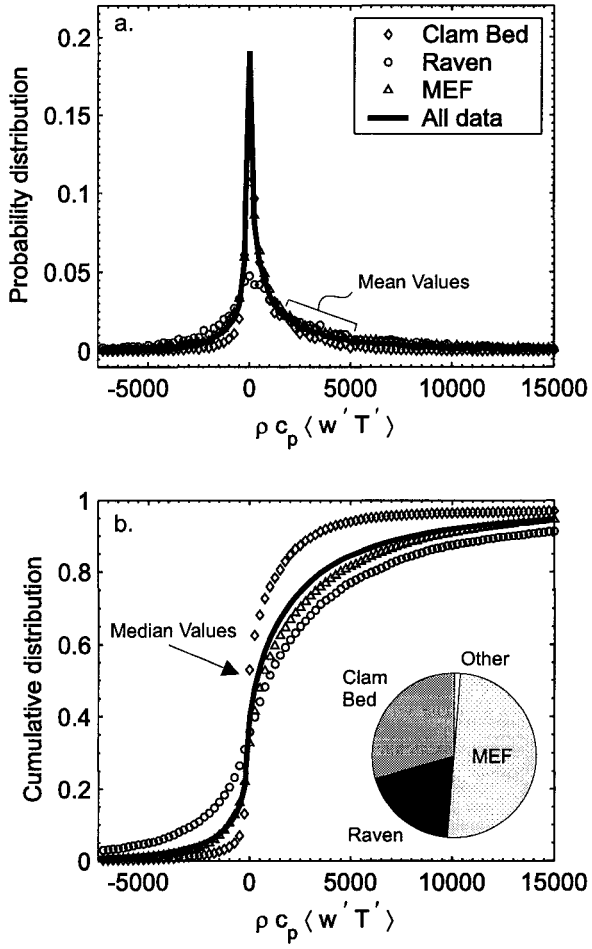

Figure 4.11: (a) Probability distribution of turbulent heat flux estimates obtained during the 2000, 2001 and 2002 field programs. Large skewness is due to the efficiency with which heat is dispersed by larger eddies. (b) The large kurtosis, or peakedness, indicates that most of the actual heat transfer takes place during intermittent events. The median values for these observations range between 50–730 W/m^2, while mean values are between 1800–5500 W/m^2. The inset pie chart shows the spatial distribution of the measured heat flux values; 50% Main Endeavour Field, 19% Raven, 29% Clam Bed and <2% in the central valley and High Rise vent field. Total number of observations over the three years was 36150 at twenty-five different locations, and the mean heat flux was 4100 W/m^2.

of the surface heat flux and that the region of diffusely venting seafloor is between 0.5–5%, yields 700 m × 300 m × 0.005 to 0.05 × 5500 W/m^2 or 6–58 MW, roughly consistent with the water column data. Similar scaling applied to the Clam Bed vent field, but using the smaller area of the vent field, a larger percentage of seafloor having diffuse venting (~20–30%) of the approximately 200 m × 300 m vent field, and a lower mean heat flux of 1800 W/m^2 gives a similar range of heat flux between 21–32 MW. This result is of comparable magnitude to, but still substantially smaller than, an earlier study of the focused heat flux from this vent field of 122 ± 61 MW [62].

4.6 Summary

The flux of mass and energy through the seafloor interface impacts the interactions of the biological, chemical and physical processes important to the development of deep-sea hydrothermal vent communities, and also the global ocean chemical balance [29, 70, 80, 108, 109, 110, 111, 112]. In this paper, we have examined the processes important for the advective transfer of heat from the basaltic upper oceanic crust to the near-bottom boundary layer via basalt-hosted, diffusely venting regions of a mid-ocean spreading ridge. Our observations indicate that the seafloor interface is very heterogeneous within these regions of diffuse venting. This variability at the interface is however quickly homogenized both above and below the surface. The turbulent heat transfer in the near-bottom surface layer (< 2 m hob) is controlled by the mechanical production of shear due to bottom currents. However, substantial enhancement in the shear production was observed near sites exhibiting large surface heat fluxes. Plumes from the low-temperature diffuse sources are likely to be constrained within the bottom low-stability layer, and are not likely to be mixed into high-temperature neutrally-buoyant plume which is of order 100s of meters above the axial floor. While short-term observations of turbulent heat flux show large variability, a mean heat flux

between 2–5 kW/m^2 is probably reasonable for diffuse-patches in this study area. The measured heat fluxes imply permeabilities greater than 10^{-10} m^2 for the uppermost basaltic crust.

Chapter 5

TEMPORAL VARIABILITY

The influence of tides on submarine hydrothermal systems has been observed almost since the discovery of hot springs in the deep ocean over 25 years ago [33]. Ocean tides modulate the seafloor pressure field, and thereby force a periodic variation in hydrostatic pressure throughout the water column and in any portion of the upper oceanic crust which is in 'open' contact with the water column. These tides, which may yield an effective stress as much as two orders of magnitude larger than co-located Earth tides, also cause compression and dilation of the rock matrix within the upper oceanic lithosphere [54, 114]. This deformation may be a significant factor in the observed variability in fluid flow rates out of, and the microseismicity near, deep-sea hydrothermal systems [36, 53, 55, 114, 115, 116, 117]. But the presence of significant tidal currents in the bottom boundary layer have made it difficult to ascertain how much (if any) of the observed modulation of hydrothermal temperatures is due to (1) an actual modulation in the temperature of the effluent fluid or (2) the effect of boundary layer processes that advect heat down to, or along, the seafloor interface.

Tidal modulation of horizontal bottom currents has long been suspected of having a substantial effect on many of the deep-sea hydrothermal observations; particularly measurements of fluid temperature near diffuse hydrothermal vents and observations of the biologic responses of vent fauna [31, 32, 118]. Oscillations between peak- and slack-tidal velocities (on the order of 5 to 30 cm/s in ridge-crest environments) may substantially affect thermal boundary conditions near the seafloor [27]. At periods of peak tidal flow, strong bottom water motion may efficiently advect heat away from the seafloor. In contrast, periods of slack or diminished tidal flow may allow

a thermal boundary layer (order 10s of meters) to develop above low temperature diffuse vents. Further, the enhanced fluid temperatures in this region of the boundary layer may subsequently be horizontally advected along the seafloor with the mean current [23, 56], resulting in elevated temperature measurements 'downwind' of the vent source. Recent field studies have documented examples of this effect, where periodic changes in temperatures measured at diffusely venting sites are the result of lateral advection of warm / cool fluid from regions of more / less vigorous venting [30, 119].

It has also been suggested that near-bottom tidal currents may also be the source of temperature oscillations recorded at high temperature focused-vent locations, even when the temperature sensors are buried within the sulfide or anhydrite deposits [30, 35]. Lateral motion of water along the seafloor interface, with perhaps some bottom water penetrating into the interior of the permeable vent structures, would yield a vertical pressure gradient within the vent structure. In areas of large vertical temperature gradients, such as vent orifices where measurements are typically obtained, effluent temperatures could be impacted due to changes in the cooling rate of the upwelling hydrothermal fluid; either through enhanced mixing with seawater or greater conductive heat loss [35]. It has been suggested that temperature variations on the exterior of the vent structures could also affect the rate of conductive cooling of the upwelling hydrothermal fluid, and imprint a periodic variation on the vent fluid temperature [30]. While it is not obvious how to easily distinguish between these processes with field data, these hypotheses are testable with field observations. Effluent fluid temperatures affected by any of these processes should display a small (fixed) phase lag between the measured effluent temperature and the bottom current speed and/or direction. This phase lag should be small, and related to the time it takes hydrothermal fluid to flow through the vent structure.

An alternative hypothesis for producing a modulation of effluent fluid temperature in high-temperature hydrothermal systems is related to the large gradients in the

thermodynamic properties that exist near the two-phase boiling curve. Because of these large gradients, small changes in fluid pressure could greatly affect the transport and thermodynamic properties of upwelling hydrothermal fluids, potentially yielding variations that could be measured at the seafloor. The disproportionately large impact that small variations in pressure and / or temperature can have on the transport properties of hydrothermal fluid near the critical point has long been recognized in numerical simulations [120]. The local extrema in the gradients of the buoyancy and heat transport properties may also exert significant control on both the style and the temperature observed during surface venting of hydrothermal systems [121, 122, 123].

Motivated by these observations, an examination of the impact of ocean tides on the thermodynamic properties of hydrothermal fluid and how these processes produce fluid temperature variations at the seafloor is undertaken. Section 5.1 describes the governing equations for idealized one-dimensional hydrothermal flow utilized in these simulations. Section 5.2 illustrates the effect of small pressure perturbations on the thermodynamic properties of fluid at a fixed depth surface, such as the seafloor or the high-temperature reaction zone. Section 5.3 examines the chronology of a hydrothermal fluid parcel as it travels through an entire idealized flow path, from reaction zone to seafloor. The expected temperature modulation of the effluent fluid is then calculated for two simplified models for the cooling of the hydrothermal fluid, i.e. conduction and mixing with seawater. In Section 5.4, the idealized model simulations are compared with field observations acquired at high-temperature focused vents on Axial Seamount. The simulations are able to match the amplitude of the effluent temperatures and also their observed phase-lags with respect to the ocean tide.

5.1 Model description

Seafloor hydrothermal systems are an important component in the Earth's total heat flux budget. It is estimated that roughly one third of the heat flux through the ocean

floor is due to hydrothermal circulation [1, 21]. Dissipating such a large amount of heat requires that a volume equivalent to the entire world's oceans be circulated through the ocean crust on the order of every 10^5–10^6 years [1, 111, 21, 124]. Chemical exchanges between the circulating water and seafloor basalts cause the effluent hydrothermal fluid to be either enriched or depleted in a number of chemical constituents—yielding a global impact on ocean chemistry [111, 112, 21]. Given the global importance and diversity in the processes of interest, a large collection of mathematical models have been developed to elucidate different aspects of hydrothermal systems. These models can in general be described as either cellular convection models or single-pass (pipe) models [125]. Cellular convection models solve the conservation equations (mass, momentum and energy) in a permeable 1-, 2-, or 3-dimensional rock matrix. Typically only the steady state solutions are derived. Single-pass models, in contrast, examine the general behavior of hydrothermal systems, without considering the details of the fluid temperature and velocity distribution. The equations used in pipe models are formulated only in terms of the integrated properties of the systems, such as total resistance to flow or total heat supply.

Whether pressure variations from the surface tide can yield variations in the effluent temperature of some deep-sea hydrothermal vents is examined with our model. Consistent with this goal, our model solves the governing equations for a compressible two-phase flow in one-dimension. It should be noted however that many of the idealizations utilized in this model are unlikely to represent the true complexity of deep-sea hydrothermal systems, such as assuming uniform permeability and porosity throughout the entire upflow zone or the absence of phase segregation in the upwelling fluid.

Governing equations for one-dimensional flow of pure water and/or steam and the transport of heat within the subsurface porous media are (1) the continuity equation, (2) the conservation of energy and (3) Darcy's law for fluid flow in a porous media

(see [87] for a complete derivation);

$$\frac{\partial \rho}{\partial t} + \frac{\partial}{\partial z} \cdot (\rho \overline{u}) = 0, \tag{5.1}$$

$$\rho \frac{Dh}{Dt} = \frac{DP}{Dt} + \nabla \cdot \lambda \nabla T + q_w, \tag{5.2}$$

$$\overline{u} = -\frac{k}{\mu} \left(\frac{\partial P}{\partial z} - \rho g \right), \tag{5.3}$$

where $\frac{D}{Dt} = \frac{\partial}{\partial t} + \overline{u} \cdot \frac{\partial}{\partial z}$ is the substantial derivative in one dimension. In the above equations, ρ is the fluid density, $\overline{u}$ is the vertical component of the Darcy velocity, h is the enthalpy (per unit mass), P is the pressure, λ is the thermal conductivity, T is the temperature, q_w is the transient heat transfer term, k is the permeability of the rock matrix, g is the acceleration due to gravity, and μ is the dynamic viscosity. These equations were solved using the equation of state for pure water [126]. Flow is assumed compressible, and the rock and fluid are not required to be in thermal equilibrium (i.e. a non-steady state solution). Assumptions implicit in these equations are that Darcy's Law for porous flow is valid, capillary-pressure effects and heat transfer by dispersion are negligible, and separation (e.g. gravitational segregation) of the two fluid-phases does not occur. Mass and energy balances for each time-step determine convergence.

5.1.1 Reaction Zone

As seawater-derived fluids penetrate oceanic crust in the axial region, their composition must continually evolve until the fluids enter a high-temperature reaction zone and obtain their end-member fluid compositions [127, 128]. Fluids within the reaction zone undergo dramatic changes in their thermodynamic properties, including energy content, transport efficiency properties, and composition [122, 129, 130]. A fixed (or at least slowly varying) amount of heat is input into the bottom of the reaction zone from a magmatic-derived heat supply. This heat is transferred through a thin conductive boundary layer to the hydrothermal fluid, which then rapidly migrates

away from the reaction zone and efficiently removes the input heat supply through vertical advection to the seafloor interface [122]. In our model, we are only concerned with describing the fluid's thermodynamic and transport properties as it leaves the reaction zone and migrates vertically up through the crustal section.

Theoretical studies suggest that the temperature at which plumes initially separate from the reaction zone may be controlled by gradients in the thermodynamic transport properties of the fluid [122]. From the steady-state solution of equation (5.2), it can be shown that the rate of change of energy per unit volume is given by the negative divergence of the total heat flux, or $-\nabla \cdot (\rho h\overline{u} - \lambda \nabla T)$. The first and seconde terms of this equation represent the rates of accumulation of energy per unit volume due to advection and conduction, respectively. *Jupp and Schultz* [123] noted that the relative importance of these two mechanisms can be expressed by the ratio,

$$Ra_L(z,t) = \left| \frac{\nabla \cdot (\rho h\overline{u})}{\lambda \nabla^2 T} \right|. \tag{5.4}$$

This ratio measures the influence of fluid motion on the evolution of the local temperature field and therefore *Jupp and Schultz* [123] described it as a 'local' Rayleigh number. If $Ra_L \ll 1$, conduction dominates over advection. Conversely where $Ra_L \gg 1$, advection dominates over conduction. *Jupp and Schultz* [123] argue that the temperature of the rising plume that initially separates from the conductive boundary layer above a heat source can be inferred by calculating where Ra_L is a maximum value. When heat transport through the boundary layer is purely conductive (i.e. prior to plume initiation), this corresponds to the region where the gradient in fluxibility as a function of temperature is maximized, where fluxibility is defined as $F = kg(h\rho(\frac{(\rho-\rho_0)}{\mu})$ [122]. Numerical simulations show for pressures appropriate for deep sea hydrothermal reaction zones that plumes do initiate near the maximum values of Ra_L, between $375 - 475°C$ for heat sources greater than 500°C [123].

During the time period following plume formation however, the rate of advective heat loss from the reaction zone must eventually equal (or at least not be greater

than) the rate of conductive heat gain, or the depth of the reaction zone must propagate vertically with respect to time. If the vertical migration of the reaction zone is constrained on daily timescales, yet small perturbations in the pressure field are permitted (e.g. the tides), then the advective heat transfer must be invariant with respect to these small pressure perturbations since the conductive heat equation is not dependent on pressure. Thus, for a given temperature, the solution in one-dimension requires that $\frac{\partial}{\partial P} \cdot (\rho h \overline{u}) = 0$, or equivalently $\frac{\partial F}{\partial P} = 0$ for the fluid that advects vertically away from the reaction zone. The temperature of the fluid leaving the reaction zone (and therefore the thermodynamic and transport properties) can thus be precisely specified for any given reaction zone depth (Figure 5.1). This temperature is always higher than the temperature where the Ra_L is maximized, which agrees with the line of reasoning that if the $Ra_L > 1$ the reaction zone would propagate towards the heat source. The exactness of this result is a consequence of the one-dimensional solution space however, and is not a general solution applicable to multi-dimensional problems.

5.1.2 Upflow Zone

Any changes in the thermodynamic properties of the hydrothermal fluid as it leaves the reaction zone are then mitigated during the time spent within the upflow zone. In these simulations, the permeability and porosity of the media are kept constant throughout the entire flow path, and viscous dissipation losses are neglected. Much of the solution space lies below the critical point for pure water (373.9 °C and 22.04 MPa) and the modeled hydrothermal fluid therefore consists of only a single phase. In our simulations, solutions that occur within the two-phase region would still be assumed to be single component. That is segregation between the vapor and water phases is not permitted. While this assumption does not account for geochemical measurements which indicate that phase separation occurs in some deep-sea hydrothermal systems [41, 60], it does allow the present model to demonstrate a potential thermo-

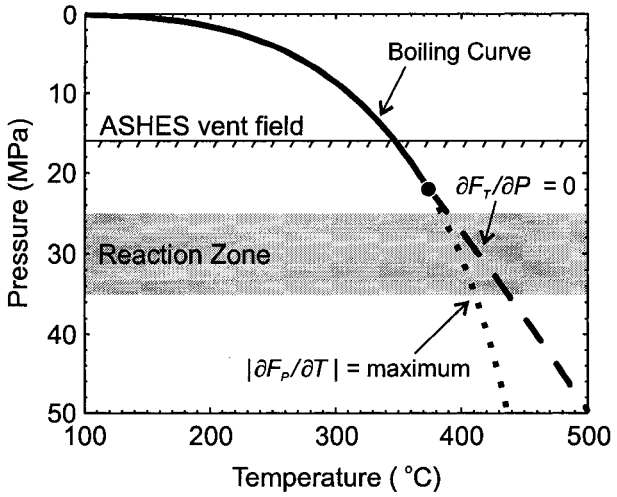

Figure 5.1: The temperatures for which plumes within the crust would (theoretically) initially separate from the boundary layer (dotted line; [123]) and for which the advected heat flux is not sensitive to small pressure perturbations (dashed line). The boiling curve for pure water (solid line) is also shown. The filled circle is the critical point for pure water. Geochemical data indicates that in ASHES vent field, the fluid has undergone subsurface phase separation [41]. If no near-surface cooling occurs, the fluid would vent at the boiling temperature. The depth range shown for the high-temperature reaction zone is consistent with a recent seismic study on Axial Seamount [45].

dynamic explanation for the modulation of hydrothermal temperatures — without the complexities produced by phase isolation. Observational data used to test our model in Section 5.4 is perhaps an extreme example of phase segregation within a vent field. Spatial variation in the salinity of the effluent fluid across the field, and between high temperature focused-vents and low temperature diffuse-vents, make a strong case for subsurface phase segregation. Hypotheses regarding the mechanism for the physical separation of brine and vapor phases range from gravitational segregation and fracture geometry [41, 131] to variations in the effective multi-dimensional permeability structure as a function of the vapor saturation [42]. In Section 5.4, both vapor- and brine-dominated venting fluids are compared with model simulations.

Permeability Model

While most model calculations can be performed without direct description of a porosity and permeability structure, a specific permeability model is used in order to examine the fluid's transient heat loss to the host rock during upflow. Our idealized model for the permeability and porosity structure is a cubic matrix of circular tubes [52]. The matrix has two inherent dimensions; the diameter, δ, of the individual tubes and the distance, b, between the tubes. Given this geometry, the effective porosity of the matrix is given by

$$\phi = \frac{3\pi}{4}\frac{\delta^2}{b^2}. \tag{5.5}$$

The actual (or intrinsic) porosity of the medium, which has been measured in ocean bottom gravity surveys [43, 8], may be substantially larger than the porosity that is relevant to flow models. Specifically, all voids may not be interconnected in a way which contributes to vertical flow. The volumetric surface area of this model is

$$A_0 = 3\pi\frac{\delta}{b^2}, \tag{5.6}$$

where $A_0 = A_{sf}/V$ is the surface area of fluid in contact with the rock per unit volume, A_{sf} is the interfacial area between the solid and fluid phases and V is a unit volume. Assuming flow through the tubes is laminar and occurs only in the vertical direction, the relation between the interstitial pore velocity, u_p, and the Darcy velocity is given by

$$\overline{u} = \frac{\phi u_p}{3}. \tag{5.7}$$

The intrinsic permeability of this model can then be directly computed as

$$k = \frac{\pi}{128}\frac{\delta^4}{b^2}. \tag{5.8}$$

For situations where two fluid phases are present (both liquid and vapor), the effective permeability would in all cases be less than the intrinsic permeability of the reservoir rock [132]. The reduction in effective permeability available to each of the separate

phases is also different. For low vapor saturations, the vapor phase can be nearly immobile; while at high vapor saturations, the brine / fluid phase becomes nearly immobile [42]. Determination of relative permeability functions is dependent on the flow geometry and fracture patterns and configurations [133, 134]. In our model however, the fluid and vapor phases are defined to have the same velocity and thus no relative permeability functions or corrections are sensible. If non-homogenous flow were considered, the heat transfer coefficients between the two fluid phases would also need to be estimated and some description of how the fluid and vapor phases adhere to the rock matrix and / or coalesce in the pore channels at different vapor saturations would be required.

Heat Loss

Since the time-varying temperature of hydrothermal fluid as it exits the seafloor is being examined, we are necessarily concerned with how the internal heat carried by the fluid is modified under the assumption that the fluid and the solid matrix are not in local thermal equilibrium. It is expected that harmonic temperature changes of the upwelling fluid will slowly diffuse into the host rock. During periods of cooler upwelling fluid, the hydrothermal fluid would be warmed by the rock matrix. Conversely, during time intervals of warmer upwelling fluid, the host rock would cool the upwelling fluid. In general, conduction of heat between host rock and fluid dampens any thermal variations carried by the upwelling fluid. The rate of heat transfer is dependent on the solid-fluid contact properties and the magnitude of the temperature gradient between the two phases. This type of heat conduction problem has been examined for a wide range of different flow geometries and fluid flow rates [135].

Simple one-dimensional Darcean flow and heat transfer models, similar to the one employed here, have been found to match experimental results to $\pm 20\%$ [136]. In these models, heat flux to the wall is conveniently expressed using a heat transfer

coefficient, h_{sf}, between the wall and the excess fluid temperature

$$q_w = h_{sf} A_0 (\langle T_c \rangle - \langle T_f \rangle), \tag{5.9}$$

where $\langle\ \rangle$ represents the volume average and T_c and T_f are the temperatures of the rock and fluid, respectively. Assuming laminar flow and using our permeability model, the heat transfer coefficient can be written as

$$h_{sf} = \frac{48\lambda}{11\delta}. \tag{5.10}$$

Combining equations (5.2) and (5.9) and ignoring axial conduction, the one-dimensional time-dependent heat conduction equation for the fluid [137] can be written as

$$\frac{D\langle T_f \rangle}{Dt} = \frac{h_{sf} A_0}{\phi \rho c_p} (\langle T_c \rangle - \langle T_f \rangle), \tag{5.11}$$

where c_p is the fluid's specific heat capacity, $c_p = (\partial h / \partial T)_P$. If we define the rate of heat transfer as $\Gamma = \frac{h_{sf} A_0}{\phi \rho c_p}$, then we can define a heat transfer coefficient, $\Gamma(k/\phi)$, which isolates the effects of porosity and density for our permeability model. This formulation allows easy comparison of the thermal dissipation rates for a variety of different intrinsic permeabilities and effective porosities.

While enthalpy is a monotonic increasing function of temperature at all pressures, variations in the heat storage capacity of a given mass of fluid leads to a local minimum in the rate of thermal dissipation for all pressures (Figure 5.2a). At subcritical pressures however, there exists a discontinuity in specific enthalpy associated with crossing the two-phase curve. The magnitude of this step increase is equal to the latent heat of vaporization at that pressure. Thus two fluid parcels on the two-phase curve may have slightly different enthalpies and still be isothermal, since there is no change in the temperature of the fluid parcel until the quantity of heat added or subtracted is sufficient to change the phase of the fluid. At this temperature there would be no transient thermal dissipation, $\frac{D\langle T_f \rangle}{Dt} = 0$, since there would be no temperature gradient between the fluid and the host rock. For all other cases, propagation of a

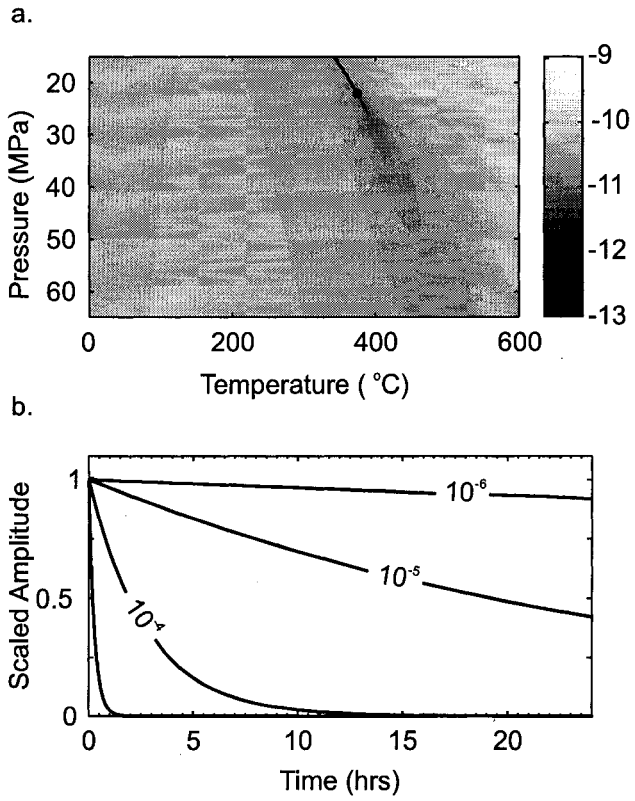

Figure 5.2: (a.) Plot of $\log_{10}(\Gamma(k/\phi))$ for the range of relevant temperatures and pressures. (b.) Dissipation rates for different Γ, ranging from 10^{-3} to 10^{-6} s^{-1}, illustrates that for thermal signals to propagate any distance requires high intrinsic permeability, low effective porosity (volumetric surface area) and close proximity to the two-phase curve.

thermal signal through the porous matrix on the order of days requires Γ to be of order 10^{-5} s^{-1} (Figure 5.2b).

In detailed calculations of transient heat transfer, one should also consider the rate of temperature change of the solid. However, given the substantial thermal capacity of the host rock in relation to the fluid, the temperature of the rock matrix is assumed constant with respect to time. The surface temperature of the host rock can then be prescribed to be the mean temperature of the upwelling hydrothermal fluid at any given vertical location. This assumption increases the magnitude of the total

dispersive loss of the transient temperature signal during upwelling.

Poroelasticity

While our model examines the effect of pressure variations on hydrothermal fluid flow at the reaction zone and within the upwelling branch of the hydrothermal circulation cell, the diffusive effect of poroelasticity on upwelling fluid flow rates within the upper oceanic crust is not included in the present model. Our model utilizes only the instantaneous component of the pressure signal (assuming a loading effiency of 0.6 [53]), but for simplicity neglects any impact of the diffusive pressure pulse within the porous upper oceanic crust. While the influence of tidally-induced pore pressure variations may be significant [53, 55], the proportional effect of the incremental velocity due to poroelastic effects decreases as a function of increasing thermal buoyancy-driven vertical velocity [53, 138]. The influence of poroelastic effects on modulating hydrothermal effluent may however be important in specific cases, and the effect (if it obtains sufficient amplitude) should be observable in field data. Solution of the poroelastic equations for velocity at the seafloor interface shows that the incremental vertical velocity will lag the ocean tide by $90 - 135°$, and potentially could yield a small incremental temperature variation at the seafloor which would display an additional fixed lag for all tidal constituents [139]. Spatial variations in pore fluid pressure due to this mechanism may also drive horizontal flow within the porous media. This effect would be magnified near upwelling hydrothermal fluid because of the high thermal gradients, and the resulting variability in the properties of both the fluid and the rock matrix [138]. It is also possible that a variation in horizontal flow within the rock substrate could enhance mixing of cooler host rock fluid with the upwelling hydrothermal fluid, and thereby generate measurable variations in effluent temperature and chemistry.

5.2 *Effect of pressure perturbations on fluid temperature*

If we consider fluid flowing past a fixed depth, for example fluid flowing out of rock/water interface, a periodic pressure variation should yield a temperature modulation on the effluent fluid. In the simplest case of a stagnant water column (i.e. $\overline{u} = 0$), we can see from equation (5.1) that $\frac{\partial \rho}{\partial t} = 0$. Thus the stipulation of no-flow during compressive forcing requires the fluid to be incompressible. Given the generally small gradients in fluid density as a function of pressure, this assumption is reasonable for small pressure perturbations such as ocean tides. It is therefore possible to directly determine the enthalpy variations prescribed by a pressure perturbation, $\Delta h = \frac{\Delta P}{\rho}$. The change in enthalpy varies inversely with fluid density, and therefore the greatest variations in enthalpy are seen at high temperatures (Figure 5.3a). Variations in specific enthalpy of this magnitude correspond to only small changes in the fluid temperature (Figure 5.3b). However, since the enthalpy variation scales directly as a function of the pressure change, a doubling of the tidal amplitudes would double the enthalpy response. Even so, the resulting variations in calculated enthalpy cannot account for the $0.5 - 1.5$°C temperature variations in effluent hydrothermal fluid measured at ridge crest depths. Temperature variability of this magnitude (< 0.2°C) also does not yield a significant change in the chemical reactivity of the fluid [140], nor are these variations of sufficient magnitude to be within the resolution of typically deployed thermistors.

If we focus on fluid leaving the reaction zone however, we find that small pressure perturbations can yield substantial variations in enthalpy. The fluid departing from a reaction zone that is held at a fixed depth is subject to the constraint that $\frac{\partial}{\partial P} \cdot (\rho h \overline{u}) = 0$ over the pressure range of the tidal interval. Thus while equation (5.2) requires that fluid leaving the reaction zone cannot change in temperature (if the reaction zone is stationary), small pressure perturbations do produce variations in the other fluid properties. The effect on the specific enthalpy of the fluid for pressure

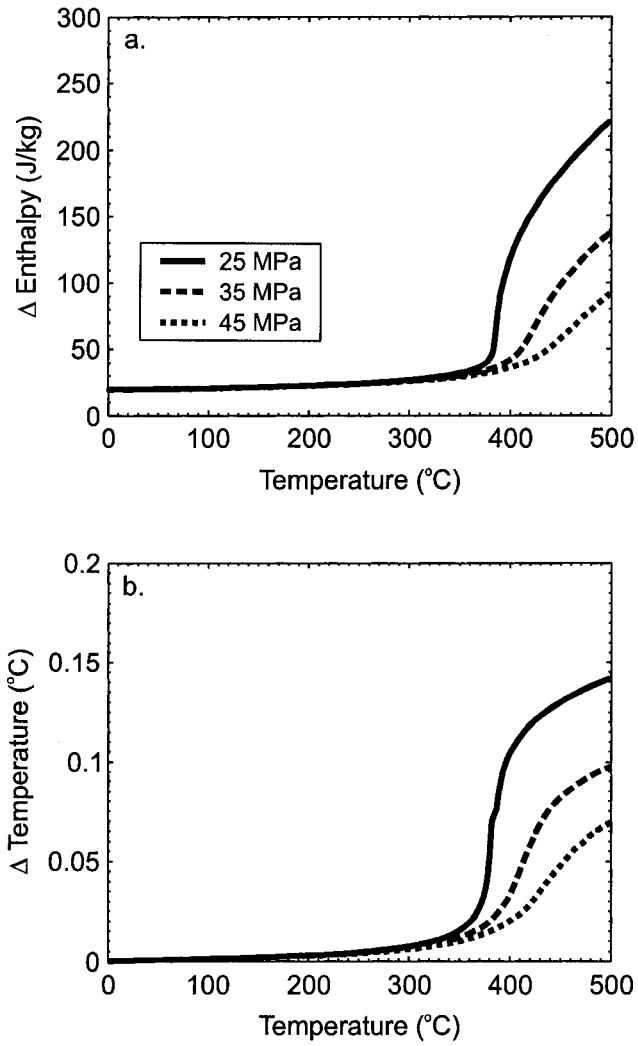

Figure 5.3: Small pressure perturbations (0.02 MPa in above examples) have little impact on the enthalpy or temperature of a parcel of non-convecting hydrothermal fluid. (a) Variation in enthalpy for an incompressible fluid, $\Delta h = \Delta P/\rho$. (b) The corresponding temperature variations for a non-convecting fluid are all less than 0.2 °C. This indicates that the simple thermodynamic (excluding advection) effect of pressure variations due to tides is insufficient to yield the 0.5−1.5 °C temperature variations observed at deep-sea hydrothermal vents.

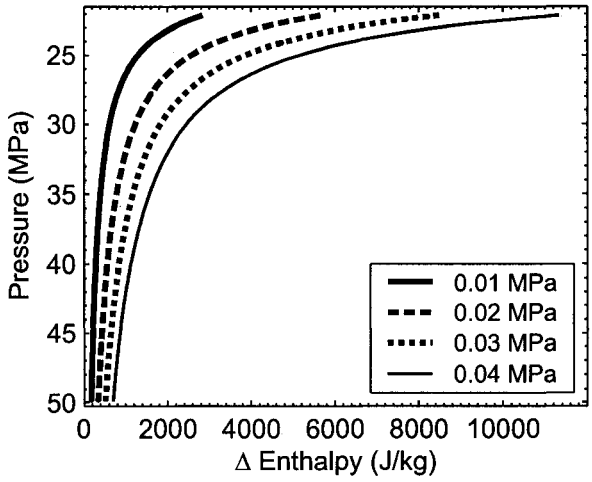

Figure 5.4: Plot showing the maximum change in enthalpy of the fluid leaving the reaction zone for different tidal amplitudes. Fluid leaving the reaction zone is subject to the constraint that $\frac{\partial}{\partial P} \cdot (\rho h \overline{u}) = 0$.

variations between 0.01 and 0.04 MPa is shown in Figure 5.4. Large gradients in the transport and thermodynamic properties produce a strong increase in the relative response as the critical point is approached. Although variations in fluid properties are considerably less than 1% of their absolute magnitudes, transport of this enhanced thermal energy to the seafloor interface can yield a measurable temperature response at hydrothermal vent orifices.

5.3 Flow path model results

For fluid within the upflow zone, we assume a uniform Darcian flow rate during ascent. The temperature of the upwelling fluid subject to this constraint is shown in Figure 5.5a for reaction zone depths equivalent to 25, 35 and 45 MPa. Although the specific enthalpy variations for fluid departing the reaction zone are substantially larger than those due to hydrostatic pressure variations alone, temperature variations in the hydrothermal fluid in the upflow zone are still small due to the large heat capacity of the fluid along the flow path (Figure 5.5b). For this same reason, the

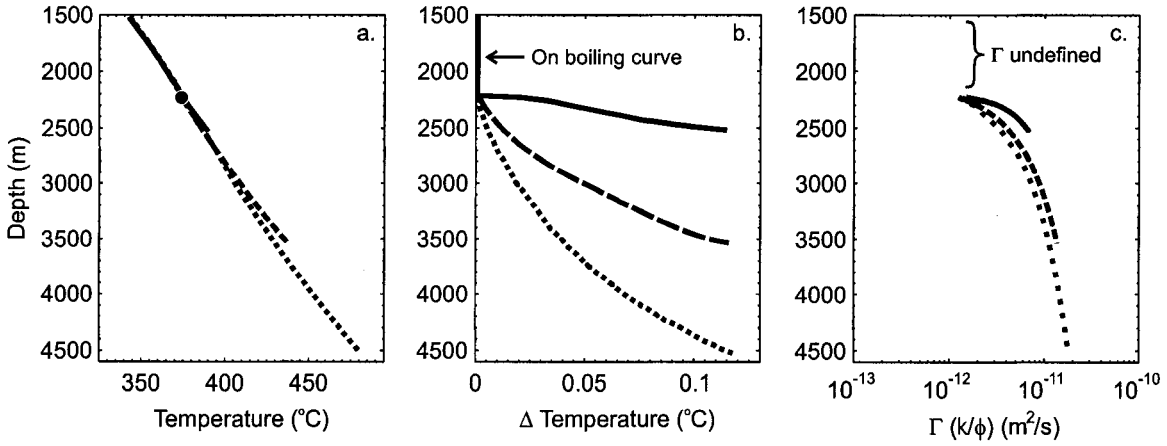

Figure 5.5: Ascent paths for three different reaction zone depths assuming the specific discharge, $\overline{u}$, is constant for the upwelling fluid. (a.) Temperature of the fluid in the upflow zone. The solid dot represents the critical point for pure water. (b.) Maximum temperature differential of the fluid passing a given depth for the three different reaction zone depths, assuming a 0.02 MPa tidal amplitude and negligible transfer of heat between the fluid and the host rock. (c.) Transient heat transfer coefficient along the ascent paths.

transient heat transfer rate to the host rock is also minimized in the region near the flow path (Figures 5.2a and 5.5c).

Even though the flow path is near the minimum in the heat transfer coefficient, strong constraints on the intrinsic permeability and effective porosity of the host rock are clearly required for the hydrothermal fluid to transport a transient thermal signal for a substantial distance prior to reaching the boiling curve. For example, a heat transfer rate of 10^{-5} s^{-1} with a mean heat transfer coefficient of 10^{-12} m^2/s requires k/ϕ to equal 10^{-7} m^2. This is equivalent to intrinsic permeabilities of 10^{-8}, 10^{-9} and 10^{-10} m^2 for effective porosities of 0.10, 0.01 and 0.001, respectively. These permeability values are higher than typically expected for oceanic crust, but are consistent with the range of permeabilities, 10^{-8} to 10^{-12} m^2, estimated from ophiolite studies [141, 142], previous modeling of ridge axis hydrothermal systems [143, 144, 145], recent borehole measurements [37, 146], and from the measured pore pressure

responses to ocean tides [53] and regional scale hydrologic pressure transients [49].

5.3.1 Near surface cooling

Once hydrothermal fluid approaches the seafloor interface, it will cool through conduction of the heat to the surrounding host rock (which may be rapidly cooled through secondary circulation), by mixing with a cooler background fluid, or through some combination of these two processes. For simplicity, only the two end-member cases are examined. In the pure conduction case, if transient heat transfer losses are negligible, or equivalently if the rate of conductive heat loss is very high near the seafloor interface, then variations in effluent temperature are determined from the entire variation in specific enthalpy. Since specific enthalpy increases with temperature over the full range of pressure, the corresponding change in temperature for a given enthalpy variation decreases with increasing temperature (Figure 5.6a). Gradients in specific enthalpy near the boiling curve force the temperature response to approach zero at the boiling point for the given pressure. While at the boiling point there is no change in temperature corresponding to small changes in enthalpy, since an increase in enthalpy equivalent to the latent heat of vaporization is required before the fluid can change temperature. For the case where all cooling is due to mixing with a background fluid (Figure 5.6b), a similar effect can be seen. In this case however, the temperature response also approaches zero when the majority of the fluid mixture consists of background fluid, which contains none of the variation in specific enthalpy. If the upwelling hydrothermal fluid mixes with cooler host rock water or conductively cools at any substantial depth however, it is clear from Figure 5.2 that any transient thermal signal would likely dissipate before the fluid reaches the seafloor interface.

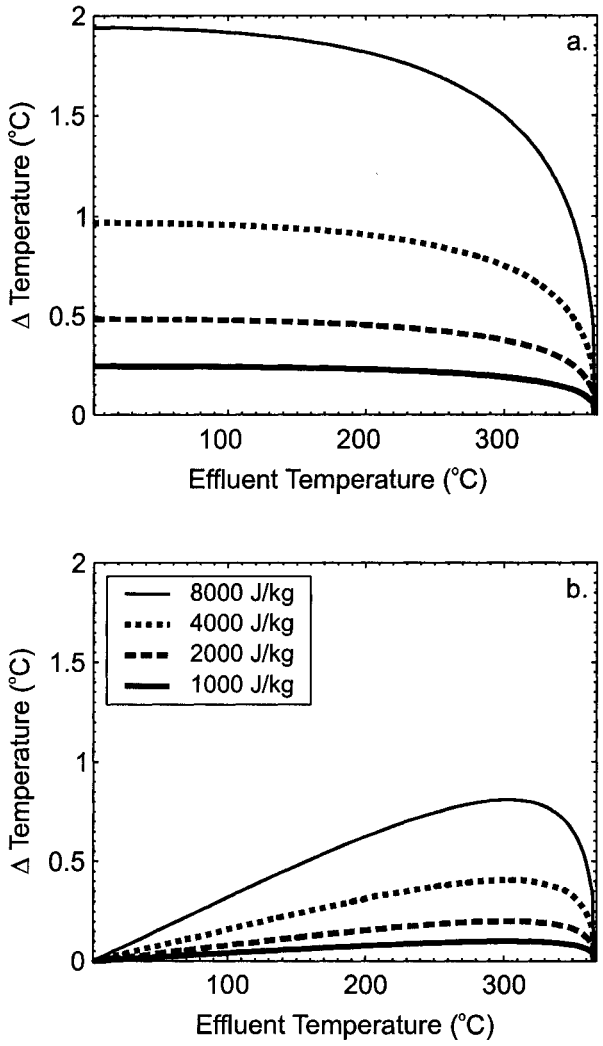

Figure 5.6: Temperature effect due to different enthalpy variations at 20 MPa. Due to the large heat capacity of fluid near the boiling curve, small variations in enthalpy yield only small temperature variations. (a) Temperature variations assuming rapid conductive cooling of the fluid, ignoring dissipative loss. (b) Temperature variations assuming cooling is due to mixing with 2°C water at 20 MPa.

5.4 *Model / data comparison*

No deep-sea hydrothermal system circulates the salinity-free water used in our model. However there is no other model for which thermodynamic properties and phase equilibria can be used reliably across all relevant environmental conditions, even for such thoroughly studied aqueous systems such as the sodium chloride solution [147, 148]. One important difference between the hydrothermal seawater system and the pure water system is the location of the critical point (e.g. from 373.9°C and 22.04 MPa for pure water to 405°C and 30 MPa for a 3.2% NaCl solution), and the slight displacement of the two-phase curve with depth [149]. The goal of this section is only to demonstrate a plausible thermodynamic reason for the tidal modulation of effluent temperatures and care should be taken when interpreting our simulation results, obtained by utilizing the equation of state for pure water, during any comparison with an actual hydrothermal system which has a more complex fluid chemistry.

Modulation of hydrothermal temperatures on tidal timescales has previously been reported on the Juan de Fuca Ridge at the Endeavour vent field [150, 151, 20] and at Axial Seamount [2], and also on the Mid-Atlantic Ridge at the TAG hydrothermal mound [32, 35]. Tidal modulation of hydrothermal temperatures is not a ubiquitous feature of deep-sea hydrothermal systems however [30, 152]. The field data utilized for the model comparisons was acquired from two high-temperature focused vents located in the ASHES vent field on Axial Seamount in the Northeast Pacific. Axial Seamount is a well-studied ridge axis volcano which has been repeatedly visited and sampled in recent years as part of a multi-year observatory effort (see http://www.pmel.noaa.gov/vents/nemo/index.html for additional information).

The two data records used for comparison with our model are from the Virgin Mound and the Inferno vent structures (Figure 5.7). The deployed thermistors took measurements every 20 minutes and their resolution was temperature dependent, ranging from 0.6−1.1°C. Inferno is a 4-m high sulfide structure venting brine-rich

fluid with effluent temperatures exceeding 320°C. Virgin Mound, while also venting fluid over 300°C, consists of a nearly pure anhydrite structure approximately 2-m across and is typically <1 m tall. The fluid compositions of the Virgin Mound and Inferno vents represent the two high-temperature endmember compositions that can explain most of the fluid compositions observed in the ASHES vent field, when a three-endmember (with seawater representing the third composition) conservative mixing model is employed [41]. The composition of Virgin mound fluid is gas-enriched and has low chlorinity, while the composition of Inferno fluid is comparatively gas-depleted and high-chlorinity. Fluid geochemistry argues that phase separation, and subsequent phase segregation, occurred below the seafloor. Virgin Mound is also somewhat depleted in calcium, indicating the hydrothermal fluid may have cooled in the sub-surface due to mixing with cold seawater and has precipitated anhydrite [41]. The boiling point for fluid similar to seawater composition (3.2% NaCl) is 348.9°C (or 344.6°C for pure water) at the pressures typical of the summit caldera on Axial Seamount [126, 149].

Of probable significance to the hydrogeology of this area is a volcanic eruption which occurred on the southeastern caldera wall in January of 1998, approximately 3 km distant from the ASHES vent field. This eruption modified both the effluent fluid chemistry and bacterial diversity within the vent field [84, 153, 154]. An active-source seismic survey in 1999 identified a region of partial melt at a depth of less than 1 km below the caldera floor, and micro-earthquakes recorded in the caldera region during this survey did not extend deeper than 2 km [45]. Thus it is likely that the high-temperature reaction zone is not deeper than 2 km below the caldera floor, and may be at a depth of less than 1 km during the time interval sampled.

5.4.1 Phase Information

An important consequence of any thermally modulated signal that originates at the reaction zone is that it will lag the seafloor pressure by an amount related to the time

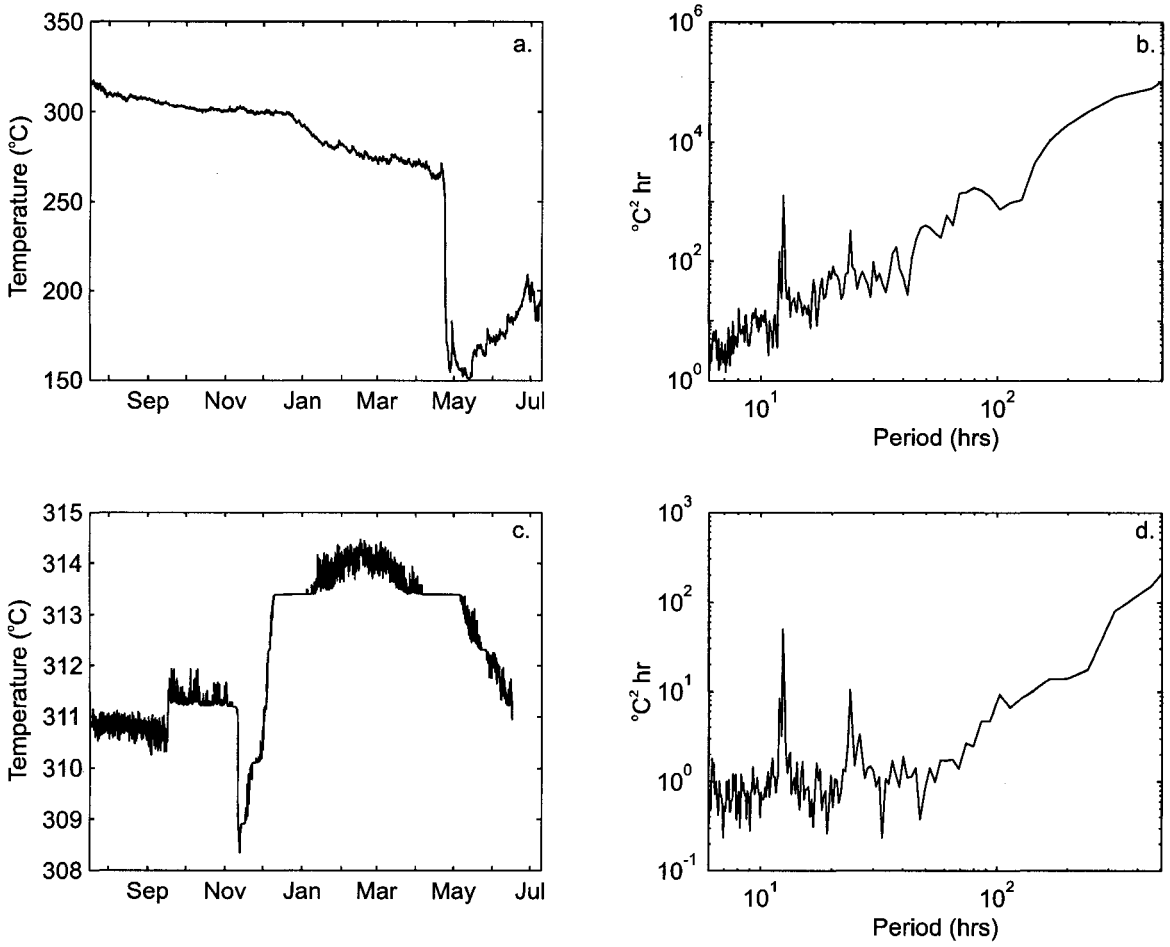

Figure 5.7: High-temperature data records collected at Axial Volcano in the NE Pacific from the summer of 1998 to the summer of 1999. (a.) Time-series and (b.) spectra of the effluent temperature from the Inferno vent show enhanced energy at tidal frequencies over the entire interval, including the post-April 1999 decrease in measured effluent temperature. (c.) Time-series and (d.) spectra of the effluent fluid from the Virgin Mound vent also show increased variance at tidal frequencies.

required for the thermal signal to propagate through the full extent of the upflow zone. This can be described as $\Delta t/\tau_i$, where Δt is the time the fluid spends in the upflow zone and τ_i is the period corresponding to the tidal constituents. The seafloor pressure field at Axial Seamount has been well characterized [155]. Additional bottom pressure data was obtained from the southeastern caldera wall for the year prior to the temperature data records, including 7 weeks of overlap in the two different types of data records [54]. The phase lags between the bottom pressure and the measured effluent temperature signals are shown in Table 5.1 for the six primary tidal constituents. Given (1) the range of periods for the tidal constituents, (2) noting that an increase in pressure yields a decrease in the specific enthalpy (energy per unit mass) for fluid leaving the reaction zone and (3) assuming the entire phase lag is due to the travel time of the fluid to the seafloor interface, a travel time in the upflow zone, Δt, can be estimated which is independent of geologic flow parameters. With these assumptions, both the Virgin Mound and Inferno vents have similar fluid upflow times of between 23 and 25 hours. Allowing for one-dimensional Darcy flow (i.e. equation (5.3)) and assuming the distance to the reaction zone is the same for both vents, the similar Δt indicates that the effective permeability in the upflow zone is remarkably similar (within 7%) for the fluid venting at both structures.

5.4.2 Temperature Amplitude

Given the tidal amplitude, an estimate of the maximum depth of the reaction zone can be determined by (1) examining the specific enthalpy variation for fluid departing the reaction zone at different depths and then (2) comparing this with the enthalpy variations required at the seafloor interface to yield measured temperature variability (see Figures 5.4 and 5.6). This calculation assumes no thermal dissipation, and represents the maximum possible depth to the reaction zone. In order to generate the amplitudes of the temperature variations observed at the seafloor (0.5−1.5°C), the reaction zone must be close to the critical point. For pure water this is at a depth

Table 5.1: Phase lags between the measured surface pressure and the effluent temperature signals, and from utilizing the given upflow times. The 95% confidence limits for the measured phase are given when less than ± 45°.

Constituent	Period (hrs)	Inferno	Model_I	Virgin Mound	Model_VM
S_2	12.0000	-160° ± 19°	-156°	153° ± 25°	153°
M_2	12.4207	-133° ± 12°	-132°	-178° ± 21°	178°
N_2	12.6584	-118° ± 22°	-120°	-173° ± 28°	-168°
K_1	23.9343	-140° ± 24°	-169°	163° ± 23°	165°
O_1	25.8198	-92°	-143°	-149° ± 37°	-167°
Q_1	26.8673	-113°	-131°	-151°	-154°
Upflow time (hrs)			23.2		24.9

equivalent to 22.04 MPa, and for a 3.2% NaCl solution it is at approximately 30 MPa. For our simulations, we have chosen the reaction zone to be at a depth of 22.3 MPa, or equivalently a depth of 690 m below the seafloor. Using this depth to the reaction zone and the travel times computed for the upflow zone, we find that the interstitial pore velocity for the upwelling fluid is approximately 8×10^{-3} m/s. From equations (5.3) and (5.7) we can write

$$\frac{k}{\phi} = \frac{u_p}{3} \frac{\mu}{g(\rho_0 - \rho)}. \tag{5.12}$$

Using this interstitial pore fluid velocity, 8×10^{-3} m/s, and the fluid properties calculated at 22.3 MPa with a reaction zone temperature of 376.6°C, we obtain $k/\phi \sim 10^{-11}$ m^2. For the idealized permeability model used in this study, this result yields effective permeabilities of 10^{-12}, 10^{-13} and 10^{-14} m^2 for porosities of 0.10, 0.01 and 0.001 respectively, or similarly Darcy velocities between 2.6×10^{-4} to 10^{-6} m/s. Increasing the reaction zone depth to 3000 m would increase the interstitial pore velocity to 1.8×10^{-2} m/s, and corresponding modify the other calculated values by

a factor of less than 3. The small value of k/ϕ implies very rapid dissipation of the transient thermal signal, unless k/ϕ is much larger (especially near the reaction zone) than the value determined from the entire upflow zone indicates and / or the fluid in the upflow zone (very) quickly meets and is maintained on the boiling curve during ascent.

In the model / data comparison in Figure 5.8, results have been shown where there is no thermal dissipation. If thermal dissipation were included, the reaction zone would need to be shallower. The model shown also assumes all the surface cooling is by conduction. Mixing with cold background water would decrease the model amplitudes by approximately 40% at these effluent temperatures. The reasonable fit between the model and observations is not surprising since the reaction zone depth was chosen to yield the appropriate measured amplitudes, and have constrained the flow in the upflow zone to yield the calculated phase lags. The time period shown was chosen since the Virgin Mound vent displayed significant temperature variability (of order 1°C) and *in situ* bottom pressure data was available [54]. The peak-to-peak variability in the measured temperature signal is interesting. However given that these amplitudes are close to the instrument resolution, it is uncertain whether this variability represents actual changes in the vent fluid properties or is an artifact of the instrument resolution and signal filtering.

5.5 Conclusions

A simple thermodynamic model which can explain the temperature modulation observed at some deep-sea hydrothermal vents has been described. The model is based on the assumption that for a stationary (non-propagating) reaction zone, the temperature leaving the reaction zone must be constant and the rate of advective heat transfer away from the reaction zone can not vary for small pressure variations. Correspondingly, this requires the heat content per unit mass of the fluid to vary over a

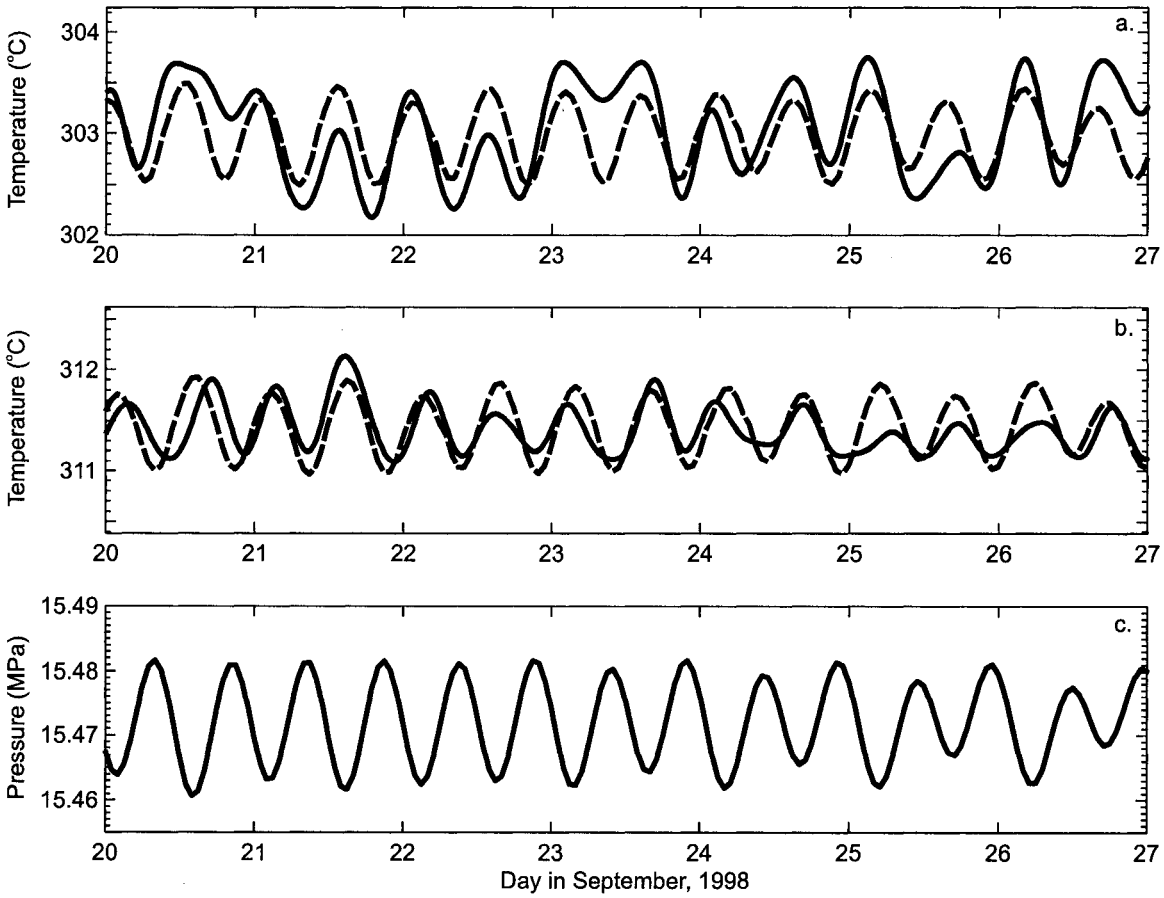

Figure 5.8: Model (dashed line) and measured (solid line) effluent temperatures for (a.) Inferno and (b.) Virgin Mound. (c.) Pressure data from a nearby bottom pressure recorder [54]. Effluent temperatures lag the pressure signal by the times given in Table 5.1. An increase in pressure yields a decrease in the enthalpy (energy per unit mass) for fluid leaving the reaction zone. All data records have had a 4-hr low pass filter applied.

tidal cycle or during other pressure perturbations. For the one-dimensional case, the temperature of fluid leaving the reaction zone can be precisely calculated.

Transport of the modulated thermal signal from reaction zone to seafloor is difficult to explain. Examination of a simple permeability model and a heuristic transient heat transfer model demonstrate that in order for a thermally modulated signal to propagate any distance through a rock matrix, several restrictions must be met. The rock matrix must have (1) a high intrinsic permeability and (2) a low effective porosity, and the fluid (3) must be close to the two-phase curve. Using values typical for oceanic crust it is found that, in general, it is unlikely that transient thermal signals will maintain significant amplitude for time periods greater than a few days. One notable exception occurs when the fluid is transported along the two-phase curve. In this case, different amounts of thermal energy per unit mass may be transported by fluid that is at the same temperature, due to the latent heat of vaporization. Since there is no variation in fluid temperature, there is no loss of transient thermal energy; similar in concept to a heat pipe. These stringent requirements are one possible explanation for the lack of tidally-modulated temperature variations at some hydrothermal vents.

Simulation results have been compared with field measurements obtained from two high-temperature focused vents on the summit of Axial Seamount in the Northeast Pacific. This data set may be considered somewhat prototypical for testing our thermodynamic model however, since there is a known high-temperature heat source (magma) at shallow depth. The hydrothermal fluid venting at this site has also undergone phase separation, and thus is likely to have been at least partially transported on the boiling curve. Consistent with the model, the measured phase lag between the seafloor pressure and the effluent temperature can be explained by simple transport of a thermal signal through the upper oceanic crust. Both Inferno and Virgin Mound vents indicate the time spent by the hydrothermal fluid in the upflow zone is approximately one day, and the temperature variations are consistent with the model which yields a decrease in thermal energy per unit mass for an increase in pressure. If the

thermal modulation of the effluent fluid occurs as the fluid leaves the reaction zone, then the modeled travel times indicate an interstitial pore velocity of between 0.8 and 1.8 cm/s for a reaction zone depth between 690 and 1500 meters below the seafloor. Comparison of the measured temperature modulation of the hydrothermal effluent with the thermodynamic model shows that the fluid leaving the reaction zone must be near the critical point. For a pure water system, that would imply a depth to the reaction zone of approximately 660 meters, or roughly 1500 meters in the case of a seawater system. The thermodynamic model proposed in this paper can thus provide a reasonable explanation of the modulated vent temperatures seen at Axial seamount. The model could be improved substantially however by inclusion of a more realistic fluid chemistry and thermodynamic properties, and with more realistic modeling of fluid transport in two phases. Model simulations for other vent fields where the depth of venting is below the critical point (e.g. TAG) or where the depth to the reaction zone is believed to be greater (e.g. Endeavour Segment) would be instructive.

Chapter 6

CONCLUSIONS (AND FUTURE WORK)

A large volume of low-temperature hydrothermal fluid is discharged into the deep ocean each year. Analysis of point-observations and measurements obtained within the deep sea bottom boundary layer yields information on the hydrologic and mechanical properties of the upper oceanic crust. Numerical simulation of one-dimensional porous flow from a theoretical high-temperature reaction zone within the igneous basaltic crust to the seafloor interface has indicated a thermodynamic explanation for some observations of tidally-modulated effluent signals from high-temperature hydrothermal vents.

6.1 Global-to-regional problems

Although the analysis included in Chapter 2 indicates that low-temperature hydrothermal flow is equivalent to about 20% of the total volume flux from river sources into the oceans [1], surprisingly little is known about its composition, properties or regional variability. This fluid has a significantly higher temperature and substantially different fluid chemistry than deep waters which it is injected into. Many research questions are still open. How this fluid is mixed into the deep ocean? Does this fluid get distributed over wide geographic regions, such as has been shown for high-temperature hydrothermal effluent [71]? Do biological process mediate, or make use of, the nutrients provided by diffuse hydrothermal venting? Are there regional hot-spots of low-temperature hydrothermal activity? Where? Why? What are the

controlling factors on the chemistry of low-temperature (on-axis and off-axis) fluids? What would the chemistry of the deep ocean be like if we turned off the tap of low-temperature hydrothermal venting into the deep ocean?

6.2 Co-registered flow and temperature

Pore fluid pressure in the oceanic crustal reservoir is sensitive to aquifer head, tectonic compression, loading / compaction with the absence of adequate drainage systems, intrusion of gas or fluid phase changes, and ocean bottom hydrostatic pressure (atmosphere + ocean). Fluid temperature within the reservoir is determined by mixing, advection and diffusion processes. Given that fluid temperature is believed to be the dominant factor controlling the density of off-axis crustal fluids (i.e. salinity variations in the crustal fluids are not large), these two state parameters are inextricably linked. In Chapter 3 co-registered flow and temperature data was examined. Studies of this type are yielding substantial advancements in our understanding about the plate-scale stress state, large-scale hydrology of the upper oceanic crust and the response of this fluid reservoir to both impulse and periodic forcing.

Variations in the sub-seafloor pressure field (in both time and space) drive horizontal and vertical flow within the crustal reservoir. In any permeable medium, pressure gradients drive a flux of interstitial fluid according to Darcy's Law, and thus require that changes in incremental pore pressure are subject to diffusion. This property was utilized in a recent study [53], where both the amplitude and phase information from borehole pressure sensors was utilized to estimate formation-scale hydraulic and mechanical properties of the upper oceanic crust. Relative amplification of the magnitude of lower frequency signals, and an incremental phase offset of the forcing and response functions are principal indicators of a poroelastic influence on the subseafloor hydrothermal circulation of crustal fluids, and observation of co-registered flow and temperature allow for direct testing of this hypothesis [2, 36, 139]. Pore

fluid pressure transients have also been examined in boreholes on the Juan de Fuca Ridge flank following a plate deformation event [49]. Hydrologic transients are characterized by a rapid co-seismic rise in pore pressure, followed by a continuing, slower rise to a peak, and then a much slower decay. Based on a simple model that the transients reflect a combination of coseismic elastic strain and subsequent hydraulic diffusion, [49] estimated bulk crustal properties, and also the size of the inferred (mostly aseismic) crustal extension event. Similarly, low-temperature on-axis hydrothermal systems showed large amplitude, periodic variations following this plate-scale strain event [48], although these variations are not currently well understood.

Year-long observations of temperature data from the monitoring probe placed on Baby Bare seamount also show large amplitude, periodic variations following a large seismic event (S. Lange, pers. comm.). Interestingly, the temperature signal shows significant variability at the four largest tidal constituents. Given the good correspondence of the tidal variance amplitudes to the local bottom pressure variance amplitudes, and also the large temperature variance—the upper part of the oceanic reservoir is predicted to have comparatively uniform temperature [156, 157]—implies local tidal *flushing* of the upper oceanic crust may be important, even in lightly sedimented regions of the seafloor.

Determination of static loading (e.g. crustal strain, aquifer head, and lateral pressure gradients) is only possible when changes in the flow regime—temperature, pressure—occur. Analysis of on-axis data from hydrothermal springs shown in Chapter 3 have shown that even in open-circulation systems, static overpressuring of the pore fluid of may be an important contributor to vertical flow [2]. These observations were only possible because of synchronous volumetric flow and temperature observations were collected over a multiple month time period. Analysis of on-axis data however is complicated by the associated high-temperature hydrothermal systems due to laterally induced flow [139], temporal variability in permeability due to mineral precipitation / dissolution or biological processes [88] fluid phase changes and

tidal variability in the energy transport of high-temperature fluids [3].

Utilizing the variability, it would be exciting to obtain the static stress state of the fluid and the bulk hydrologic and mechanical properties of the fluid reservoir (scale will be dependent on distance to recharge). This could be done by instrumenting both on- and off-axis fluid monitoring sites [2, 158]. Utilizing crustal strain events, one could additionally model the response and transient decay for plate-scale hydrologic and mechanical properties.

6.3 Boundary layer mixing and flow

The observation of turbulent heat flux above deep sea diffuse hydrothermal systems is ultimately determined by the geological transport properties of the upper oceanic crust. In Chapter 4 the interconnections of these two regimes was discussed. From the 36150 observations of the turbulent heat flux at roughly 0.5 m height above the bottom, it appears that diffuse flow is largely accomplished in regions of relatively high permeability ($>10^{-10}$ m^2) zones. This may be an important factor in the patchiness of diffuse flow on the seafloor, especially in locating the more rigorous regions of low-temperature diffuse flow. In general, it appears that most low-temperature diffuse venting will also be contained within the near-bottom mechanical boundary layer. Typical rise heights (without cross-flow) are approximately equal to the bottom low-stability layer observed in our survey.

However, even with these observations, very little is known about how this fluid is eventually mixed into the deep ocean. What role do tides, and tidal mixing, play? How is the boundary layer affected by the periodic, oscillating tidal flow? What is the effect of cross-axis versus along-axis flow? Is the axial valley, or the geographic location and distribution of venting, the dominant feature of the hydrodynamics of fluid flow along the Endeavour Segment? What is the along-axis distribution of diffuse venting? Are diffuse vents (quantitatively) located near faults and fissures, sheet or

pillow flow? What is the proportioning of diffuse and high-temperature flow along global spreading axes?

6.4 Temporal variability

Although each of the previous sections dealt with at least some aspect of temporal variability, Chapter 5 showed how analysis and simulation of temporal variability can yield important information on the hydrologic properties of the rock matrix in the region of upflow. Additionally, if the model proves robust, substantial information on the flow geometry, maximum fluid temperature, temperature in the reaction zone and during transport to the seafloor can be estimated. Substantial improvements to the modeling of fluid-rock interactions could then be undertaken with this flow history. In fact, fluid geochemistry provides one potential way to examine the robustness of the model, e.g. utilizing the Axial Seamount high-temperature systems, which have shown tidal variability for several years, and comparing the geochemistry with the models flow temperature and mixing history. An obvious first-order improvement to the model will be to incorporate the one-dimensional heat conduction equation. This will be required to better examine mixing and / or conductive cooling in future simulations. Examining other hydrothermal systems showing tidal variability will also test the utility of the proposed model.

6.5 Summary

In this dissertation, many aspects of the volume and energy flux of diffuse hydrothermal fluids have been examined. In Chapter 2, the global magnitude of low-temperature venting was examined. Chapter 3 went from this global-scale all the way down to observations obtained covering just one square meter of seafloor. These observations led to insights and provided context for the observations of heat flux obtained in the near-bottom boundary layer, discussed in Chapter 4. Finally, in chapter 5, the

tidal variability observed in the effluent temperature of a couple of high-temperature vents on Axial Seamount was addressed through the development of a thermodynamic model which can explain the modulation of hydrothermal fluid seen at some hydrothermal systems. However, this research has led to more questions. It is hoped that the theoretical and observation data presented in dissertation will provide the impetus and basis for many future research endeavors in deep sea hydrothermal research.

BIBLIOGRAPHY

[1] Johnson, H. P., and M. J. Pruis, 2003. Fluxes of fluid and heat from the oceanic crustal reservoir, *Earth and Planetary Science Letters,* 216, 565–574.

[2] Pruis, M. J. and H. P. Johnson, 2004. Tapping into the sub-seafloor: examining diffuse flow and temperature from an active seamount on the Juan de Fuca Ridge, *Earth Planetary Science Letters* 271 (3–4), 379–388.

[3] Pruis, M. J. and H. P. Johnson, 2004. Tidal modulation of hydrothermal effluent temperature, *Journal of Geophysical Research* submitted.

[4] Pruis, M. J., S. L. Hautala, H. P. Johnson, I. García Berdeal and T. Bjorklund, 2004. Turbulent heat flux in the deep ocean above diffuse hydrothermal vents, manuscript in preparation for *Deep-Sea Research.*

[5] Pollack, H. N., S. J. Hurter, and J. R. Johnson, Heat flow from the earth's interior: analysis of the global data set, *Reviews of Geophysics* 31, 267–280, 1993.

[6] Divens, D., Total sediment thickness of the world's oceans, National Oceanic and Atmospheric Administration, US Department of Commerce, Boulder, CO, 1996 [available on the Web at http://www.ngdc.noaa.gov/mmg/sedthick/sedthick.html].

[7] Mueller, R. D., W. R. Roest, J.-Y. Royer, L. M. Gahagan, and J. G. Sclater, A digital age map of the ocean floor, SIO Reference Series 93-30, Scripps Institution of Oceanography, 1997 [available on the Web at ftp.es.usyd.edu.eu/pub/agegrid].

[8] Pruis, M. J. and H. P. Johnson, 2002. Age dependent porosity of young upper oceanic crust: Insights from seafloor gravity studies of recent volcanic eruptions, *Geophysical Research Letters* 29 (5), 10.1029/2001GL013977.

[9] Stein, C. S. and S. Stein, A model for the global variation in oceanic depth and heat flow with lithospheric age, *Nature*, 359, 123–129, 1992.

[10] Stein, C. S. and S. Stein, Constraints on hydrothermal heat flux through the oceanic lithosphere from global heat flow, *Journal of Geophysical Research* 99, 3081–3095, 1994.

[11] Moran, J. E. and C. R. B. Lister, Heat flow across cascadia Basin near 47°N, 128°W, *Journal of Geophysical Research* 92, B11, 11416–11432, 1987.

[12] Davis, E. E., D. S. Chapman, K. Wang, H. Villinger, A. T. Fisher, S. W. Robinson, J. Grigel, D. Pribnow, J. Stein and K. Becker, Regional heat flow variations across the sedimented Juan de Fuca Ridge eastern flank: Constraints on lithospheric cooling and lateral heat transport, *Journal of Geophysical Research* 104, B8, 17675–17688, 1999.

[13] Embley, R. W., M. A. Hobart, R. N. Anderson and D. Abbott, Anomalous heat flow in the northwest Atlantic: A case for continued hydrothermal circulation in 80-M.Y. crust, *Journal of Geophysical Research* 88, B2, 1067–1074, 1983.

[14] Pribnow, D. F. C., M. Kinoshita and C. A. Stein, Thermal data collection and heat flow recalculations for ODP Legs 101-180, Institute for Joint Geoscienttific Research, GGA, Hannover, 0120432 [available on the Web at http://www.odp.tamu.edu/publications/heatflow/].

[15] Davis, E. E., K. Wang, J. He, D. S. Chapman, H. Villinger and A. Reseberger, An unequivocal case for high Nusslelt number hydrothermal convection in sediment-

buried igneous oceanic crust, *Earth and Planetary Science Letters* 146, 137–150, 1997.

[16] Wang, K., J. He and E. E. Davis, Influence of basement topography on hydrothermal circulation in sediment-buried oceanic crust, *Earth and Planetary Science Letters* 146, 151–164, 1997.

[17] Mantyla, A. W. and J. L. Reid, Abyssal characteristics of the World Ocean waters, *Deep-Sea Research* 30, 805–833, 1983.

[18] Mottl, M. J. and C. G. Wheat, Hydrothermal circulation through mid-ocean ridge flanks: fluxes of heat and magnesium, *Geochim. Cosmochim. Acta* 58, 2225–2237, 1994.

[19] Schlesinger, W. H., *Biogeochemistry: An analysis of global change*, Academic Press, San Diego, CA, 574 pp., 1997.

[20] Butterfield, D. A., W. E. Seyfried Jr. and M. D. Lilley, 2003. Composition and evolution of hydrothermal fluids, In: P. E. Halback, V. Tunnicliffe and J. R. Hein (Eds.), *Energy and Mass Transfer in Marine Hydrothermal Systems*, Dahlem University Press, Berlin, pp. 123–162.

[21] Elderfield, H. and A. Schultz, Mid-ocean ridge hydrothermal fluxes and the chemical composition of the ocean, *Annu. Rev. Earth Planet. Sci., 24,* 191–224, 1996.

[22] Wheat, C. G. and M. J. Mottl, Composition of pore and spring waters from Baby Bare: Global implications of geochemical fluxes from a ridge flank hydrothermal system, *Geochim. Cosmochim. Acta* 64, 629–642, 2000.

[23] Rona, P. A. and D. A. Trivett, Discrete and diffuse heat transfer at ASHES vent field, Axial Volcano, Juan de Fuca Ridge, *Earth Plan. Sci. Lett.* 109, 57–71, 1992.

[24] Baker, E. T., G. J. Massoth, S. L. Walker and R. W. Embley, A method for quantitatively estimating diffuse and discrete hydrothermal discharge, *Earth Planet. Sci. Lett.* 118, 235-249, 1993.

[25] Trivett, D. A. and A. J. Williams III, Effluent from diffuse hydrothermal venting 2. Measurement of plumes from diffuse hydrothermal vents at the southern Juan de Fuca Ridge, *J. Geophys. Res.* 99 (C9), 18417-18432, 1994.

[26] Lavelle, J. W., M. A. Wetzler, E. T. Baker, and R. W. Embley, Prospecting for hydrothermal vents using moored current and temperature data: Axial Volcano on the Juan de Fuca Ridge, northeast Pacific, *J. Phys. Oceanogr.* 31, 827-838.

[27] Little, S. A., K. D. Stolzenbach and F.J. Grassle, Tidal current effects on temperature in diffuse hydrothermal flow: Guaymas Basin, *Geophys. Res. Lett.*, 15 (13), 1491-1494, 1988.

[28] Rudnicki, M. D. and H. Elderfield, Theory applied to the Mid-Atlantic Ridge hydrothermal plumes: the finite difference approach, , *J. Volcanol. Geothermal. Res.* 50, 161-172, 1992.

[29] Lavelle, J. W. and M. A. Wetzler, Diffuse venting and background contributions to chemical anomalies in a neutrally buoyant ocean hydrothermal plume, *J. Geophys. Res.* 104 (C2), 3201-3209, 1999.

[30] Tivey, M. K., A. M. Bradley, T. M. Joyce and D. Kadko, Insights into tide-related variability at seafloor hydrothermal vents from time-series measurements, *Earth Planet Sci. Lett.* 202, 693-707, 2002.

[31] Schultz, A., J. R. Delaney and R. E. McDuff, On the partitioning of heat flux between diffuse and point source seafloor venting, *J. Geophys. Res.* 97, B9, 57-71, 1992.

[32] Schultz, A., P. Dickson and H. Elderfield, Temporal variations in diffuse hydrothermal flow at TAG, *Geophys. Res. Lett.* 23, (23), 3471-3474, 1996.

[33] Corliss, J. B., J. Dymond, L. I. Gordon, J. M. Edmond, R. P. von Herzen, R. D. Ballard, K. Green, D. Williams, A. Brainbridge, K. Crane and T. H. van Andel, Submarine thermal springs on the Galapagos Rift, *Science* 203, 1073-1083, 1979.

[34] Cooper, M. J., H. Elderfield and A. Schultz, Diffuse hydrothermal fluids from Lucky Strike hydrothermal vent field: Evidence for a shallow conductively heated system, *J. Geophys. Res.* 105, B5, 19369-19375, 2000.

[35] Schultz, A. and H. Elderfield, Controls on the physics and chemistry of seafloor hydrothermal circulation, *Phil. Trans. R. Soc. Lon.* 355 (1723), 387-425, 1997.

[36] Davis, E. and K. Becker, Tidal pumping of fluid within and form the oceanic crust: new observations and opportunities for sampling the crustal hydrosphere, *Earth Planet. Sci. Lett.* 172, 141-149, 1999.

[37] Fisher, A. T., Permeability within basaltic oceanic crust, *Rev. Geophys.* 36 (2), 143-182, 1998.

[38] Fisher, A. T. and K. Becker, Channelized fluid flow in oceanic crust reconciles heat-flow and permeability data, *Nature* 403, 71-74, 2000.

[39] Hammond, S. R., Relationships between lava types, seafloor morphology, and the occurance of hydrothermal venting in the ASHES vent field of Axial Volcano, *J. Geophys. Res.* 95 (B8), 12875-12893, 1990.

[40] Embley, R. W. and E. T. Baker, Interdisciplinary group explores seafloor eruption with remotely operated vehicle, *Eos Trans., American Geophysical Union* 80 (19), 213, 219, 222, 1999.

[41] Butterfield, D. A., G. J. Massoth, R. E. McDuff, J. E. Lupton and M. D. Lilley, Geochemistry of hydrothermal fluids from Axial Seamount Hydrothermal Emissions Study Vent Field, Juan de Fuca Ridge: Subseafloor boiling and subsequent fluid-rock interaction, *J. Geophys. Res.* 95 (B8), 12895-12921, 1990.

[42] Fox, C. G., Consequences of phase separation on the distribution of hydrothermal fluids at ASHES vent field, Axial Volcano, Juan de Fuca Ridge, *J. Geophys. Res.* 95 (B8), 12923-12926, 1990.

[43] Hildebrand, J. A., J. M. Stevenson, P. T. C. Hammer, M. A. Zumberge and R. L. Parker, A seafloor and sea surface gravity survey of Axial Volcano, *J. Geophys. Res.* 95, 12689-12696, 1990.

[44] Tivey, M. A. and H. P. Johnson, The magnetic structure of Axial Seamount, Juan de Fuca Ridge, *J. Geophys. Res.* 99, 12735-12750, 1992.

[45] West, M., W. Menke, M. Tolstoy, S. Webb and R. Sohn, Magma storage beneath Axial volcano on the Juan de Fuca mid-ocean ridge, *Nature* 418, 833-836, 2001.

[46] Dziak, R. P. and C. G. Fox, Long-term seismicity and ground deformation at Axial Volcano, Juan de Fuca Ridge, *Geophys. Res. Lett.* 26 (24), 3641-3644, 1999.

[47] Johnson, H. P., R. P. Dziak, C. R. Fisher, C. G. Fox and M. J. Pruis, Earthquakes' impact on hydrothermal systems may be far-reaching, *Eos, Trans.* 82 (21), 233,236, 2001.

[48] Johnson, H. P., M. Hutnak, R. P. Dziak, C. G. Fox, I. Urcuyo, J. P. Cowen, J. Nabelek and C. Fisher, Earthquake induced changes in a hydrothermal system on the Juan de Fuca mid-ocean ridge, *Nature*, 407, 174-177, 2000.

[49] Davis, E. E., K. Wang, R. E. Thomson, K. Becker and J. F. Cassidy, An episode of seafloor spreading and associated plate deformation inferred from crustal fluid pressure transients, *J. Geophys. Res.* 106 (B10), 21953-21963, 2001.

[50] Cowen, J. P., S. J. Giovannoni, F. Kenig, H. P. Johnson, D. Butterfield, M. S. Rappé, M. Hutnak and P. Lam, Microorganisms in fluids from 3.5 m.y. old ocean crust, *Science*, in press, 2003.

[51] Hutnak, M. and H. P. Johnson, On obtaining a hydrological seal with the sea floor: A concrete example from Axial Seamount, *Ridge Events* 10 (1), 24-28, 1999.

[52] Turcotte, D. L. and G. Schubert, Geodynamics: Applications of continuum physics to geological problems, John Wiley and Sons, New York, 450 pp., 1982.

[53] Davis, E. E., K. Wang, K. Becker and R. E. Thomson, Formation-scale hydraulic and mechanical properties of oceanic crust inferred from pore pressure response to periodic seafloor loading, *J. Geophys. Res.* 105 (B6), 13423-13435, 2000.

[54] Fox, C. G., In situ ground deformation measurements from the summit of Axial Volcano, *Geophys. Res. Lett.* 26 (23), 3437-3440, 1999.

[55] Wang, K. and E. E. Davis, Theory for the propagation of tidally induced pore pressure variations in layered subseafloor formations, *J. Geophys. Res.* 101, B5, 11483-11495, 1996.

[56] Trivett, D. A., Effluent from diffuse hydrothermal venting 1. A simple model of plumes from diffuse hydrothermal sources, *J. Geophys. Res.* 99, (C9), 18403-18415, 1994.

[57] Reynolds, O., On the experimental investigation of the circumstances which determine whether the motion of water shall be direct or sinuous, and the law of resistance in parallel channels, *Phil. Trans. Roy. Soc. A* 186, 123-164, 1883.

[58] Robigou, V., J. R. Delaney and D. S. Stakes, 1993. Large massive sulfide deposits in a newly discovered active hydrothermal system, the High-Rise Field, Endeavour Segment, Juan de Fuca Ridge, *Geophysical Research Letters* 20 (17), 1887–1890.

[59] Delaney, J. R., V. Robigou, R. E. McDuff and M. K. Tivey, 1992. Geology of a vigorous hydrothermal system on the Endeavour Segment, Juan de Fuca Ridge, *Journal of Geophysical Research* 97, 19663–19682.

[60] Butterfield, D. A., R. E. McDuff, M. J. Mottl, M. D. Lilley, J. E. Lupton and G. J. Massoth, 1994. Gradients in the composition of hydrothermal fluids from the Endeavour segment vent field: Phase separation and brine loss, *Journal of Geophysical Research* 99 (B5), 9561–9583.

[61] Little, S. A., K. D. Stolzenbach and R. P. Von Herzen, 1987. Measurements of plume flow from a hydrothermal vent field, *Journal of Geophysical Research* 92 (B3), 2587–2596.

[62] Ginster, U., M. J. Mottl and R. P. Von Herzen, 1994. Heat flux from black smokers on the Endeavour and Cleft segments, Juan de Fuca Ridge, *Journal of Geophysical Research* 99 (B3), 4937–4950.

[63] Turner, J. S., 1979. *Buoyancy effects in fluids*, B. K. Batchelor and J. W. Miles (Eds.), Cambridge University Press, Cambridge, 368 pp.

[64] Bemis, K. G., P. A. Rona, D. Jackson, C. Jones, D. Silver and K. Mitsuzawa, 2002. A comparison of black smoker hydrothermal plume behavior at Monolith

Vent and at Clam Acres Vent Field: Dependence on source configuration, *Marine Geophysical Researches* 23, 81–96.

[65] Speer, K. G. and P. A. Rona, 1989. A model of an Atlantic and Pacific hydrothermal plume, *Journal of Geophysical Research* 94 (C5), 6213–6220.

[66] Lavelle, J. W., E. T. Baker and G. J. Massoth, 1998. On the calculation of total heat, salt and tracer fluxes from ocean hydrothermal events, *Deep-Sea Research II* 45, 2619–2636.

[67] Rona, P. A. K. G. Bemis, D. Silver and C. D. Jones, 2002. Acoustic imaging, visualization, and quantification of buoyant hydrothermal plumes in the ocean, *Marine Geophysical Researches* 23, 147–168.

[68] Rosenberg, N. D., J. E. Lupton, D. Kadko, R. Collier, M. D. Lilley and H. Pak, 1988. Estimation of heat and chemical fluxes from a seafloor hydrothermal vent field using radon measurements, *Nature* 334, 604–607.

[69] Veirs, S. R., R. E. McDuff, M. D. Lilley and J. R. Delaney, 1999. Locating hydrothermal vents by detecting buoyant, advected plumes, *Journal of Geophysical Research* 104 (B12), 29239–29247.

[70] Thomson, R. E., S. F. Mihály, A. B. Rabinovich, R. E. McDuff, S. R. Veirs, and F. R. Stahr, 2003. Constrained circulation at Endeavour ridge facilitates colonization by vent larvae, *Nature* 424, 545–549.

[71] Lupton, J., 1998. Hydrothermal helium plumes in the Pacific Ocean, *Journal of Geophysical Research* 103 (C8), 15853–15868.

[72] Bemis, K. G., R. P. Von Herzen and M. J. Mottl, 1993. Geothermal heat flux

from hydrothermal plumes on the Juan de Fuca Ridge, *Journal of Geophysical Research* 98, 6351–6365.

[73] Epstein, M. and J. P. Burlach, 2001. Vertical mixing above a steady circular source of buoyancy, *International Journal of Heat and Mass Transfer* 44, 526–536.

[74] Jackson, D. R., C. D. Jones, P. A. Rona and K. G. Bemis, 2003. A method for Doppler acoustic measurement of black smoker flow fields, *Geochemistry, Geophysics, Geosystems* 4 (11), 1095, doi:10.1029/2003GC000509.

[75] Fanneløp, T. K. and D. M. Webber, 2003. On buoyant plumes rising from area sources in a calm environment, *Journal of Fluid Mechanics* 497, 319–334.

[76] McDuff, R. E., 1994. Physical dynamics of deep-sea hydrothermal plumes, In: *Seafloor hydrothermal systems: Physical, chemical, biological, and geological interactions*, Geophysical Monograph Series 91, 317–346.

[77] Von Damm, K. L., 1995. Controls on the chemistry and temporal variability of seafloor hydrothermal fluids, In: *Seafloor Hydrothermal Systems: Physical, Chemical, Biological, and Geological Interactions*, Geophysical Monograph Series 91, American Geophysical Union, pp. 222–246.

[78] Trivett, D. A. and A. J. Williams III, 1994. Effluent from diffuse hydrothermal venting 2. Measurement of plumes from diffuse hydrothermal vents at the southern Juan de Fuca Ridge, *Journal of Geophysical Research* 99 (C9), 18417–18432.

[79] James, R. H. and H. Elderfield, 1996. Chemistry of ore forming fluids and mineral formation rates in an active hydrothermal sulfide deposit on the Mid-Atlantic Ridge, *Geology* 24, 1147–1150.

[80] Murton, B. J., L. J. Redbourn, C. R. German and E. T. Baker, 1999. Sources and fluxes of hydrothermal heat, chemicals and biology within a segment of the Mid-Atlantic Ridge, *Earth and Planetary Science Letters* 171, 301–317.

[81] Tivey, M. K., S. E. Humphris, G. Thompson, M. D. Hannington and P. A. Rona, 1995. Deducing patterns of fluid flow and mixing within the TAG active hydrothermal mound using mineralogical and geochemical data, *Journal of Geophysical Research* 100, 12527–12555.

[82] Sedwick, P. N., G. M. McMurtry and J. D. Macdougall, 1992. Chemistry of hydrothermal solutions from Pele's Vents, Loihi Seamount, Hawaii, *Geochimica et Cosmochimica Acta* 56, 3643–3667.

[83] Johnson, K. S., J. J. Childress, R. R. Hessler, C. M. Sakamoto-Arnold and C. L. Beehler, 1988. Chemical and biological interactions in the Rose Garden hydrothermal vent field, Galápagos spreading center, *Deep-sea Research,* 35, 1723–1744.

[84] Huber, J., D. A. Butterfield and J. Baross, 2002. Temporal changes in archaeal diversity and chemistry in a mid-ocean ridge subseafloor habitat, *Applied Environmental Microbiology* 68, 1585–1594.

[85] Bear, 1972. *Dynamics of Fluids in Porous Media*, Elsevier, New York, 764 pp.

[86] Gilbert, L. A. and H. P. Johnson, 1999. Direct measurements of oceanic crustal density at the northern Juan de Fuca Ridge, *Geophysical Research Letters* 26 (24), 3633–3636.

[87] Rohsenow, W. M., J. P. Hartnett and Y. I. Cho, 1998. *Handbook of heat transfer,* New York, McGraw-Hill, 1483 pp.

[88] Lowell, R. P. and Y. Yao, 2002. Anhydrite precipitation and the extent of hydrothermal recharge zones at ocean ridge crests, *Journal of Geophysical Research* 107 (B9), 2183, 10.1029/2001JB001289.

[89] Slawson, P. R. and G. T. Csanady, 1967. On the mean path of buoyant, bent-over chimney plumes, *Journal of Fluid Mechanics* 28, 311–322.

[90] Maxworthy, T. and S. Narimousa, 1994. Unsteady, turbulent convection into a homogeneous, rotating fluid, with oceanographic applications, *Journal of Physical Oceanography* 24 (5), 865–887.

[91] Lavelle, J. W., 1997. Buoyancy-driven plumes in rotating, stratified cross flows: plume dependence on rotation, turbulent mixing, and cross-flow strength, *Journal of Geophysical Research* 102 (C2), 3405–3420.

[92] Hanna, S. R., G. A. Briggs and R. P. Hosker Jr., 1982. *Handbook of Atmospheric Diffusion*, Tech. Inf. Cent., U. S. Dept. of Energy, Washington D.C., 102 pp.

[93] Middleton, J. H., 1986. The rise of forced plumes in a stably stratified crossflow, *Boundary-Layer Meteorology* 36, 187–199.

[94] Jones, H. and J. Marshall, 1993. Convection with rotation in a neutral ocean: A study of open-ocean deep convection, *Journal of Physical Oceanography,* 23, 1009–1039.

[95] Ivey, G., J. Taylor and M. Coates, 1995. Convectively driven mixed layer growth in a rotating, stratified fluid, *Deep-Sea Research* 95, 331–349.

[96] Visbeck, M., J. Marshall and H. Jones, 1996. Dynamics of isolated convective regions in the ocean, *Journal of Physical Oceanography* 26, 1721–1734.

[97] Thwaites, F. T. and A. J. Williams III, 1997. New current meter development, *Sea Technology* 4, 108–112.

[98] Veirs, S. R., 2003. Heat flux and hydrography at a submarine volcano: Observations and models of the Main Endeavour vent field in the Northeast Pacific, PhD thesis, University of Washington.

[99] Williams, A. J. III, J. S. Tochko, R. L. Koehler, W. D. Grant, T. F. Gross and C. V. R. Dunn, 1987. Measurement of turbulence in the oceanic bottom boundary layer with an acoustic current meter array, *Journal of Atmospheric and Oceanic Technology* 4, 312–327.

[100] Shaw, W. J. and J. H. Trowbridge, 2001. The direct estimation of near-bottom turbulent fluxes in the presence of energetic wave motions, *Journal of Atmospheric and Oceanic Technology* 18, 1540–1557.

[101] Williams, A. J. III, 2001. Acoustic current meter zero offset drift, *Oceans 2001*, 916–921.

[102] Prandtl, L., 1925. Bericht über Untersuchungen zur ausgebildeten Turbulenz, *Zeitschrift für angewandte Mathematik und Mechanik* 5 (2), 136–139.

[103] Businger, J. A., J. C. Wyngaard, Y. Izumi and E. F. Bradley, 1971. Flux-profile relationships in the atmospheric surface layer, *Journal of the Atmospheric Sciences* 28, 181–189.

[104] Dyer, A. J., 1974. A review of flux-profile relationships, *Boundary-Layer Meteorology* 7, 363–372.

[105] McPhee, M. G. and D. G. Martinson, 1994. Turbulent mixing under drifting pack ice in the Weddell Sea, *Science* 263, 218–221.

[106] Hinze, J. O., 1975. *Turbulence*, McGraw-Hill, New York, 790 pp.

[107] Gross, T. F. and A. R. M. Nowell, 1985. Spectral scaling in a tidal boundary layer, *Journal of Physical Oceanography* 15 (5), 496–508.

[108] Marsh, A. G., L. S. Mullineaux, C. M. Young and D. T. Manahan, 2001. Larval dispersal potential of the tubeworm *Riftia pachyptila* at deep-sea hydrothermal vents, *Nature* 411, 77–80.

[109] van Dover, C. L., C. R. German, K. G. Speer, I. M. Parson and R. C. Vrijenhoek, 2002. Evolution and biogeography of deep-sea vent and seep invertebrates, *Science* 295, 1253–1257.

[110] Thurnherr, A. M., K. J. Richards, C. R. German, G. F. Lane-Serff and K. G. Speer, 2002. Flow and mixing in the rift valley of the Mid-Atlantic Ridge, *Journal of Physical Oceanography* 32, 1763–1778.

[111] Mottl, M. J., 2003. Partitioning of energy and mass fluxes between mid-ocean ridge axes and flanks at high and low temperature, In: P. E. Halback, V. Tunnicliffe and J. R. Hein (Eds.), *Energy and Mass Transfer in Marine Hydrothermal Systems*, Dahlem University Press, Berlin, pp. 271–286.

[112] Wheat, C. G., J. McManus, M. J. Mottl and E. Giambalvo, 2003. Oceanic phosphorus imbalance: Magnitude of the mid-ocean ridge flank hydrothermal sink, *Geophysical Research Letters* 30 (17), 1895, doi:10.1029/2003GL017218.

[113] Johnson, H. P., and 17 others, 2002. Survey studies hydrothermal circulation on the Northern Juan de Fuca Ridge, *Eos, Transactions,* American Geophysical Union, 83 (8), 73, 78–79.

[114] Crawford, W. C., S. C. Webb and J. A. Hildebrand, Seafloor compliance observed by long-period pressure and displacement measurements, *J. Geophys. Res., 96,* B10, 16151–16160, 1991.

[115] Glasby, G. P. and J. Kasahara, Influence of tidal effects on the periodicity of earthquake activity in diverse geological settings with particular emphasis on submarine hydrothermal systems, *Earth-Science Rev., 52,* 291–297, 2001.

[116] Wilcock, W. S. D., Tidal triggering of microearthquakes on the Juan de Fuca Ridge, *Geophys. Res. Lett., 28,* 20, 3999–4002, 2001.

[117] Tolstoy, M. F. L. Vernon, J. A. Orcutt, F. K. Wyatt, Breathing of the seafloor: Tidal correlations of seismicity at Axial volcano, *Geology, 30,* 6, 503–506, 2002.

[118] Johnson, H. P. and V. Tunnicliffe, Time-series measurements of hydrothermal activity on the northern Juan de Fuca Ridge, *Geophys. Res. Lett., 12,* 10, 685–688, 1985.

[119] Kinoshita, M., R. P. Von Herzen, O. Matsubayashi and K. Fujioka, Tidally-driven effluent detected by long-term temperature monitoring at the TAG hydrothermal mound, Mid-Atlantic Ridge, *Phys. Earth Planet. Int., 109,* 201–212, 1998.

[120] Ingebritsen, S. E. and D. O. Hayba, Fluid flow and heat transport near the critical point of H_2O, *Geophys. Res. Lett., 20,* 2199–2202, 1994.

[121] Norton, D. L. and J. Knight, Transport phenomena in hydrothermal systems: cooling plutons, *Am. J. Sci., 277,* 937–981, 1977.

[122] Lister, C. R. B., Heat transfer between magmas and hydrothermal systems, or, six lemmas in search of a theorem, *Geophys. J. Int., 120,* 45–59, 1995.

[123] Jupp, T. and A. Schultz, A thermodynamic explanation for black smoker temperatures, *Nature, 403,* 880–883, 2000.

[124] Wolery, T. J., and N. H. Sleep, Hydrothermal circulation and geochemical flux at mid-ocean ridges, *J. Geology, 84,* 249–275, 1976.

[125] Lowell, R. P., P. A. Rona and R. P. Von Herzen, Seafloor hydrothermal systems, *J. Geophys. Res., 100,* B1, 327–352, 1995.

[126] Wagner, W. and A. Kruse, *Properties of Water and Steam*, Springer Verlag, 372 pp., 1998.

[127] Kelley, D. S. and J. R. Delaney, Two-phase separation and fracturing in mid-ocean ridge gabbros at temperatures greater than 700 °C, *Earth Planet. Sci. Lett., 83,* 53–66, 1987.

[128] Fournier, R. O., Hydrothermal processes related to movement of fluid from elastic into brittle rock in the magmatic-epithermal environment, *Econ. Geol., 94,* 1193–1212, 1999.

[129] Norton, D. L., Transport phenomena Theory of hydrothermal systems, *Ann. Rev. Earth Planet Sci., 12,* 155–177, 1984.

[130] Alt, J. C., *Subseafloor processes in mid-ocean ridge hydrothermal systems, Seafloor Hydrothermal Systems: Physical, Chemical, Biological, and Geological Interactions*, AGU Geophys. Mono., 91, 85–114, 1995.

[131] Goldfarb, M. S., and J. R. Delaney, Response of two-phase fluids to fracture configurations within submarine hydrothermal systems, *J. Geophys. Res., 93,* B5, 4585–4594, 1988.

[132] Corey, A. T., The interrelation between gas and oil relative permeabilities, *Prod. Mon., 19,* 38–41, 1954.

[133] Grant, M. A., I. G. Donaldson and P. F. Bixley, *Geothermal Reservoir Engineering*, Academic, San Diego, CA, 369 pp., 1982.

[134] Pruess, K. and Y. W. Tsang, On two-phase relative permeability and capillary pressure of rough-walled rock fractures, *Water Resour. Res., 26,* 9, 1915–1926, 1990.

[135] Quintard, M., M. Kaviany and S. Whitaker, Two medium treatment of heat transfer in porous media: Numerical results for effective properties, *Adv. Water. Resour., 20,* 77–94, 1997.

[136] Wakao, N. and S. Kaguei, *Heat and Mass Transfer in Packed Beds*, Gordon and Breach Science, New York, 1982.

[137] Schumann, T. E. W., Heat transfer: A liquid flowing through a porous prism, *J. Franklin Institute., 208,* 405 pp., 1928.

[138] Crone, T. J. and W. S. Wilcock, Modeling the effects of tidal loading on hydrothermal discharge at mid-ocean ridges, *Eos Trans. AGU,* 83 (47), 2002.

[139] Jupp, T. E. and A. Schultz, A poroelastic model for the tidal modulation of seafloor hydrothermal systems, *J. Geophys. Res.*, submitted, 2003.

[140] Shock, E. L., Chemical environments of submarine hydrothermal systems, *Origins Life Evol. Biosphere, 22,* 67–107, 1992.

[141] Nehlig, P. and T. Juteau, Flow porosities, permeabilities and preliminary data on fluid inclusions and fossil thermal gradients in the crustal sequence of the Sumail ophiolite (Oman), *Tectonophysics, 151,* 199–221, 1988.

[142] van Everdingen, D. A., Fracture characteristics of the sheeted dike complex, Troodos ophiolite, Cyprus: Implications for permeability of oceanic crust, *J. Geophys. Res., 100,* 19957–19972, 1995.

[143] Lowell, R. P. and L. N. Germanovich, Dike injection and the formation of megaplumes at ocean ridges, *Science, 267,* 1804–1807, 1995.

[144] Wilcock, W. S. D. and A. McNabb, Estimates of crustal permeability on the Endeavour segment of the Juan de Fuca mid-ocean ridge, *Earth Planet. Sci. Lett., 138,* 83–91, 1996.

[145] Cherkaoui, A. S. M., W. S. D. Wilcock and E. T. Baker, Thermal fluxes associated with the 1993 diking event on the CoAxial segment, Juan de Fuca Ridge: A model for the convective cooling of a dike, *J. Geophys. Res., 102,* 24887–24902, 1997.

[146] Becker, K. and E. E. Davis, New evidence for age variation and scale effects of permeabilities of young oceanic crust from borehole thermal and pressure measurements, *Earth Planet. Sci. Lett., 210,* 499–508, 2003.

[147] Pitzer, K. S., J. C. Peiper and R. H. Busey, Thermodynamic properties of aqueous sodium chloride solutions, *J. Phys. Chem. Ref. Data, 13,* 1, 1–102, 1984.

[148] Anderko, A. and K. S. Pitzer, Equation-of-state representation of phase equilibria and volumetric properties of the system NaCl-H_2O above 573 K, *Geochim. Cosochim. Acta, 57,* 1657–1680, 1993.

[149] Bischoff, J. L., and R. J. Rosenbauer, An empirical equation of state for hydrothermal seawater (3.2 Percent NaCl), *Amer. J. Sci., 285,* 725–763, 1985.

[150] Monfort, M. and A. Schultz, Time series measurements of hydrothermal vent temperature and diffuse percolation velocity: results from an ALVIN submersible program, Endeavour Segment, Juan de Fuca Ridge, *Eos, Trans. AGU, 69,* 1484, 1988.

[151] McDuff, R. E. and J. R. Delaney, Periodic variability in fluid temperature at a seafloor hydrothermal vent, *Eos, Trans. AGU, 76,* F710, 1995.

[152] Fornari, D. J., T. Shank, K. L. Von Damm, T. K. P. Gregg, M. Lilley, G. Levai, A. Bray, R. M. Haymon, M. R. Perfit and R. Lutz, Time-series temperature measurements at high-temperature hydrothermal vents, East Pacific Rise 9° 49′-51′N: evidence for monitoring a crustal cracking event, *Earth Planet. Sci. Lett., 160,* 419–431, 1998.

[153] McLaughlin-West, E. A., E. J. Olson, M. D. Lilley, J. A. Resing, J. E. Lupton, E. T. Baker and J. P. Cowen, Variations in hydrothermal methane and hydrogen concentrations following the 1998 eruption at Axial Volcano, *Geophys. Res. Lett., 26,* 23, 3453–3456, 1999.

[154] Resing, J. A., R. Feely, G. Massoth and E. T. Baker, The water-column chemical signature after the 1998 eruption of Axial Volcano, *Geophys. Res. Lett., 26,* 3645–3648, 1999.

[155] Mofjeld, H. O., F. I. González and M. C. Eble, Subtidal bottom pressure observed at Axial Seamount in the northeastern continental margin of the Pacific Ocean, *J. Geophys. Res., 101,* C7, 16381–16390, 1996.

[156] Fisher, A. T., E. E. Davis, M. Hutnak, V. Spiess, L. Zuhlsdorff, A. Cherkaoui, L. Christiansen, K. Edwards, R. Macdonald, H. Villinger, M. J. Mottl, C. G.

Wheat and K. Becker, Hydrothermal recharge and discharge across 50 km guided by seamounts on a young ridge flank, *Nature* 421, 618–621, 2003.

[157] Spinelli, G. A. and A. T. Fisher, Hydrothermal circulation within topographically rough basaltic basement on the Juan de Fuca Ridge flank, *Geochemistry, Geophysics, Geosystems* 5 (2), 10.1029/2003GC000616, 2004.

[158] Johnson, H. P. and the LExEn scientific party, Probing for life in the ocean crust with the LExEn program, *EOS,* Trans. AGU, 84 (12), 109–116, 2003.

Appendix A

WHERE TO FIND THE FILES

Copies of the publications related to this dissertation are available for download from http://www.nwra.com/resumes/pruis/publications/.

Data files and processing code are available upon request, please send email to matt@nwra.com.

VITA

Matt Pruis obtained his Bachelor of Science in applied geophysics from Michigan Technological University in 1995, and his Master of Science in oceanography from the University of Washington in 1998. He has authored or co-authored eight papers that have been published in peer-reviewed journals, and many additional abstracts presented at international conferences. He has participated in 7 land/near-shore research programs; 6 deep-water research cruises; 2 research cruises using a deep-diving submersible; 4 research cruises using a ROV; 2 research cruises using an AUV; 2 coring cruises and been observer on 3 submersible dives. Matt authored an online science journal for Europa Focus Group field conference held in Barrow, AK, which was published by the *Astrobiology Magazine* and picked up by *Space.com* and NASA Ames. He also developed an on-line magnetics tutorial used by the *Discovery Channel School Understanding: Physics in Motion* program and was coordinator of the *MaGIC* web site that allowed grade school classes to interact with scientists aboard the R/V Thomas G. Thompson. In addition to these outreach and educational activities, Matt has been a teaching assistant in courses on Environmental Geology and Physical Oceanography. Matt is currently working as a support scientist at North-West Research Associates.